

Design, Fabrication, and Characterization of Semiconductor Transverse Bragg Resonance Lasers

Thesis by
John M. Choi

In Partial Fulfillment of the Requirements
for the Degree of
Doctor of Philosophy



California Institute of Technology
Pasadena, California

2007

(Defended February 5, 2007)

© 2007

John M. Choi

All Rights Reserved

Scripture taken from the Holy Bible, NEW INTERNATIONAL VERSION®. Copyright © 1973, 1978, 1984 International Bible Society. All rights reserved throughout the world. Used by permission of International Bible Society.

NEW INTERNATIONAL VERSION® and NIV® are registered trademarks of International Bible Society. Use of either trademark for the offering of goods or services requires the prior written consent of International Bible Society.

Acknowledgements

Let them give thanks to the LORD for his unfailing love
and his wonderful deeds for men,
for he breaks down gates of bronze
and cuts through bars of iron.

Psalm 107:15-16

Foremost, I thank my God, without whom I can do nothing. His love endures forever.

I would like to thank my advisor, Prof. Amnon Yariv, for providing the environment and resources in which to grow. Also, I thank Prof. Bruno Crosignani, who has been like a second advisor, for his counsel and support. Together, they have been fathers to our group, tending to our minds and souls. I am grateful to be able to trace my scientific parentage to them.

Additionally, I would like to thank everyone in our group, all of whom have been instrumental in guiding me along my path. Of particular note are Dr. Reg Lee, who trained me in the experimental, and Prof. Yong Xu, the theoretical. I am forever in their debt for the time they took to patiently teach me how to think. I would like to thank all the students that I have worked with over the years: Dr. Will Green, Dr. Roger Koumans, Wei Liang, Prof. Shayan Mookherjea, Dr. George Paloczi, Joyce Poon, Dr. Dan Provenzano, Naresh Satyan, Xiankai Sun, and Lin Zhu. Also, I would like to express my appreciation to the post-docs and visiting scholars for their discussions and support: Dr. Philip Chak, T. R. Chen, Prof. Avishay Eyal, Prof. Yanyi Huang, Dr. Robert Lang, Dr. Bill Marshall, and Prof. Koby Scheuer. Finally, I would like to acknowledge the staff who tend to the daily operations of our group: Kevin Cooper, Ali Ghaffari, Irene Loera, and Connie Rodriguez. A special thanks to those who have shared an office with me, who had to endure more than the daily recommended allowance of me.

In addition, this thesis work could not have been done without the support of many outside Caltech. At the Stanford Nanofabrication Facility, I would like to thank all the staff for their training and support, especially James Conway, Paul Jerabek, Mahnaz Mansourpour, Ed Myers, Jeannie Perez, Mary Tang, and Uli Thumser. Also at Stanford, I would like to thank my fellow labmates, Rafael Aldaz, Dr. Jim Kruger, Dr. Eric Perozziello, and Mike Wiemer. At nLight Corporation, I am especially grateful to Dr. Paul Crump for his support of our collaboration.

I would also like to acknowledge the agencies that have provided support for this work: the Department of Defense (National Defense Science and Engineering Graduate Fellowship), DARPA (SHEDS), and the industrial sponsors of Stanford CIS (CIS New User Grant).

Finally, I would like to express my deepest and most sincere gratitude to my family, my parents and brother, and my surrogate family while at Caltech, Pastors Ché and Sue Ahn, Todd and Junia Pokrifka-Joe, and Jessica Kang, for their love, patience, encouragement, and unconditional support.

Abstract

Controlling the spatial modes of a laser cavity is fundamental for improving the beam quality of a laser and achieving highly efficient coupling of power into an optical system. High-power applications are particularly challenging due to the conflicting requirements for large modal volume, to prevent facet damage by reducing energy density, and narrow width, for single-mode operation of an index-guided waveguide. By replacing traditional index confinement with Bragg reflection in the transverse direction, single-mode operation can be achieved even for large modal volumes. These grating confined structures, transverse Bragg resonance (TBR) waveguides, have the unique ability to support localized modes above the light line. Such modes normally couple to radiation modes of the cladding when the confinement mechanism is total-internal-reflection and are too lossy to be considered guided modes. However, for Bragg resonance confined modes, the modal loss can be designed by careful optical mode engineering to introduce a large loss discrimination that can favor a single spatial, low-loss mode. Semiconductor TBR lasers in an InP/InGaAsP/InGaAs material system were designed, fabricated, and characterized to investigate this property. Two regions of operation are identified for TBR waveguides, and, while transverse mode selection is provided by a grating, longitudinal mode control is found to be also necessary to restrict operation to the region that supports modes above the light line.

Contents

1	Introduction	1
2	Numerical Analysis Techniques	3
2.1	Scalar Approach	3
2.1.1	Approximating Maxwell's Equations	3
2.1.2	Finite Difference Eigenvalue Problem	4
2.1.3	Matrix Method	5
2.2	Vector Approach	13
2.2.1	Discretizing Maxwell's Equations	13
2.2.2	Boundary Conditions	15
2.2.3	Time Domain Filtering	17
2.2.4	Parallel Implementation	23
3	Waveguide Models	27
3.1	Index Guided Waveguides	27
3.1.1	Slab Waveguide Solutions	27
3.1.2	Single Mode	30
3.2	Transverse Bragg Reflection	32
3.2.1	Coupled Mode Analysis of Bragg Layers	33
3.2.2	Transverse Bragg Resonance Waveguides	39
3.2.3	Simulation Results	43

4	Device Design, Fabrication, and Measurement	50
4.1	Design	50
4.1.1	Grating Pitch	50
4.1.2	Wafer Epitaxy/Surface Grating	52
4.2	Fabrication	55
4.3	Measurement	69
4.3.1	Experimental Setup	69
4.3.2	Pulsed and Continuous Lasing	70
4.3.3	Nearfield	71
4.3.4	Farfield	71
5	Analysis of Results	81
5.1	Coupled Waveguides	81
5.2	Transverse Bragg Resonance Waveguides, Revisited	90
5.3	Device Simulations	105
6	Conclusion	112

List of Figures

2.1	Slab waveguide solutions	4
2.2	Schematic of layered media showing forward and backward travelling wave amplitudes	8
2.3	Reflection and transmission spectrum of a Bragg stack	9
2.4	Field intensity distribution of the forward and backward waves travelling in Bragg stack of Fig. 2.3	10
2.5	Reflection and transmission spectrum of the Bragg stack in Fig. 2.3 with gain	11
2.6	Field intensity distribution of the forward and backward waves travelling in Bragg stack of Fig. 2.5	12
2.7	A cell of the FDTD grid	15
2.8	Filter function, $\text{sinc}(\omega)$	19
2.9	Two common memory models for parallel computing	24
2.10	Split domain of a two dimensional topology. Ghost cells are shown shaded in gray.	26
3.1	A slab waveguide	28
3.2	Graphical solution to the slab waveguide	30
3.3	Effective index difference between the two lowest order (largest effective index) modes of a slab waveguide	32

3.4	The TBR waveguide geometry consisting of a GaAs substrate and air holes. x and z are the transverse and longitudinal dimensions, respectively. The core width is W . The hole radius is $r = 0.15a$. A_0 and A_1 represent the inward propagating plane-wave components in the core and cladding respectively. A_2 represents the incoming field outside the cladding. B_0 , B_1 , and B_2 represent similar quantities for the outward propagating components.	33
3.5	The 2D FDTD simulation domain showing a sample field calculation	44
3.6	Normalized transverse field decay calculated by the 2D FDTD simulation for a structure with approximately 10 layers of Bragg periods	45
3.7	Dispersion curves for varying widths of the core	46
3.8	Plot of normalized loss constant, αa , from 2D FDTD simulations for varying core widths with the propagation constant, β_R , as a parameter	47
3.9	Plot of normalized loss constant from 2D FDTD simulations as well as coupled mode (CM) theory for selected core width values	48
3.10	The reciprocal lattice vectors for the triangular lattice, $a_1 = -4\pi/b \hat{x}$ and $a_2 = -2\pi/b \hat{x} - 2\pi/a \hat{z}$	49
4.1	Schematic showing equivalent ray optics path within TBR waveguide	51
4.2	Photoluminescence of unprocessed wafer of Table 4.1 excited by a Ti:sapphire pulsed source	54
4.3	Electron microscope images of developed PMMA that is (a) underexposed, (b) optimally exposed, and (c) overexposed . .	56

4.4	500nm squares etched into InP using a HBr:HNO ₃ mixture . .	57
4.5	Electron microscope image of etched profile using a HBr:HNO ₃ mixture showing the etch rates for different InGaAsP alloys . .	58
4.6	Surface gratings after HCl:H ₂ O etch into InP mixture	59
4.7	Process flow	60
4.8	Electron microscope images of surface after etching of pla- narization polymer showing (a)incomplete planarization and (b) complete planarization	64
4.9	Scanning electron microscope images of lift-off resist profiles for (a) photolithography and (b) electron beam lithography . .	65
4.10	Scanning electron microscope image of developed LOR10B and photoresist showing undercut profile	66
4.11	Scanning electron microscope images of TBR lasers showing the defect region. (a) A high index defect composed of semi- conductor and (b) a low index defect composed of polymer . .	67
4.12	A fully fabricated device die-bonded onto a c-mount heatsink and wirebonded	68
4.13	Experimental setup used for measurement of devices	69
4.14	Schematic diagram of apparatus for (a) thermoelectric cooling and (b) cyrogenic cooling	72
4.15	Average optical power vs. peak voltage of a TBR laser as a function of duty cycle for a 10 μ s period. Data is shown for 100ns to 2 μ s pulse widths at a heat sink temperature of 10°C.	73
4.16	Lasing spectrum shift as a function of cryostat temperature . .	74
4.17	(a) Continuous wave light vs. current density curves at cryo- stat temperature of 82K. (b) Current vs. voltage curves of corresponding lasers	75

4.18	(a) Lasing spectra of a broad-area laser, a low index defect TBR, and a high index defect TBR. The dashed curves show the lasing spectra at threshold. (b) Lasing threshold of the high index defect TBR laser at various operating points	76
4.19	Nearfield image below threshold for (a) broad-area, (b) high index defect TBR, and (c) low index defect TBR	77
4.20	Nearfield image at threshold for (a) broad-area, (b) high index defect TBR, and (c) low index defect TBR	78
4.21	Nearfield image above threshold for (a) broad-area, (b) high index defect TBR, and (c) low index defect TBR	79
4.22	Farfield image above threshold for (a) broad-area, (b) high index defect TBR, and (c) low index defect TBR	80
5.1	Dispersion curves calculated for various coupled waveguide systems composed of 2, 3, and 10 identical waveguides. The light lines for the high index and low index materials as well as the analytic slab waveguide theory are shown.	86
5.2	Two coupled waveguides and the mode solutions, showing the even and odd mode splitting. The separation between the two waveguides is given by d	87
5.3	The propagation constant difference between the odd/even mode splitting as a function of the separation distance, d in Fig. 5.2. As d increases, κ decreases, reducing the separation as described by Eq. 5.28.	88
5.4	Ten coupled waveguides and the first 3 mode solutions	89
5.5	A coupled array waveguide consisting of 5 periods of Bragg reflectors that will be one half of a TBR waveguide. The lowest order mode electric field profile is shown.	90

5.6	A coupled array waveguide composed of the two waveguides shown in Fig. 5.5. The even/odd splitting of the lowest order mode is shown as well as a slab mode confined to the central high index (defect) region.	91
5.7	The Bragg confined defect mode as well as the two band edge modes of a TBR waveguide	93
5.8	Mode profile of the lowest order mode for a (a) high index defect region, and a (b) low index defect region	94
5.9	Dispersion of the TBR defect mode for the model shown in Fig. 5.7. The crossover points show that for small propagation constants, β , the modes are above the light line, and for very large propagation constants, the modes sink below the light line.	95
5.10	The modes of the TBR structure shown for a single frequency. The theoretical curves for TIR and TBR modes are also shown.	97
5.11	Modal loss of the modes shown in Fig. 5.10, $\omega\Lambda/2\pi c = 0.385$. The TBR defect mode is circled.	98
5.12	Modal loss at $\omega\Lambda/2\pi c = 0.598$. The TBR defect mode is circled.	99
5.13	The modal loss/gain of the defect mode, effective index 2.39, and the 2 nearest band edge modes on either side as the material gain of the laser is increased	101
5.14	Mode profiles of the defect mode and a band edge mode showing the radiation into the substrate outside the grating region for a passive, lossless waveguide structure	102
5.15	Modal loss dependence of the defect mode and two neighboring band edge modes of the structure shown in Fig. 5.14 as the material loss outside the grating region is increased	103

5.16	Mode profiles of the defect mode and a band edge mode showing the absorption of the substrate radiation leakage shown in Fig. 5.14 when the material loss outside the grating region is increased sufficiently	104
5.17	Mode profile of the defect mode and band edge mode for a lossless grating region. Note that there are twice as many Bragg layers as in the structure for Fig. 5.15, reducing the radiation loss of the defect mode. The radiation of the band edge mode is not effected.	105
5.18	Mode profile of the defect mode and band edge mode shown in Fig. 5.17 in the presence of material gain in the grating region displaying the same qualitative behavior	106
5.19	(a) The surface grating semiconductor structures. The box shows the unit cell used for calculating the band structure. (b) The index contours of the actual simulation domain	107
5.20	Band diagram of the surface grating structure. The inset shows the Brillouin zone edge.	108
5.21	Intensity distribution of fields at the Brillouin zone edge . . .	110
5.22	Dispersion of the propagating band edge modes for the actual fabricated device	111

List of Tables

4.1	Epitaxial wafer structure	53
4.2	Electron beam resist coat procedures	57
4.3	PMMA develop procedure	58
4.4	Etch procedure	59
4.5	BCB planarization coat procedure	61
4.6	Photolithography procedure	62

Chapter 1

Introduction

The control and design of optical cavity modes has been a fundamental element of designing lasers. The field of semiconductor lasers has advanced from the use of buried heterostructure devices for transverse confinement[28] to the latest in mode control, the photonic bandgap, defect mode laser[21]. This latter example is an illustration of the importance of periodic structures in controlling the optical modes of a laser. While the use of periodic structures has become in vogue due to the field of multi-dimensional photonic crystals, of which the defect laser is an example, the fundamental concept of using periodicity to control the guided modes of light is a well-known idea[37]. One of the earliest practical implementations that is still of great significance today is the semiconductor distributed-feedback (DFB) laser[19], in which the periodic corrugation provides longitudinal feedback resulting in frequency selection.

The transverse Bragg resonance (TBR) laser[34] also includes a periodic corrugation, but in the transverse direction. This Bragg grating provides transverse confinement only for modes that have transverse wave vectors that satisfy the Bragg condition. Thus, in the same way that the grating in a DFB fixes the longitudinal wave vector, in a TBR the transverse component is fixed. This limitation of the transverse wave vector should allow the TBR

laser to lase in a single transverse mode regardless of the lateral size of the device, in contrast to traditional ridge waveguide lasers[15]. The resulting single transverse mode can be very large, spread out over the entire width of the device. This is an important feature for high-power laser applications where high-power densities can cause catastrophic optical damage (COD) at the end facets[26]. Thus, the TBR laser has 2 attractive features for high-power applications: good beam quality, as defined by a single lateral mode, and a large aperture for high-power extraction while reducing the power density.

While there have been many proposed methods for controlling the spatial modes of a high-power, large modal volume laser, such as phased arrays[4], Bragg reflection[9, 22], and mode filtering[29], the standard workhorse for high-power lasers is still the single stripe, broad area laser, packaged as a single emitter or as a multiple emitter stacked bar. It is hoped that the analysis of the TBR laser in the following chapters will provide insight into the control of modes using a transverse Bragg grating and bring us closer to the reality of a useful, single-mode, high-power laser.

Chapter 2

Numerical Analysis Techniques

2.1 Scalar Approach

2.1.1 Approximating Maxwell's Equations

We start with the standard approach to solving the scalar wave equation in two dimensional systems[17]. Maxwell's equations simplified within a dielectric medium (no charge) are

$$\nabla \times \mathbf{E} = -\partial_t(\mu\mathbf{H}) \quad \nabla \times \mathbf{H} = \partial_t(\epsilon\mathbf{E}) \quad (2.1)$$

$$\nabla \cdot \mathbf{E} = 0 \quad \nabla \cdot \mathbf{H} = 0 \quad (2.2)$$

(This assumes that $\nabla \cdot \epsilon \sim 0$.) Using the vector identity $\nabla \times \nabla \mathbf{A} = \nabla(\nabla \cdot \mathbf{A}) - \nabla^2 \mathbf{A}$, we can get $\nabla^2 \mathbf{E} - n^2/c^2 \partial_t^2 \mathbf{E} = 0$. Assuming travelling, time harmonic solutions,

$$E(x, z, t) = E(x) \exp(i\omega t - i\beta z) \quad (2.3)$$

gives the form $(\partial_x^2 + \partial_y^2)E = (\beta^2 - n^2 k_0^2)E$ which reduces to

$$\partial_x^2 E = (\beta^2 - n^2 k_0^2)E \quad (2.4)$$

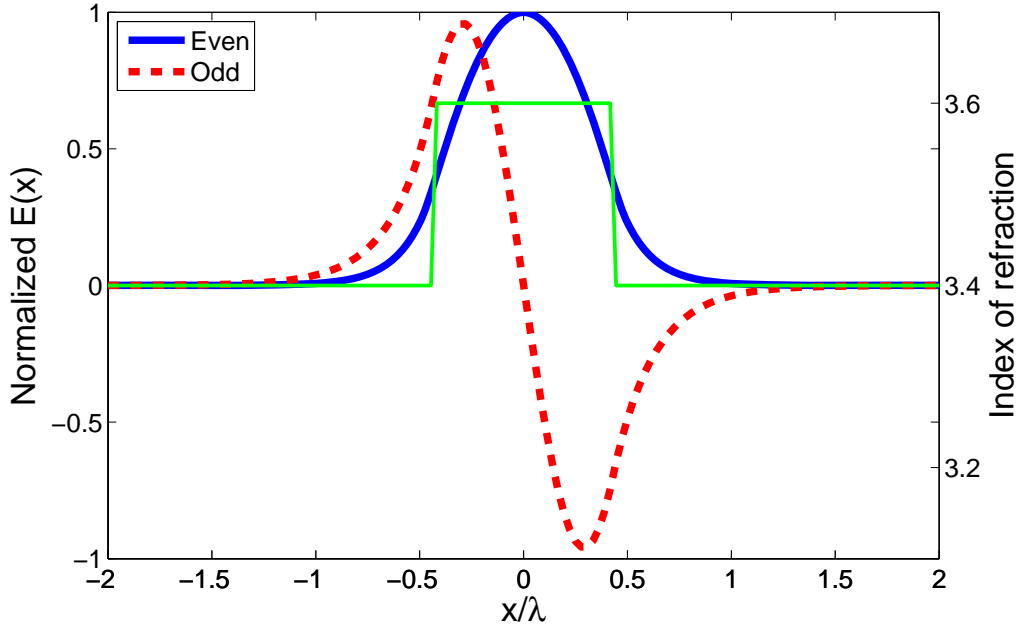


Figure 2.1: Slab waveguide solutions

for the 1-dimensional scalar case ($\partial_y E = 0$), where $k_0 \equiv \omega/c$. Both of the scalar methods start by assuming Eq. 2.4 is valid.

2.1.2 Finite Difference Eigenvalue Problem

To solve Eq. 2.4, we can rewrite it in matrix form by discretizing along some finite grid such that $x_i = (i - 1)\Delta$, for $i = 1 \dots N$, and $E_i = E(x_i)$. We discretize the ∂_x^2 operator into the $N \times N$ matrix

$$\partial_x^2 \equiv \frac{1}{\Delta^2} \begin{bmatrix} -2 & 1 & 0 & 0 & \dots & 0 \\ 1 & -2 & 1 & 0 & \dots & 0 \\ 0 & 1 & -2 & 1 & \dots & 0 \\ \dots & \dots & \dots & \dots & \dots & \dots \\ 0 & \dots & 0 & 1 & -2 & 1 \\ 0 & \dots & 0 & 0 & 1 & -2 \end{bmatrix} \quad (2.5)$$

because we note that

$$\partial_x^2 E(x) \approx \frac{E_{i+1} - 2E_i + E_{i-1}}{\Delta^2} \quad (2.6)$$

if $\Delta/\lambda \ll 1$. Here we have chosen the simple boundary condition that $E_{-1} = E_{N+1} = 0$, since we are only looking for confined solutions that should decay exponentially in the cladding. Similarly,

$$n(x)^2 k^2 \equiv k^2 \begin{bmatrix} 1 & 0 & \dots & 0 \\ 0 & 1 & \dots & 0 \\ \dots & \dots & \dots & \dots \\ 0 & \dots & 1 & 0 \\ 0 & \dots & 0 & 1 \end{bmatrix} \begin{bmatrix} n_1 \\ n_2 \\ \dots \\ n_{N-1} \\ n_N \end{bmatrix} . \quad (2.7)$$

Thus we have transformed Eq. 2.4 into an eigenvalue problem

$$\hat{M}\mathbf{E} = \lambda\mathbf{E} \quad (2.8)$$

where $\hat{M} = \partial_x^2 + n(x)^2 k^2$ as defined by Eqs. 2.5 and 2.7, $\lambda = \beta^2$, and \mathbf{E} is a column vector of all E_i . We can then use any standard eigenvalue solver to find the modes of the waveguide defined by n_i .

2.1.3 Matrix Method

Here we modify the standard matrix method[36] by explicitly including an imaginary part to the propagation constant to allow for the possibility of lossy modes. Starting from Eq. 2.4, we substitute the following definitions

$$\beta = \beta_r + i\beta_i \quad (2.9)$$

$$\epsilon = \epsilon_r + i\epsilon_i \quad (2.10)$$

to obtain

$$\partial_x^2 E(x) = \left[(\beta_r^2 + i2\beta_r\beta_i) - (\epsilon_r + i\epsilon_i)\frac{\omega^2}{c^2} \right] E(x) \quad (2.11)$$

where we have assumed that $\beta_i \ll \beta_r$ since we are looking for localized, but possibly lossy modes. The imaginary term, β_i , describes the modal propagation loss while ϵ_i describes any material loss or gain. We use an ansatz of the form,

$$E(x) = Ae^{ikx} + Be^{-ikx} \quad (2.12)$$

where again, we let

$$k = k_r + ik_i \quad (2.13)$$

($k_i \ll k_r$) to obtain

$$k_r^2 = \epsilon_r \frac{\omega^2}{c^2} - \beta_r^2 \quad (2.14)$$

$$k_i = \frac{1}{2k_r} \left(\epsilon_i \frac{\omega^2}{c^2} - 2\beta_r\beta_i \right) . \quad (2.15)$$

Eq. 2.12 holds true in each layer n . Thus, for a given homogeneous, isotropic material layer n , we have in matrix form

$$\begin{vmatrix} A_n(x_n) \\ B_n(x_n) \end{vmatrix} = \begin{vmatrix} \exp(-ik_n x_n) & 0 \\ 0 & \exp(ik_n x_n) \end{vmatrix} \begin{vmatrix} A_n(0) \\ B_n(0) \end{vmatrix}, \quad (2.16)$$

where $\Re[k_n]$ is given by Eq. 2.14 and $\Im[k_n]$ is given by Eq. 2.15. Only ϵ has dependence on the layer, and β , ω are the same for all layers. (β is parallel to the interface, and thus continuous. ω is clearly the same.) $x_n = x - x_0[n]$.

At the interface, we let the field and its derivative be continuous.

$$\begin{aligned} A_{n+1}(0) + B_{n+1}(0) &= A_n(L_n)e^{-ik_nL_n} \\ &+ B_n(L_n)e^{ik_nL_n} \end{aligned} \quad (2.17)$$

$$\begin{aligned} -ik_{n+1}A_{n+1}(0) + ik_{n+1}B_{n+1}(0) &= -ik_nA_n(L_n)e^{-ik_nL_n} \\ &+ ik_nB_n(L_n)e^{ik_nL_n} \end{aligned} \quad (2.18)$$

From this, we can immediately write the matrix form

$$\begin{aligned} &\begin{vmatrix} 1 & 1 \\ -ik_{n+1} & ik_{n+1} \end{vmatrix} \begin{vmatrix} A_{n+1}(0) \\ B_{n+1}(0) \end{vmatrix} \\ &= \begin{vmatrix} 1 & 1 \\ -ik_n & ik_n \end{vmatrix} \begin{vmatrix} \exp(-ik_nL_n) & 0 \\ 0 & \exp(ik_nL_n) \end{vmatrix} \begin{vmatrix} A_n(L_n) \\ B_n(L_n) \end{vmatrix}. \end{aligned} \quad (2.19)$$

If we define the following matrices:

$$\hat{\Phi}_n \equiv \begin{vmatrix} \exp(-ik_nL_n) & 0 \\ 0 & \exp(ik_nL_n) \end{vmatrix} \quad (2.20)$$

$$\hat{K}_n \equiv \begin{vmatrix} 1 & 1 \\ -ik_n & ik_n \end{vmatrix} \quad (2.21)$$

$$\mathbf{v}_n(x_n) \equiv \begin{vmatrix} A_n(x_n) \\ B_n(x_n) \end{vmatrix} \quad (2.22)$$

$$\mathbf{v}_N(0) = \hat{K}_N^{-1} \left(\prod_{m=1}^{N-1} \hat{K}_m \hat{\Phi}_m \hat{K}_m^{-1} \right) \hat{K}_0 \hat{\Phi}_0 \mathbf{v}_0, \quad (2.23)$$

we can define

$$\hat{M} = \begin{vmatrix} m_1 & m_2 \\ m_3 & m_4 \end{vmatrix} \equiv \hat{K}_N^{-1} \left(\prod_{m=1}^{N-1} \hat{K}_m \hat{\Phi}_m \hat{K}_m^{-1} \right) \hat{K}_0 \hat{\Phi}_0. \quad (2.24)$$

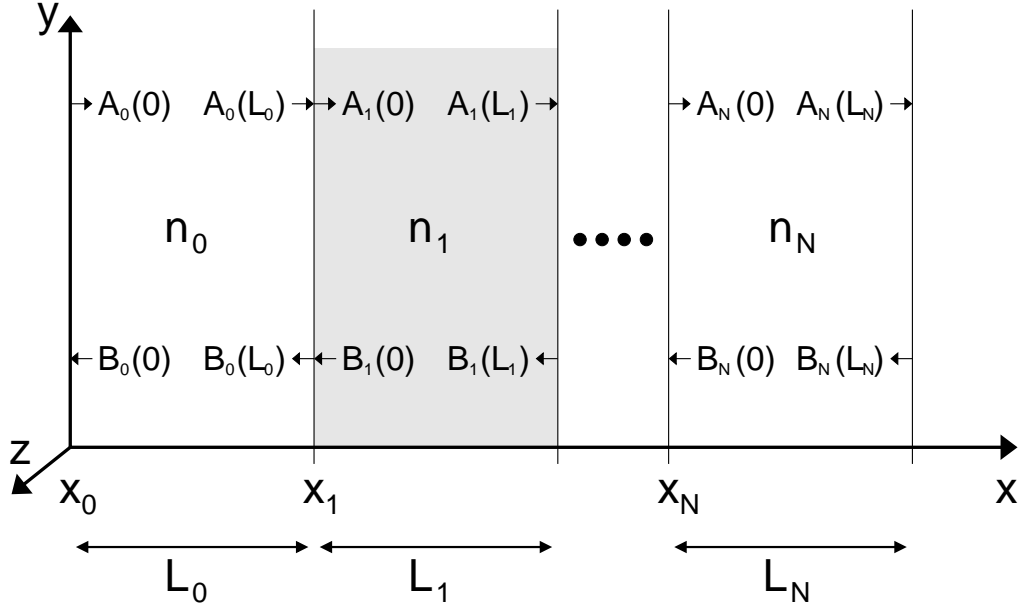


Figure 2.2: Schematic of layered media showing forward and backward travelling wave amplitudes

If we define an interface matrix

$$\begin{aligned} \hat{K}_{n+1}^{-1} \hat{K}_n &= \frac{1}{i2k_{n+1}} \begin{vmatrix} ik_{n+1} & -1 \\ ik_{n+1} & 1 \end{vmatrix} \begin{vmatrix} 1 & 1 \\ -ik_n & ik_n \end{vmatrix} \\ &= \frac{1}{2} \begin{vmatrix} 1 + \frac{k_n}{k_{n+1}} & 1 - \frac{k_n}{k_{n+1}} \\ 1 - \frac{k_n}{k_{n+1}} & 1 + \frac{k_n}{k_{n+1}} \end{vmatrix}, \end{aligned} \quad (2.25)$$

at each interface we have

$$\begin{vmatrix} A_{n+1}(0) \\ B_{n+1}(0) \end{vmatrix} = \hat{K}_{n+1}^{-1} \hat{K}_n \begin{vmatrix} A_n(L_n) \\ B_n(L_n) \end{vmatrix}. \quad (2.26)$$

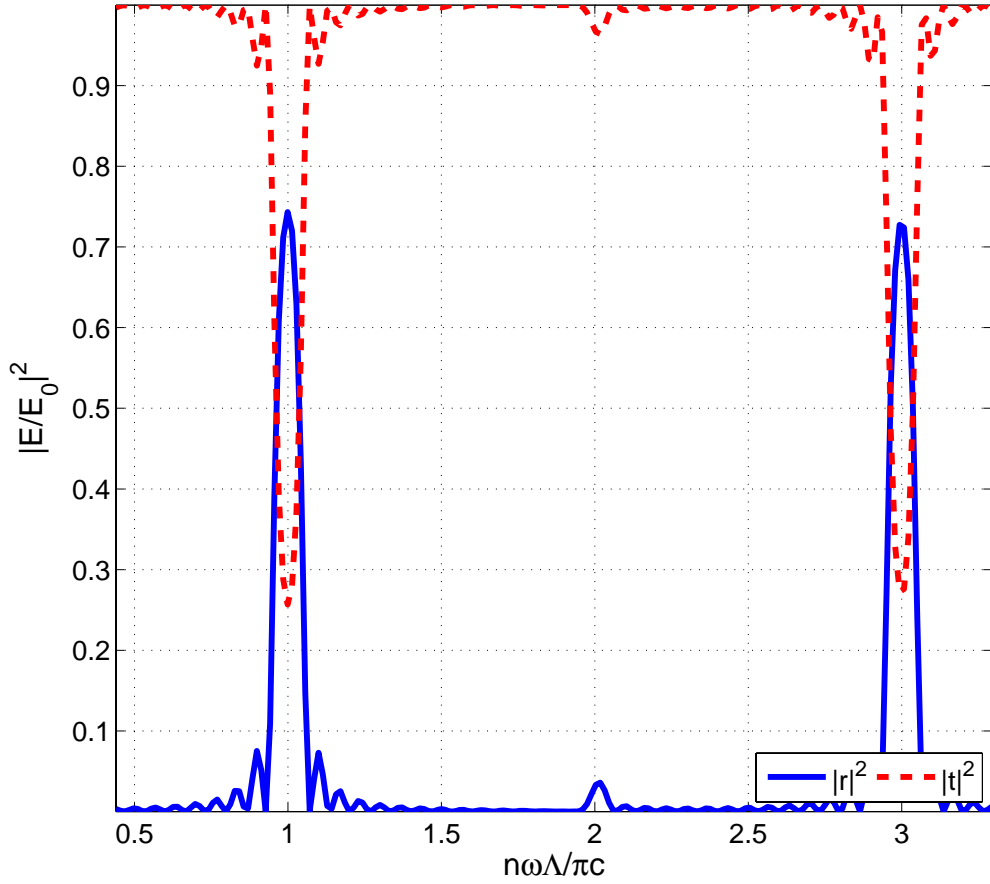


Figure 2.3: Reflection and transmission spectrum of a Bragg stack

Using Eq. 2.24, the boundary condition for a localized mode is

$$\begin{vmatrix} A_n(L_n) \\ 0 \end{vmatrix} = \hat{M} \begin{vmatrix} 0 \\ B_0(0) \end{vmatrix}, \quad (2.27)$$

since we expect outgoing waves from the structure, but nothing coming into the structure from outside the waveguide. Thus, a mode exists if it satisfies the condition

$$m_4 = 0. \quad (2.28)$$

If we let the position x_0 be the center of a symmetric structure, we can expect

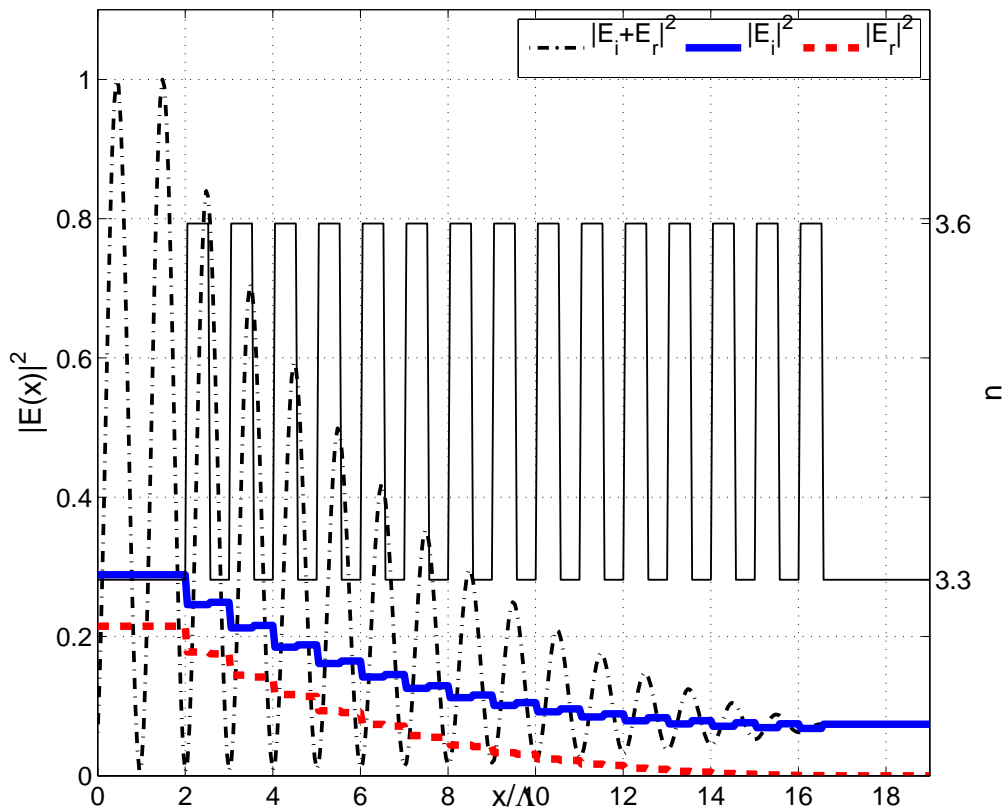


Figure 2.4: Field intensity distribution of the forward and backward waves travelling in Bragg stack of Fig. 2.3

the solutions to have even or odd symmetry about that point. This can be written as

$$\begin{vmatrix} A_n(L_n) \\ 0 \end{vmatrix} = \hat{M} \begin{vmatrix} 1 \\ 1 \end{vmatrix} \quad (2.29)$$

for even modes and

$$\begin{vmatrix} A_n(L_n) \\ 0 \end{vmatrix} = \hat{M} \begin{vmatrix} 1 \\ -1 \end{vmatrix} \quad (2.30)$$

for odd modes. Thus the condition for existence of an even mode is

$$m_3 + m_4 = 0 \quad (2.31)$$

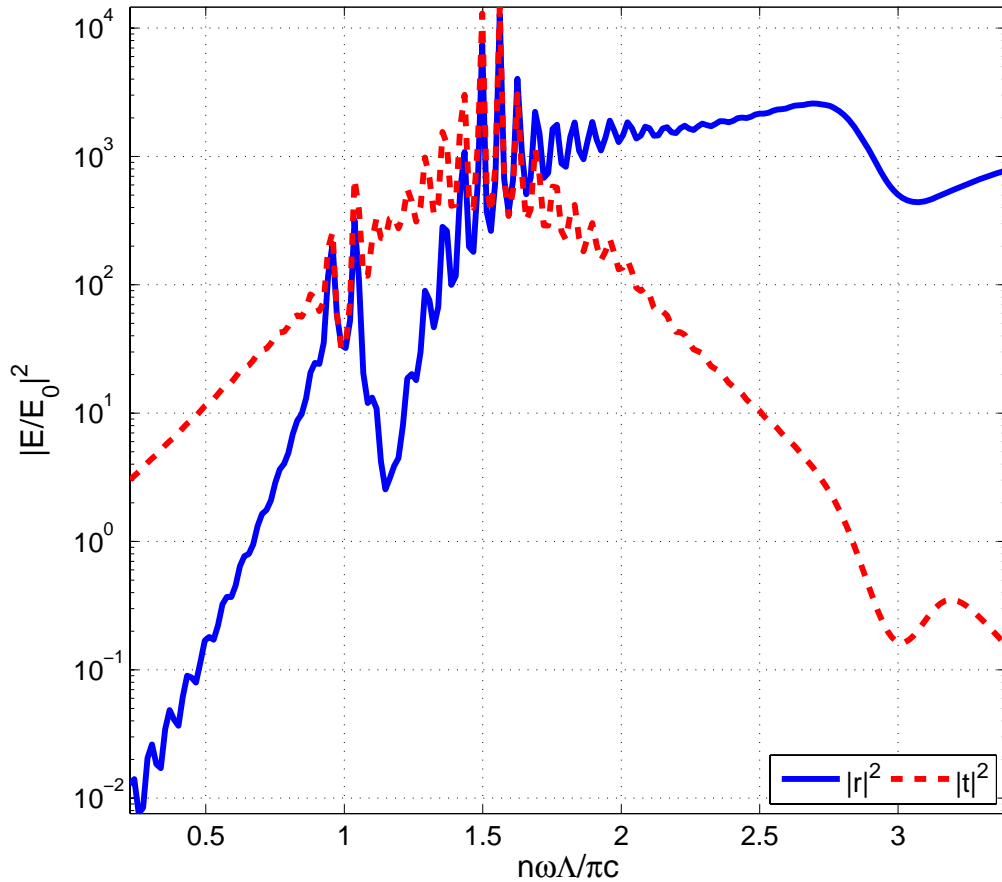


Figure 2.5: Reflection and transmission spectrum of the Bragg stack in Fig. 2.3 with gain

and

$$m_3 - m_4 = 0 \quad (2.32)$$

for odd modes. The algorithm for finding modes then becomes solving the mode equation for a given frequency, ω , to find the propagation constant(s) (the dispersion relation). For each of the modes, we can then use Eqs. 2.12 and 2.16 to calculate the field in each layer, and apply Eq. 3.54 across each boundary.

Following the convention shown in Fig. 2.2, for an incoming wave at

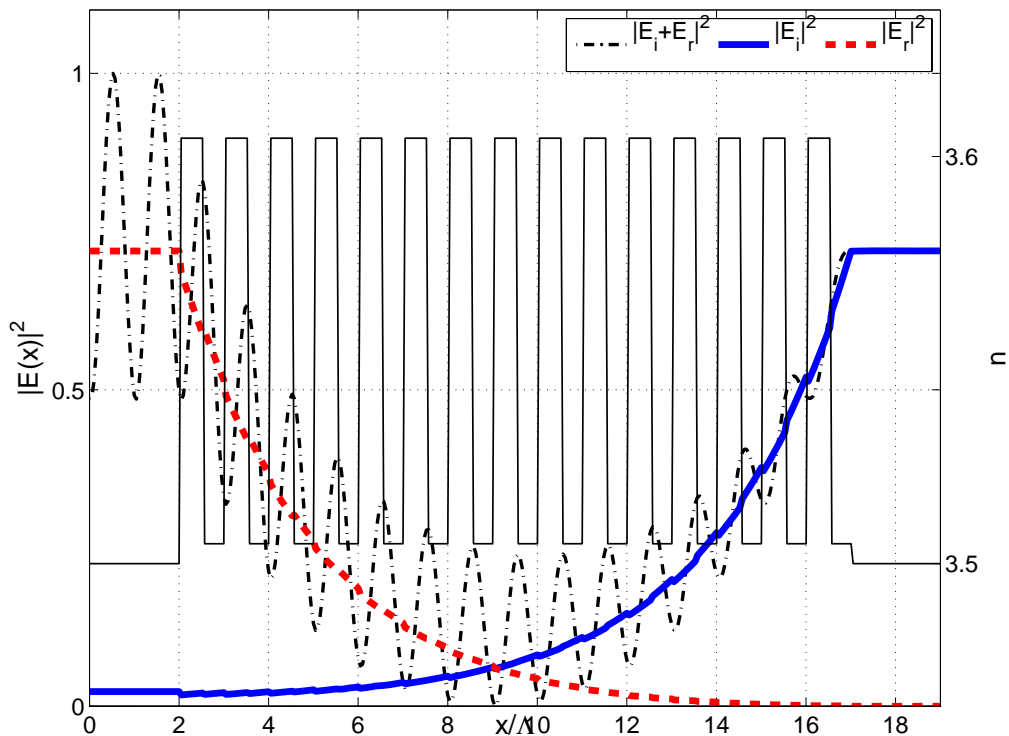


Figure 2.6: Field intensity distribution of the forward and backward waves travelling in Bragg stack of Fig. 2.5

$x = 0$

$$\begin{vmatrix} A_N \\ 0 \end{vmatrix} = \begin{vmatrix} m_1 & m_2 \\ m_3 & m_4 \end{vmatrix} \begin{vmatrix} A_0 \\ B_0 \end{vmatrix}, \quad (2.33)$$

since we should not have an incoming wave at the other boundary. In this case, the reflection is given by

$$r = -\frac{m_3}{m_4} = \frac{B_0}{A_0} \quad (2.34)$$

and the transmission is given by

$$t = m_1 - \frac{m_2 m_3}{m_4} = \frac{A_N}{A_0}. \quad (2.35)$$

To calculate the reflection or transmission of power, we use the time averaged Poynting vector, $\mathbf{S} = \mathbf{E} \times \mathbf{H}$, for plane waves. For a plane wave incident normally on the y-z plane, in keeping with our convention,

$$\mathbf{S} = \frac{1}{2} \text{Re}[\mathbf{E} \times \mathbf{H}^*] = \frac{1}{2} \text{Re}[E_y H_z^*] = \frac{\epsilon\omega}{k} \frac{1}{2} |E|^2 = \frac{1}{2\eta} |E|^2 \quad (2.36)$$

where we have made use of the fact that $k = n\omega/c$ for a normally incident plane wave, and $E \equiv E_y$, $H \equiv H_z$ for the TE-mode, and $\partial_x H_z = \epsilon \partial_t E_y$. $\eta \equiv \sqrt{\mu/\epsilon}$. For a plane wave that is not normally incident, we want

$$\mathbf{S} \cdot \hat{\mathbf{x}} = |\mathbf{S}| |\hat{\mathbf{x}}| \cos \theta = \frac{1}{2\eta} |E|^2 \frac{ck_x}{n\omega} = \frac{k_x}{2\mu\omega} |E|^2, \quad (2.37)$$

since $c/n = 1/\sqrt{\mu\epsilon}$. Thus, we have

$$R = \left| \frac{\mathbf{S}'_0 \cdot \hat{\mathbf{x}}}{\mathbf{S}_0 \cdot \hat{\mathbf{x}}} \right| = \frac{|B_0|^2}{|A_0|^2} = |r|^2 \quad (2.38)$$

$$T = \left| \frac{\mathbf{S}_N \cdot \hat{\mathbf{x}}}{\mathbf{S}_0 \cdot \hat{\mathbf{x}}} \right| = \frac{k_N |A_N|^2}{k_0 |A_0|^2} = \frac{k_N}{k_0} |t|^2 \quad (2.39)$$

Fig. 2.3 and 2.4 show the reflection and transmission spectrum for a Bragg stack and the intensity distribution while Fig. 2.5 and 2.6 show the same quantities for a Bragg stack with material gain.

2.2 Vector Approach

2.2.1 Discretizing Maxwell's Equations

To solve for the full vectorial solution of Maxwell's equations of a three dimensional system we employ the finite-difference time-domain (FDTD) method[35]. Writing out each field component of Maxwell's equations re-

sults in the following:

$$\partial_t H_x = -\frac{1}{\mu}(\partial_y E_z - \partial_z E_y) \quad \partial_t E_x = \frac{1}{\epsilon}(\partial_y H_z - \partial_z H_y) \quad (2.40)$$

$$\partial_t H_y = -\frac{1}{\mu}(\partial_z E_x - \partial_x E_z) \quad \partial_t E_y = \frac{1}{\epsilon}(\partial_z H_x - \partial_x H_z) \quad (2.41)$$

$$\partial_t H_z = -\frac{1}{\mu}(\partial_x E_y - \partial_y E_x) \quad \partial_t E_z = \frac{1}{\epsilon}(\partial_x H_y - \partial_y H_x) . \quad (2.42)$$

For each field value, the discretized value at time step n and grid location (i, j, k) is related to the continuous value by the following relation:

$$f^n(i, j, k) = f(i\Delta, j\Delta, k\Delta, n\delta t) . \quad (2.43)$$

Using Fig. 2.7, we can now explicitly write out the discretized algorithm for two components:

$$\begin{aligned} H_x^{n+1}(i, j, k) = & H_x^n(i, j, k) \\ & - \delta t \left[\left(\frac{E_z^{n+.5}(i, j+1, k) - E_z^{n+.5}(i, j, k)}{\Delta} \right) \right. \\ & \left. - \left(\frac{E_y^{n+.5}(i, j, k+1) - E_y^{n+.5}(i, j, k)}{\Delta} \right) \right] \end{aligned} \quad (2.44)$$

$$\begin{aligned} E_x^{m+1}(i, j, k) = & E_x^m(i, j, k) \\ & + \frac{1}{\epsilon} \delta t \left[\left(\frac{H_z^{m+.5}(i, j, k) - H_z^{m+.5}(i, j-1, k)}{\Delta} \right) \right. \\ & \left. - \left(\frac{H_y^{m+.5}(i, j, k) - H_y^{m+.5}(i, j, k-1)}{\Delta} \right) \right] . \end{aligned} \quad (2.45)$$

The other field components are discretized in a similar manner.

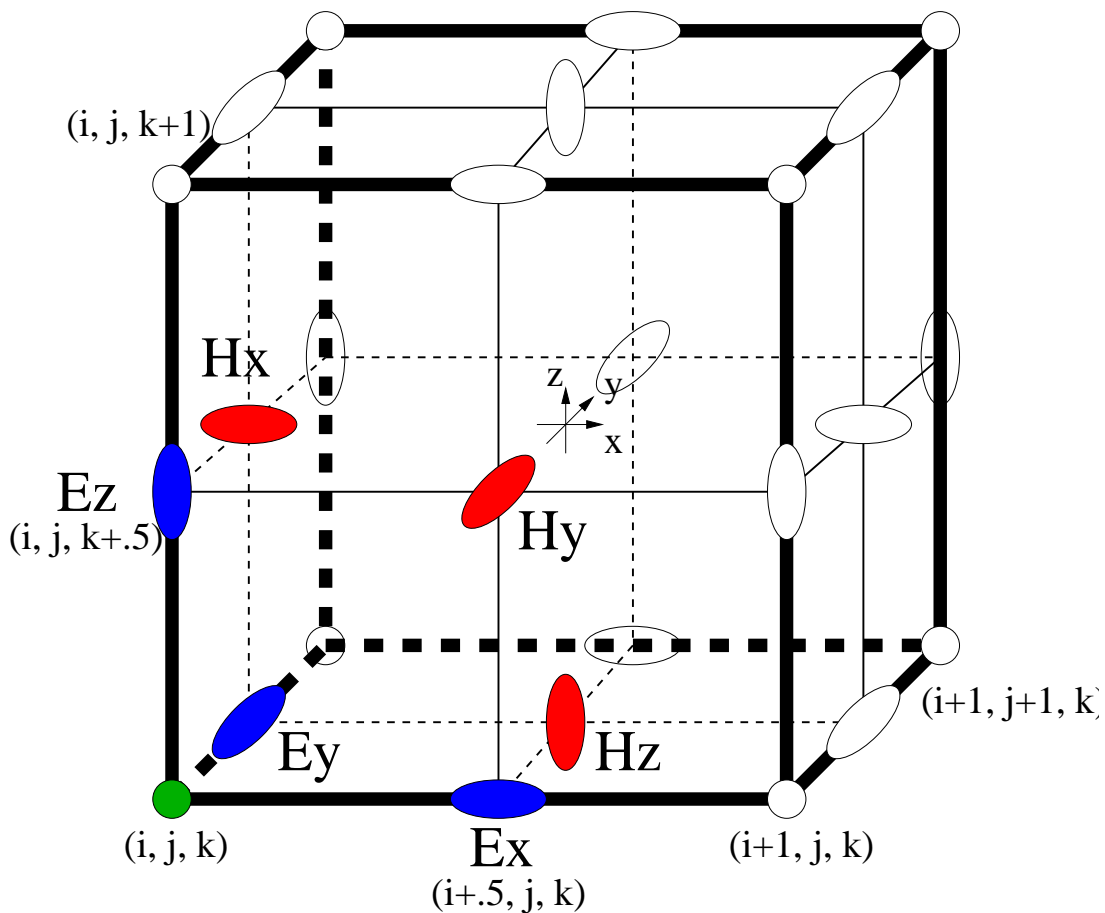


Figure 2.7: A cell of the FDTD grid

2.2.2 Boundary Conditions

Absorbing

The perfectly matched layer[3] (PML) is an absorbing boundary condition (ABC) that has high attenuation and, ideally, no reflection at the interface of the PML and non-PML layer. The specific implementation[11] used creates

an absorbing medium by introducing the vector quantity

$$[\bar{\epsilon}] = [\bar{\mu}] = \begin{bmatrix} \frac{s_y s_z}{s_x} & 0 & 0 \\ 0 & \frac{s_x s_z}{s_y} & 0 \\ 0 & 0 & \frac{s_x s_y}{s_z} \end{bmatrix} \quad (2.46)$$

$$s_x = 1 + \frac{\sigma_x}{j\omega\epsilon_0} \quad (2.47)$$

$$s_y = 1 + \frac{\sigma_y}{j\omega\epsilon_0} \quad (2.48)$$

$$s_z = 1 + \frac{\sigma_z}{j\omega\epsilon_0} , \quad (2.49)$$

into Maxwell's equations such that, in the frequency domain with normalized units ($\epsilon_0 = \mu_0 = 1$), we have

$$\nabla \times \mathbf{H} = j\omega\epsilon_r[\bar{\epsilon}]\mathbf{E} \quad (2.50)$$

$$\nabla \times \mathbf{E} = -j\omega[\bar{\mu}]\mathbf{H} . \quad (2.51)$$

Thus, for each field component we may write

$$(\nabla \times \mathbf{H})_i = j\omega \frac{s_j s_k}{s_i} \epsilon_r E_i \quad (2.52)$$

$$(\nabla \times \mathbf{E})_i = -j\omega \frac{s_j s_k}{s_i} H_i . \quad (2.53)$$

where the subscripts i , j , and k denote the field components x , y , or z . We now introduce the flux density defined as

$$D_i = \frac{s_j}{s_i} \epsilon_r E_i \quad (2.54)$$

$$B_i = \frac{s_j}{s_i} H_i \quad (2.55)$$

and substituting these into Eqs. 2.52 and 2.53 and taking the inverse Fourier transform ($j\omega \rightarrow \partial_t$), we obtain

$$(\nabla \times \mathbf{H})_i = \partial_t D_i + \sigma_k D_i \quad (2.56)$$

$$(\nabla \times \mathbf{E})_i = -\partial_t B_i + \sigma_k B_i \quad (2.57)$$

$$\partial_t D_i + \sigma_i D_i = \epsilon_r \partial_t E_i + \sigma_j \epsilon_r E_i \quad (2.58)$$

$$\partial_t B_i + \sigma_i B_i = \partial_t H_i + \sigma_j H_i . \quad (2.59)$$

Eqs. 2.56, 2.57, 2.58, and 2.59 can then be discretized in the same manner as Eqs. 2.44 and 2.45.

Bloch

The Bloch theorem[27] states that for a periodic potential, the solution should have the form

$$\mathbf{E}(\mathbf{r} + R) = \mathbf{E}(\mathbf{r})e^{ikR} \quad (2.60)$$

where R is along the direction of periodicity and k is the lattice vector. In the notation of Eq. 2.43, we thus have

$$E^n(i = N, j, k) = E^n(i = 1, j, k)e^{ik(N-1)} \quad (2.61)$$

and

$$E^n(i = 0, j, k) = E^n(i = N - 1, j, k)e^{-ik(N-1)} \quad (2.62)$$

at the boundaries.

2.2.3 Time Domain Filtering

To find the eigenfrequencies of a particular structure, we use a time domain filter[8]. Let $E(\mathbf{r}, t)$ be the electric field. Then $\tilde{E}(\mathbf{r}, j\omega)$ is the Fourier trans-

form, denoted $\tilde{E}(j\omega) = \mathcal{F}[E(t)]$. We define the Fourier transform as

$$\tilde{X}(j\omega) = \int_{-\infty}^{+\infty} x(t)e^{-j\omega t} dt , \quad (2.63)$$

and the inverse transform as

$$x(t) = \frac{1}{2\pi} \int_{-\infty}^{+\infty} \tilde{X}(j\omega)e^{j\omega t} d\omega . \quad (2.64)$$

Another definition, for convolution:

$$y(t) = \int_{-\infty}^{+\infty} h(\tau)x(t - \tau)d\tau = h(t) \otimes x(t) . \quad (2.65)$$

The following are some properties of the Fourier transform that will be used:

$$e^{j\omega_0 t} x(t) \xrightarrow{\mathcal{F}} \tilde{X}(j(\omega - \omega_0)) \quad (2.66)$$

$$\Gamma(t) = \begin{cases} 1, & |t| < T \\ 0, & |t| > T \end{cases} \xrightarrow{\mathcal{F}} 2T \frac{\sin(\omega T)}{\omega T} = 2T \text{sinc}(\omega T) \quad (2.67)$$

$$x(t) \otimes f(t) \xrightarrow{\mathcal{F}} \tilde{X}(j\omega)\tilde{F}(j\omega) \quad (2.68)$$

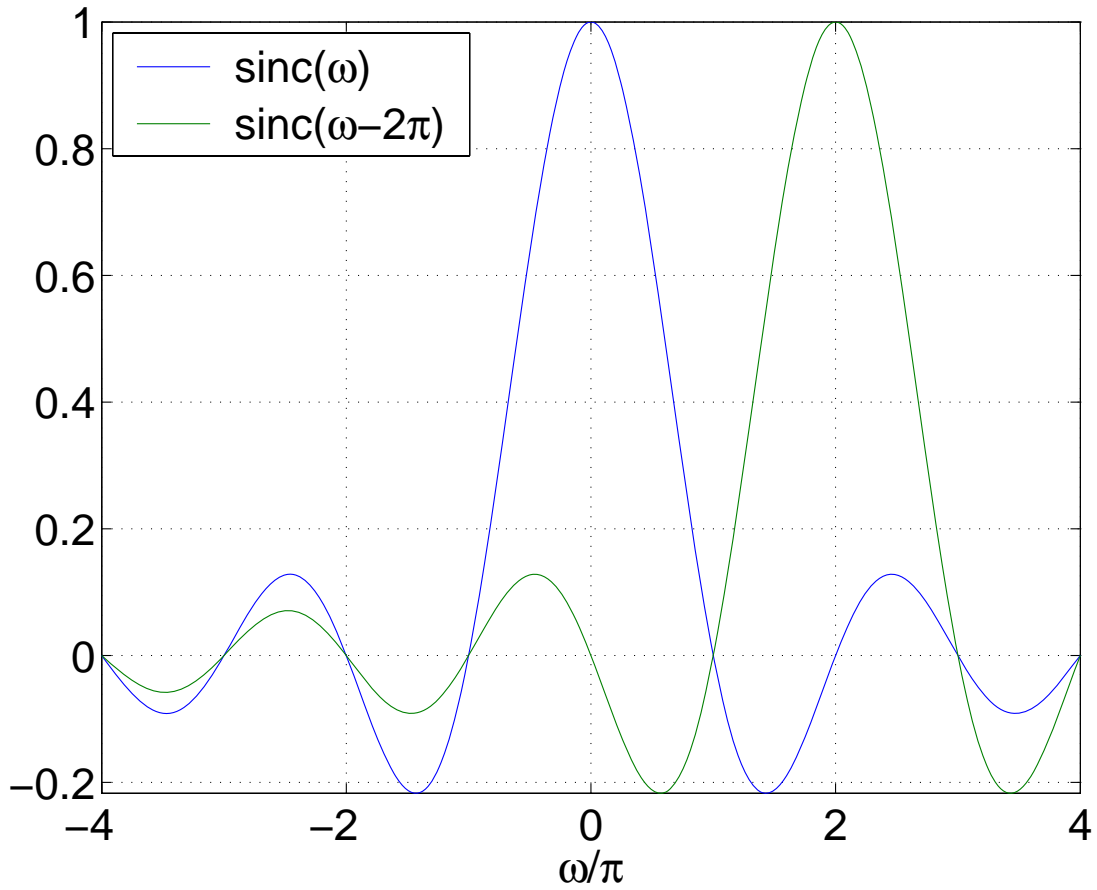
$$\sqrt{2a}e^{-at^2} \xrightarrow{\mathcal{F}} e^{-\frac{\omega^2}{4a}} . \quad (2.69)$$

Now, let us filter the frequency spectrum of our field, $\tilde{E}(j\omega)$, at some frequency ω_0 with a sinc function, $\text{sinc}(\omega - \omega_0)$. Then in time, the equivalent filter operation would be:

$$\hat{\mathbf{E}}(t) = \mathbf{E}(t) \otimes \mathcal{F}^{-1}[\text{sinc}((\omega - \omega_0)T)] = \mathbf{E}(t) \otimes \frac{1}{2T}\Gamma(t)e^{j\omega_0 t} . \quad (2.70)$$

Writing this out, we get:

$$\hat{\mathbf{E}}(t) = \int_{-\infty}^{+\infty} \mathbf{E}(\tau) \frac{1}{2T}\Gamma(t - \tau)e^{j\omega_0(t-\tau)} d\tau \quad (2.71)$$

Figure 2.8: Filter function, $\text{sinc}(\omega)$

$$\hat{\mathbf{E}}(t) = e^{j\omega_0 t} \frac{1}{2T} \int_{-\infty}^{+\infty} \mathbf{E}(\tau) \Gamma(t - \tau) e^{-j\omega_0 \tau} d\tau . \quad (2.72)$$

Now let's look closer at $\Gamma(t - \tau)$.

$$\Gamma(t - \tau) = \begin{cases} 1, & |t - \tau| < T \\ 0, & |t - \tau| > T \end{cases} \quad (2.73)$$

$$|t - \tau| < T = \begin{cases} t - \tau < T = \tau > t - T \\ -(t - \tau) < T = \tau < t + T \end{cases} \quad (2.74)$$

Thus, we get

$$\Gamma(t - \tau) = \begin{cases} 1, & t - T < \tau < t + T \\ 0, & \text{otherwise} \end{cases} . \quad (2.75)$$

Using Eq. 2.75, we get:

$$\hat{\mathbf{E}}(t) = e^{j\omega_0 t} \frac{1}{2T} \int_{t-T}^{t+T} \mathbf{E}(\tau) e^{-j\omega_0 \tau} d\tau . \quad (2.76)$$

Now we make some substitutions. First, since t is arbitrary, let $t \rightarrow T$,

$$\hat{\mathbf{E}}(T) = e^{j\omega_0 T} \frac{1}{2T} \int_0^{2T} \mathbf{E}(\tau) e^{-j\omega_0 \tau} d\tau . \quad (2.77)$$

Then, since τ is a dummy variable, let $\tau \rightarrow t$,

$$\hat{\mathbf{E}}(T) = e^{j\omega_0 T} \frac{1}{2T} \int_0^{2T} \mathbf{E}(t) e^{-j\omega_0 t} dt . \quad (2.78)$$

and we get an expression for the filtered field. The width of the central lobe of the sinc function is $\frac{2\pi}{T}$, so as T increases, $\Delta\omega \rightarrow \frac{2\pi}{T}$ and the sidelobes will decrease like $\frac{1}{T}$. The discretized version of Eq. 2.78 becomes

$$\hat{\mathbf{E}}(i, j, k) = \frac{e^{j\omega_0 T}}{2T} \sum_{n=0}^N \left[\sum_{p=0}^P \mathbf{E}^n(i, j, k) e^{-j\omega_0 \Delta t (p+1)} \right] \Delta t \quad (2.79)$$

$$N = \frac{2T\omega_0 \Delta t}{2\pi} \quad (2.80)$$

$$P = \frac{2\pi}{\omega_0 \Delta t} - 1 . \quad (2.81)$$

To implement Eq. 2.79, we need to allocate enough memory for twice the size of the total field, one for the time evolution, and one for the running sum which is the integration, or the filtered field result.

Now let us consider a Gaussian filter with the form

$$\hat{\mathbf{E}}(t) = \mathbf{E}(t) \otimes \mathcal{F}^{-1}\left[e^{j(\omega-\omega_0)t_0} e^{-\frac{(\omega-\omega_0)^2}{4a}}\right] = \mathbf{E}(t) \otimes \sqrt{2a}e^{-a(t-t_0)^2} e^{j\omega_0(t-t_0)} . \quad (2.82)$$

Writing this out, we get:

$$\hat{\mathbf{E}}(t) = \int_{-\infty}^{+\infty} \mathbf{E}(\tau) \sqrt{2a} e^{-a(t-t_0-\tau)^2} e^{j\omega_0(t-t_0-\tau)} d\tau \quad (2.83)$$

$$\hat{\mathbf{E}}(t) = e^{j\omega_0(t-t_0)} \sqrt{2a} \int_{-\infty}^{+\infty} \mathbf{E}(\tau) e^{-a(t-t_0-\tau)^2} e^{-j\omega_0\tau} d\tau . \quad (2.84)$$

Now, a Gaussian envelope is a peaked function, so when $|t| \gg T$, it becomes negligible. Hence, for a Gaussian with a central peak at $t = t_0$,

$$\hat{\mathbf{E}}(t) = e^{j\omega_0(t-t_0)} \sqrt{2a} \int_{t-t_0-T}^{t-t_0+T} \mathbf{E}(\tau) e^{-a(t-t_0-\tau)^2} e^{-j\omega_0\tau} d\tau . \quad (2.85)$$

Our signal $E(t)$ is calculated from $t = 0$ to $t = 2T$, so let us choose $t_0 = T$, and $t = 2T$.

$$\hat{\mathbf{E}}(2T) = e^{j\omega_0 T} \sqrt{2a} \int_0^{2T} \mathbf{E}(\tau) e^{-a(\tau-T)^2} e^{-j\omega_0\tau} d\tau \quad (2.86)$$

Thus, Eq. 2.86 is our filtered signal.

Energy Dissipation

The energy is assumed to have an exponential decay of the form

$$\mathcal{E}(t) = \mathcal{E}_0 e^{-\omega t/Q} , \quad (2.87)$$

where the ω is necessary since Q is supposedly defined to be a unitless number. Taking the integral,

$$\int_0^T \mathcal{E}(t) dt = \mathcal{E}_0 \frac{Q}{\omega} (1 - e^{-\omega T/Q}) , \quad (2.88)$$

hence, we can say that

$$\frac{\omega \int_0^T \mathcal{E}(t) dt}{\mathcal{E}(0) - \mathcal{E}(T)} = Q . \quad (2.89)$$

Discretizing means the integral is replaced by a discrete sum. So the discrete form becomes

$$Q = \frac{\omega \sum_0^T \mathcal{E}(t) \Delta t}{\mathcal{E}(0) - \mathcal{E}(T)} . \quad (2.90)$$

For an electromagnetic field, the energy is

$$\mathcal{E}(t) = \frac{1}{2} \int_V \epsilon |E(t)|^2 + |H(t)|^2 dV , \quad (2.91)$$

or in discrete form,

$$\mathcal{E}(t = n\Delta t) = \frac{1}{2} \Delta V \sum_{i,j,k} \epsilon |E^n(i, j, k)|^2 + |H^n(i, j, k)|^2 . \quad (2.92)$$

So the final form for the Q is,

$$Q = \frac{\omega \Delta t \sum_{n=0}^T \sum_{i,j,k} \epsilon |E^n(i, j, k)|^2 + |H^n(i, j, k)|^2}{\sum_{i,j,k} (\epsilon |E^0(i, j, k)|^2 + |H^0(i, j, k)|^2) - (\epsilon |E^T(i, j, k)|^2 + |H^T(i, j, k)|^2)} . \quad (2.93)$$

If we assume time harmonic solutions with an imaginary component to the frequency, we can relate the Q to this damping factor. In this case, the time

dependence of the electromagnetic fields can be written as

$$\mathbf{E}(\mathbf{r}, t) = \mathbf{E}(\mathbf{r})e^{-\Omega t + i\omega t} \quad (2.94)$$

$$\mathbf{H}(\mathbf{r}, t) = \mathbf{H}(\mathbf{r})e^{-\Omega t + i\omega t} . \quad (2.95)$$

Using Eqs. 2.94 and 2.95 in 2.91 and 2.87,

$$\mathcal{E}(t) = \frac{1}{2} \int_V \epsilon |E(\mathbf{r}, t)|^2 + |H(\mathbf{r}, t)|^2 dV \quad (2.96)$$

$$= \left[\frac{1}{2} \int_V \epsilon |E(\mathbf{r})|^2 + |H(\mathbf{r})|^2 dV \right] e^{-2\Omega t} \quad (2.97)$$

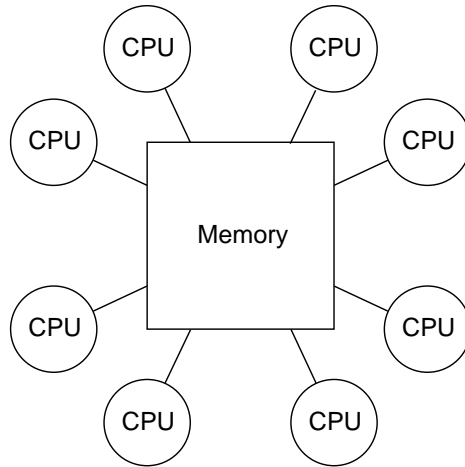
$$= \mathcal{E}_0 e^{-\omega t / Q} . \quad (2.98)$$

In other words, this means that

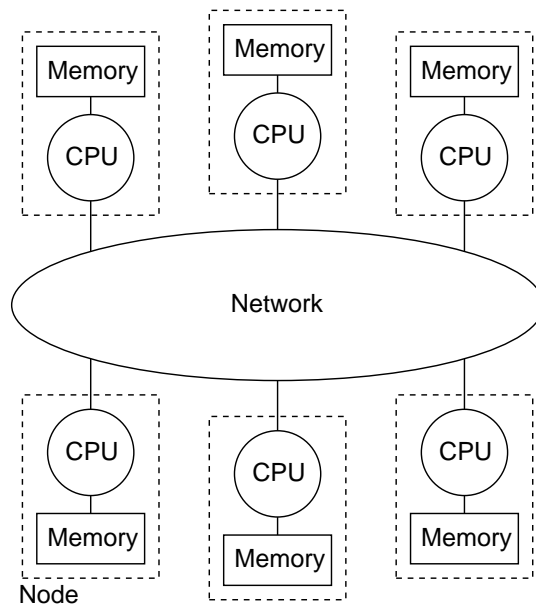
$$\Omega = \frac{\omega}{2Q} . \quad (2.99)$$

2.2.4 Parallel Implementation

To take advantage of the low cost of modern computers, we can write a parallel implementation of FDTD[13]. Parallel computing can be divided into two categories, if we consider how memory is divided among each processor (CPU). In a shared memory model, shown in Fig. 2.9(a), every processor has access to the same memory pool. Although the hardware implementation of this can be quite complex, from the programmer's perspective this means there is a single address space to consider, and changes in any memory location can be seen by all other processors without any additional considerations. Another common model, Fig. 2.9(b), is a distributed memory model, where each processor is assigned a portion of memory to which it has direct access. Any information stored in another portion of memory must be accessed by sending requests through some sort of network. The method of



(a) Shared memory



(b) Distributed memory

Figure 2.9: Two common memory models for parallel computing

network communication must be predefined-defined in some manner. In our case, we will be using the Message-Passing Interface (MPI), which is a standard programming library[25]. This distributed memory, message-passing model is particularly well suited to the cluster-of-workstations model which has become very common due to its low cost and accessibility.

The FDTD algorithm can be considered as a specialized case of the Poisson problem, $\nabla^2 u = f(x, y)$, with boundary condition $u(x, y) = g(x, y)$ [12]. Each point requires knowledge of each of the four nearest neighbors, as in Eq. 2.44 and 2.45. A simple way to address this is to allocate extra memory space to re-copy the boundaries as ghost points. Each node computes the values of its assigned domain by copying the values from each neighboring node.

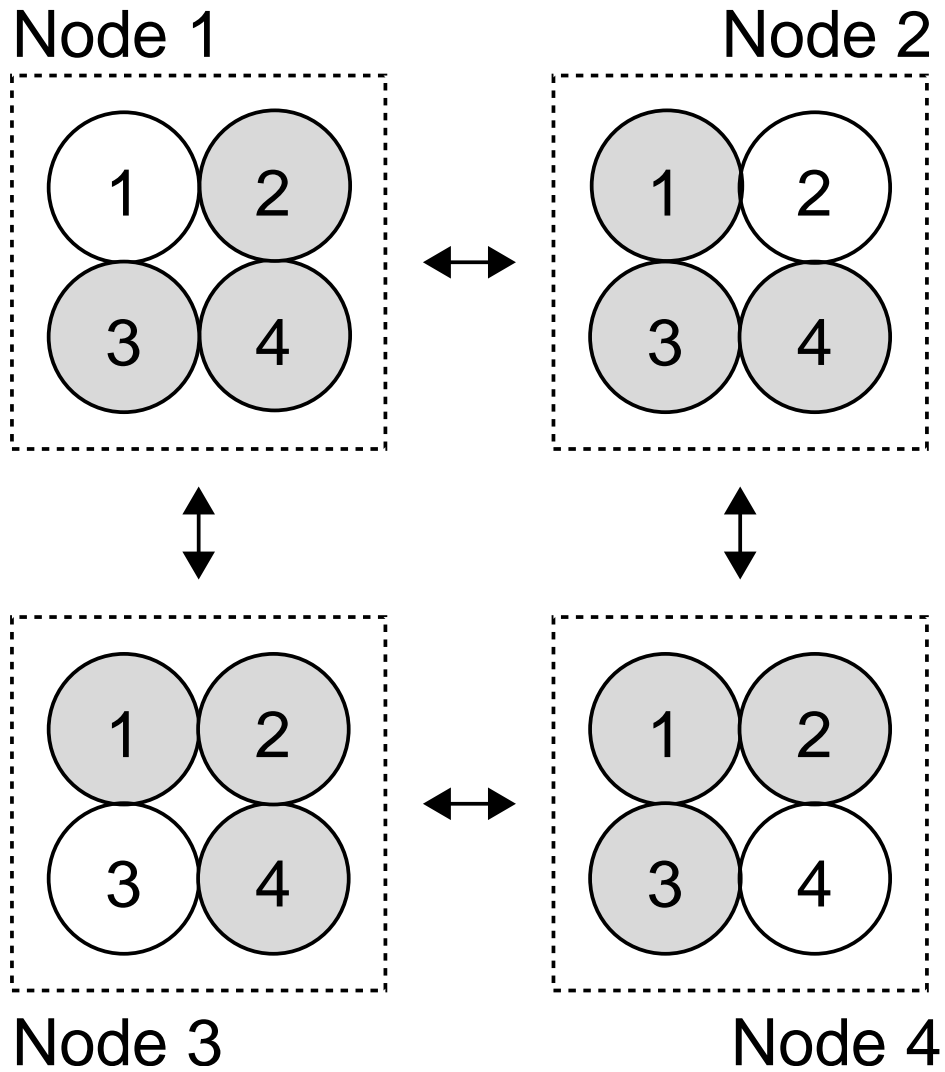


Figure 2.10: Split domain of a two dimensional topology. Ghost cells are shown shaded in gray.

Chapter 3

Waveguide Models

3.1 Index Guided Waveguides

3.1.1 Slab Waveguide Solutions

The standard method of confining light is the dielectric waveguide. This method relies on total internal reflection at an interface of two indices of refraction. Let us consider a slab waveguide as shown in Fig. 3.1. We can solve for the modes by using the 1-dimensional scalar wave equation for the electric field (TE mode) derived from Maxwell's equations by letting $\partial_y E = 0$ and by assuming travelling, time harmonic solutions, $E = E(x)\exp(i\omega t - i\beta z)$.

We assume solutions of the form

$$ae^{i\lambda x} + be^{-i\lambda x} \tag{3.1}$$

$$ce^{\gamma x} + de^{-\gamma x} \tag{3.2}$$

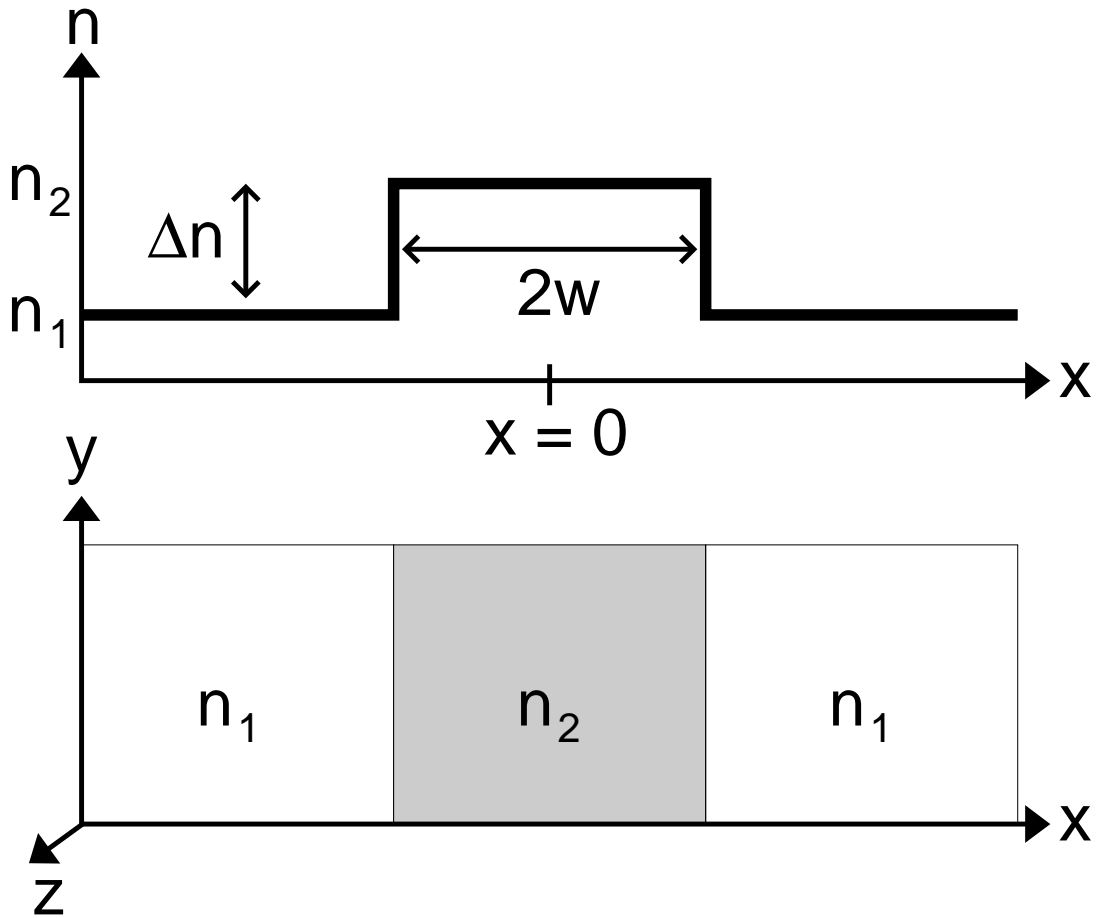


Figure 3.1: A slab waveguide

and by using symmetry we can simplify to even

$$a(e^{i\lambda x} + e^{-i\lambda x}) \quad , \quad |x| \leq w \quad (3.3)$$

$$ce^{-\gamma|x|} \quad , \quad |x| \geq w \quad (3.4)$$

and odd

$$a(e^{i\lambda x} - e^{-i\lambda x}) \quad , \quad |x| \leq w \quad (3.5)$$

$$\frac{x}{|x|} ce^{-\gamma|x|} \quad , \quad |x| \geq w \quad . \quad (3.6)$$

These solutions yield

$$\lambda^2 w^2 = n_2^2 k^2 w^2 - \beta^2 w^2 \quad (3.7)$$

$$\gamma^2 w^2 = \beta^2 w^2 - n_1^2 k^2 w^2 . \quad (3.8)$$

By enforcing the field and its derivative to be equal at the boundary $x = w$, we obtain the even solution

$$\lambda a \sin(\lambda w) = \gamma c e^{-\gamma w} \quad (3.9)$$

$$a \cos(\lambda w) = c e^{-\gamma w} \quad (3.10)$$

$$(3.11)$$

and the odd solution

$$-\lambda a \cos(\lambda w) = \gamma c e^{-\gamma w} \quad (3.12)$$

$$a \sin(\lambda w) = c e^{-\gamma w} . \quad (3.13)$$

Combining Eqs. 3.9 and 3.10 we obtain

$$\lambda w \tan(\lambda w) = \gamma w \quad (3.14)$$

and combining Eqs. 3.12 and 3.13 we obtain

$$-\lambda w \cot(\lambda w) = \gamma w \quad (3.15)$$

yielding solutions in the same form as in reference [32]. Combining Eqs. 3.7, 3.8, 3.14 and 3.15, the solutions are solved graphically in Fig. 3.2.

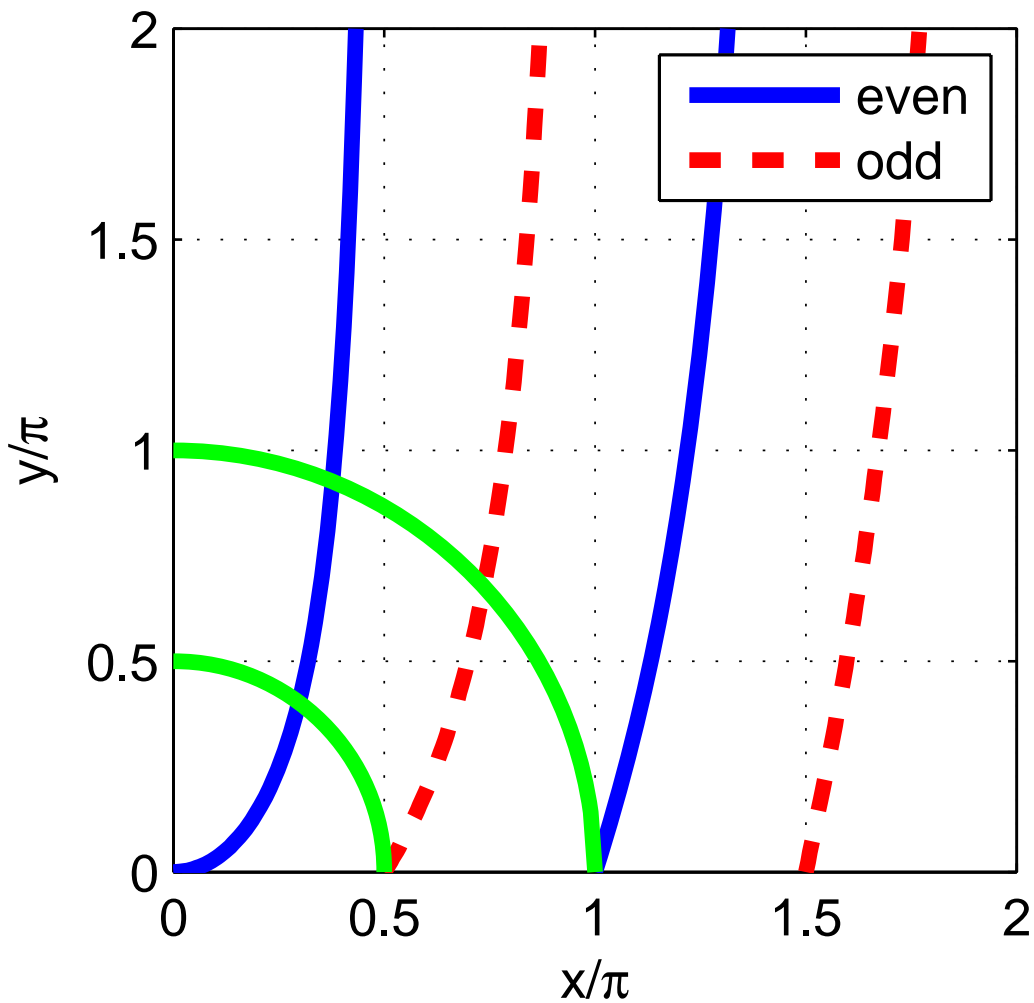


Figure 3.2: Graphical solution to the slab waveguide

3.1.2 Single Mode

Following the convention of reference [32], let

$$x = \lambda w \quad (3.16)$$

$$y = \gamma w \quad (3.17)$$

$$r = kw\sqrt{n_2^2 - n_1^2} . \quad (3.18)$$

Thus, the condition for single-mode waveguiding becomes

$$\{x, y, r\} < \pi/2 \ , \quad (3.19)$$

and we have an upper bound for the waveguide core width, $W = 2w$, of

$$W_{max} = \frac{\lambda}{2\sqrt{n_2^2 - n_1^2}} \ . \quad (3.20)$$

Since λ, γ are positive, real numbers, we also get the condition

$$n_1 < \beta/k < n_2 \ . \quad (3.21)$$

When $W = W_{max}$, there are exactly 2 modes, the first even, and the first odd. The first odd mode satisfies the condition $x = \pi/2$ yielding the following relation:

$$\beta_{odd} = n_1 k \ . \quad (3.22)$$

From Eqs. 3.20, 3.21, and 3.22, it is clear that larger core widths can be achieved by smaller index contrast, $\Delta n = n_2 - n_1$, but this also means that the even and odd modes have very similar propagation constants. This can be written explicitly in terms of the waveguide width if we define the effective index as $n_{eff} \equiv \beta/k$, and in the limit of small index contrast, $n \sim \{n_2, n_1\}$,

$$0 < \Delta n_{eff} < \frac{1}{2n} \left(\frac{\lambda}{2W} \right)^2 \ , \quad (3.23)$$

as shown in Fig. 3.3.

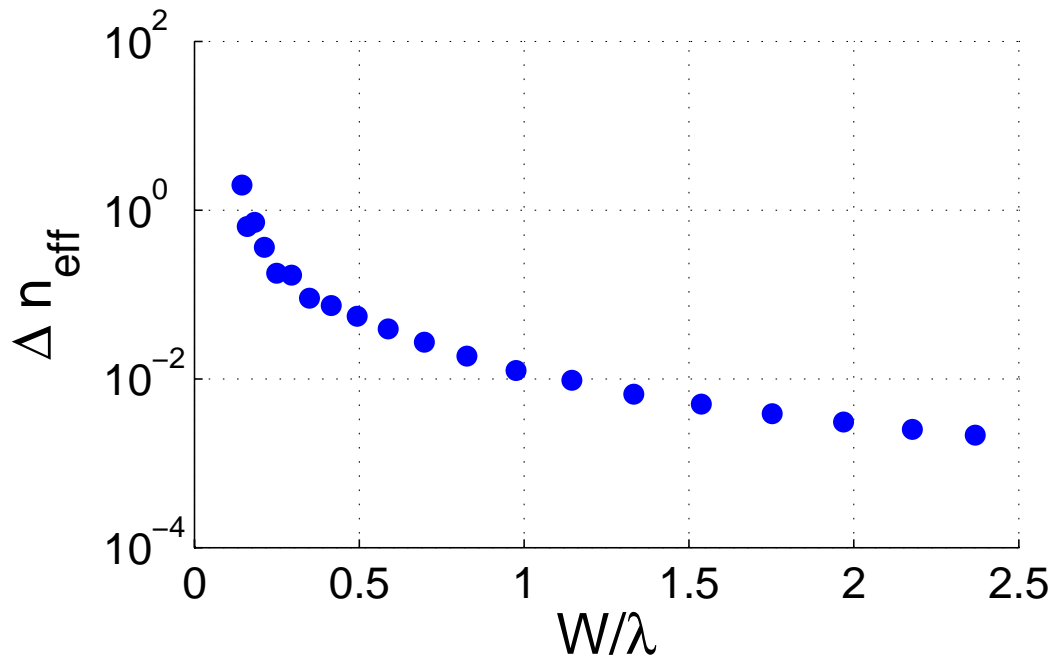


Figure 3.3: Effective index difference between the two lowest order (largest effective index) modes of a slab waveguide

3.2 Transverse Bragg Reflection

Optical waveguiding by Bragg reflection[5, 37, 38] has garnered much interest due to recent work in planar photonic crystal waveguides[7, 16, 20]. As a generalization of these photonic crystal waveguides, the transverse Bragg resonance (TBR) waveguide was recently proposed and analyzed[33]. Instead of relying on time-consuming numerical solutions to Maxwell's equations[10, 23], a coupled mode formalism was applied to calculate the dispersion and loss of a TBR waveguide composed of a GaAs substrate with air holes[6]. The results of the coupled mode analysis predict discrete, quantized values for the width of the guiding channel for achieving low loss (TBR) waveguides. Comparisons to two dimensional finite-difference time-domain (2D FDTD) simulations indicate that the coupled mode theory can provide a valid model

of the waveguiding in a TBR waveguide even with a large index contrast and, using an empirical coupling constant, can quantitatively describe the propagation of the guided modes.

3.2.1 Coupled Mode Analysis of Bragg Layers

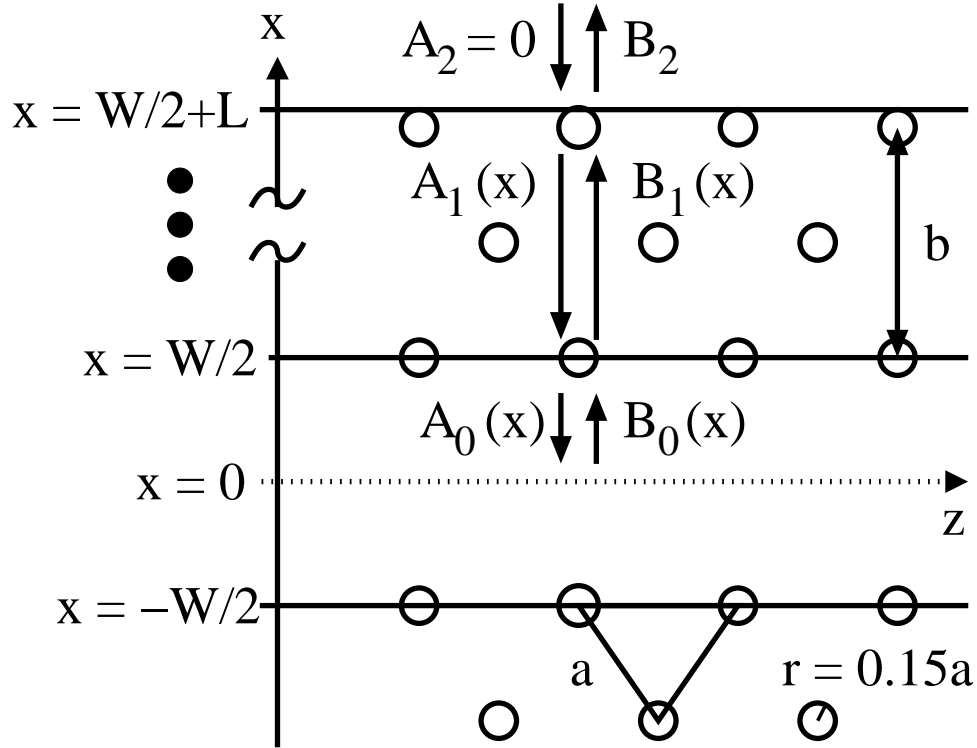


Figure 3.4: The TBR waveguide geometry consisting of a GaAs substrate and air holes. x and z are the transverse and longitudinal dimensions, respectively. The core width is W . The hole radius is $r = 0.15a$. A_0 and A_1 represent the inward propagating plane-wave components in the core and cladding respectively. A_2 represents the incoming field outside the cladding. B_0 , B_1 , and B_2 represent similar quantities for the outward propagating components.

The waveguide geometry is shown in Fig. 3.4. Assuming a small in-

dex perturbation, the propagating field can be described by the Helmholtz equation:

$$\nabla^2 \mathbf{E} + \mu \epsilon(\mathbf{r}) \omega^2 \mathbf{E} = 0 \quad , \quad (3.24)$$

describing the \mathbf{E} field out of the plane, corresponding to a TM-like mode in a photonic crystal. Although the dielectric constant, $\epsilon(\mathbf{r})$, can be complex[34], we will only consider the passive case where $\epsilon(\mathbf{r})$ is purely real. We assume a solution of the form

$$\mathbf{E}(\mathbf{r}, t) = E(x)E(z, t) = (A(x)e^{ik_b x} + B(x)e^{-ik_b x}) e^{i\omega t - i\beta z} \quad , \quad (3.25)$$

where the propagation constant is a complex quantity, $\beta = \beta_R + i\beta_I$, allowing the imaginary part of β to account for the propagation loss due to leakage through a finite cladding. Although this has the same form as Eq. 2.12, since we are analyzing Bragg layers, we note that $k_b \neq k_\perp$, but rather should satisfy the Bragg condition, as we shall see later. We have also allowed the coefficients A and B to be functions of x . We start with Eq. 2.11 and substitute our guess for $E(x)$ from Eq. 3.25. We obtain:

$$\begin{aligned} & [\partial_x^2 + 2ik_b \partial_x - k_b^2] A(x)e^{ik_b x} + [\partial_x^2 - 2ik_b \partial_x - k_b^2] B(x)e^{-ik_b x} \\ & = \left(\beta^2 - \epsilon(\mathbf{r}) \frac{\omega^2}{c^2} \right) (A(x)e^{ik_b x} + B(x)e^{-ik_b x}) \quad . \end{aligned} \quad (3.26)$$

This assumes that although the real part of the dielectric constant (index of refraction) may depend on position, the imaginary part corresponding to material gain or loss is either constant, or small compared to the changes in the index. Assuming that $|\beta_I| \ll |\beta_R|$ (low loss) and $|\partial^2/\partial x^2| \ll |2k\partial/\partial x|$ (the slowly varying approximation) and using our previous definitions Eqs.

2.9 and 2.10, we obtain

$$\begin{aligned} & \left[\epsilon(\mathbf{r}) \frac{\omega^2}{c^2} - \beta_r^2 - k_b^2 + i \left(2k_b \partial_x + \epsilon_i \frac{\omega^2}{c^2} - 2\beta_r \beta_i \right) \right] A(x) e^{ik_b x} \\ & + \left[\epsilon(\mathbf{r}) \frac{\omega^2}{c^2} - \beta_r^2 - k_b^2 + i \left(-2k_b \partial_x + \epsilon_i \frac{\omega^2}{c^2} - 2\beta_r \beta_i \right) \right] B(x) e^{-ik_b x} = 0 \end{aligned} \quad (3.27)$$

Now, we multiply by the rapidly varying term, $\exp(-ik_b x)$, and integrate over a unit cell to get

$$\begin{aligned} & \left[\epsilon_r \frac{\omega^2}{c^2} - \beta_r^2 - k_b^2 + i \left(2k_b \partial_x + \epsilon_i \frac{\omega^2}{c^2} - 2\beta_r \beta_i \right) \right] A(x) \\ & = -A(x) \frac{\omega^2}{c^2} \frac{1}{a} \int_a \Delta\epsilon(\mathbf{r}) da - B(x) \frac{\omega^2}{c^2} \frac{1}{a} \int_a \Delta\epsilon(\mathbf{r}) e^{-i2k_b x} da \end{aligned}, \quad (3.28)$$

where we have defined $\epsilon(\mathbf{r}) = \epsilon_r + \Delta\epsilon(\mathbf{r})$, and assumed that $|\int_L \exp(-i2k_b x) dx| \ll L$. We now note that

$$\int_a \Delta\epsilon(\mathbf{r}) da = \delta\bar{\epsilon}, \quad (3.29)$$

which is the dc term in a Fourier expansion. Thus,

$$\bar{\epsilon}_r \equiv \epsilon_r + \delta\bar{\epsilon} \quad (3.30)$$

is a measure of the spatially averaged dielectric constant, and for the Bragg layers we define

$$k_r^2 \equiv \bar{\epsilon}_r \frac{\omega^2}{c^2} - \beta_r^2 \quad (3.31)$$

in contrast to Eq. 2.14.

$$\begin{aligned} \partial_x A(x) & = \left[i \frac{k_r^2 - k_b^2}{2k_b} - \frac{1}{2k_b} \left(\epsilon_i \frac{\omega^2}{c^2} - 2\beta_r \beta_i \right) \right] A(x) \\ & + iB(x) \frac{k_0^2}{2k_b} \frac{1}{a} \int_a \Delta\epsilon(\mathbf{r}) e^{-i2k_b x} da \end{aligned} \quad (3.32)$$

To simplify, we now make some definitions. The loss term

$$\gamma = \frac{1}{2k_b} \left(\epsilon_i \frac{\omega^2}{c^2} - 2\beta_r \beta_i \right) , \quad (3.33)$$

the detuning from resonance

$$\Delta k = k_r - k_b , \quad (3.34)$$

and the coupling constant

$$\kappa = \frac{k_0^2}{2k_b} \frac{1}{a} \int_a \Delta \epsilon(\mathbf{r}) e^{-i2k_b x} dx dz . \quad (3.35)$$

We also note that $k_r - k_b \leq \kappa$ and $\kappa/k_b \ll 1$, since $\kappa/k_b \sim (n\Delta\omega/c)/(n\omega/c) = \Delta\omega/\omega \ll 1$ within the bandgap. From this, we get

$$\frac{k_r^2 - k_b^2}{2k_b} = (k_r - k_b) \frac{k_r + k_b}{2k_b} \approx k_r - k_b . \quad (3.36)$$

Using Eqs. 3.33, 3.34, 3.35, 3.36 in Eq. 3.32, we finally get:

$$\partial_x A(x) = -(\gamma - i\Delta k)A(x) + i\kappa B(x) . \quad (3.37)$$

If we multiply Eq. 3.27 by $\exp(ik_b x)$ and integrate, we obtain a similar equation for $\partial_x B(x)$.

$$\partial_x B(x) = (\gamma - i\Delta k)B(x) - i\kappa A(x) . \quad (3.38)$$

We have thus obtained the coupled mode equations, here presented in matrix form:

$$\frac{\partial}{\partial x} \begin{pmatrix} A(x) \\ B(x) \end{pmatrix} = \begin{pmatrix} -(\gamma - i\Delta k) & i\kappa \\ -i\kappa & (\gamma - i\Delta k) \end{pmatrix} \begin{pmatrix} A(x) \\ B(x) \end{pmatrix} . \quad (3.39)$$

We now need to solve this equation to find the form of $A(x)$ and $B(x)$.

We assume solutions of the form $c_+ \mathbf{v}_+ \exp(sx) + c_- \mathbf{v}_- \exp(-sx)$. Thus, we look for

$$\det \begin{vmatrix} -(\gamma - i\Delta k) - s & i\kappa \\ -i\kappa & (\gamma - i\Delta k) - s \end{vmatrix} = 0 \quad (3.40)$$

and we obtain

$$s = \sqrt{|\kappa|^2 + (\gamma - i\Delta k)^2} \quad (3.41)$$

and

$$\mathbf{v}_\pm = \begin{vmatrix} (\gamma - i\Delta k) \mp s \\ i\kappa \end{vmatrix}. \quad (3.42)$$

We define the matrix:

$$\hat{V} = \begin{vmatrix} (\gamma - i\Delta k) - s & (\gamma - i\Delta k) + s \\ i\kappa & i\kappa \end{vmatrix}. \quad (3.43)$$

The constants c_\pm are dependent on the initial conditions $A(0)$, $B(0)$, so we finally get

$$\begin{vmatrix} A(x) \\ B(x) \end{vmatrix} = \hat{V} \begin{vmatrix} e^{sx} & 0 \\ 0 & e^{-sx} \end{vmatrix} \hat{V}^{-1} \begin{vmatrix} A(0) \\ B(0) \end{vmatrix}. \quad (3.44)$$

If we simplify the above equation, we obtain

$$\begin{vmatrix} A(x) \\ B(x) \end{vmatrix} = \begin{vmatrix} -\frac{(\gamma - i\Delta k)}{s} \sinh(sx) + \cosh(sx) & \frac{i\kappa}{s} \sinh(sx) \\ -\frac{i\kappa}{s} \sinh(sx) & \frac{(\gamma - i\Delta k)}{s} \sinh(sx) + \cosh(sx) \end{vmatrix} \begin{vmatrix} A(0) \\ B(0) \end{vmatrix}, \quad (3.45)$$

in comparison to Eq. 2.16.

Let us look at the example of a one-dimensional grating. If we center the origin such that

$$\Delta\epsilon(x) = \begin{cases} 0 & \Lambda/4 < |x| \leq \Lambda/2, \\ \Delta\epsilon & 0 \leq |x| \leq \Lambda/4. \end{cases}, \quad (3.46)$$

in this case, Eq. 3.35 reduces to:

$$\kappa = \frac{k_0^2}{2k_b} \frac{\Delta\epsilon}{\Lambda} \int_{-\Lambda/4}^{\Lambda/4} e^{-i2k_b x} dx = \frac{k_0^2}{2k_b^2} \frac{\Delta\epsilon}{\Lambda} \sin(k_b \Lambda/2) = \frac{k_0^2 \Delta\epsilon}{2k_b^2 \Lambda}. \quad (3.47)$$

For the simple case of plane waves, we know that at the Bragg resonance $k_b = \pi/\Lambda$ and $k_b/k_0 = n \cos \theta$, so we can then get

$$\kappa \approx \frac{\Delta\epsilon}{2n^2 \Lambda \cos^2 \theta} = \frac{(n_2 - n_1)(n_2 + n_1)}{2n^2 \Lambda \cos^2 \theta} \approx \frac{\Delta n}{n \Lambda \cos^2 \theta} = \frac{\omega_0}{c\pi} \frac{\Delta n}{\cos \theta}, \quad (3.48)$$

where ω_0 is at the center of the bandgap. Eq. 3.48 is useful for insight into the relation between the bandgap, the index contrast, and the angle of incidence. The bandwidth of the gap can be obtained from Eq. 3.41 since our mode is defined only when $\Im[s] = 0$. This condition means that the value under the square root must be greater than zero. Thus, we can find the bandwidth by solving

$$\Delta k^2 + i2\gamma\Delta k - \gamma^2 - |\kappa|^2 = 0 \quad (3.49)$$

and using $n\Delta\omega = c\Delta k$. Solving this quadratic in Δk , we get

$$|\Delta k| = \pm \sqrt{|\kappa|^2 + \gamma^2}. \quad (3.50)$$

For the case of no loss or gain, $\gamma = 0$, we get

$$\Delta k_{\text{gap}} = 2\Delta k = \frac{2\omega_0}{c\pi \cos \theta} \Delta n \quad (3.51)$$

$$\Delta \omega_{\text{gap}} = \frac{c}{n} 2\Delta k = \frac{2c|\kappa|}{n} = \frac{2\omega_0}{\pi \cos \theta} \frac{\Delta n}{n} . \quad (3.52)$$

3.2.2 Transverse Bragg Resonance Waveguides

We can now use the above results along with the results from Chapter 2 to analyze a TBR waveguide. Let us define a TBR waveguide as being composed of a waveguide core of some width, W , and a cladding on either side composed of Bragg layers. We then proceed to solve the Helmholtz equation separately in the uniform core and the periodic cladding. We assume plane wave solutions, $E(x) = A \exp(ikx) + B \exp(-ikx)$, but require that the wave vector satisfy

$$k = \begin{cases} k_b = \frac{2\pi}{b} & \text{cladding} \\ k_W = [\bar{\epsilon} \frac{\omega^2}{c^2} - \beta_R^2]^{1/2} & \text{core} \end{cases} . \quad (3.53)$$

Eq. (3.39) is solved separately in the core ($\kappa = 0$, $\Delta k = 0$), and cladding and the field and its derivative are required to be continuous at the interface to obtain a piecewise continuous solution.

The mirror symmetry with respect to the center of the core ($x = 0$) allows the modes to be classified by their parity: even, $A_0(0) = B_0(0)$, and odd, $A_0(0) = -B_0(0)$. At the outer edge of the cladding, we observe that $A_2(W/2 + L) = 0$, and $B_2(W/2 + L)$ should be minimized.

In the core $\kappa = 0$ and $\Delta k = 0$. At the interface between the core and

cladding, requiring continuity of the field and its derivative leads to

$$\begin{aligned} \left| \begin{array}{c} A_1(W/2) \\ B_1(W/2) \end{array} \right| &= \\ \frac{1}{2} \left| \begin{array}{cc} \left(1 + \frac{k_W}{k_b}\right) e^{ik_W W/2} & \left(1 - \frac{k_W}{k_b}\right) e^{-ik_W W/2} \\ \left(1 - \frac{k_W}{k_b}\right) e^{ik_W W/2} & \left(1 + \frac{k_W}{k_b}\right) e^{-ik_W W/2} \end{array} \right| & \left| \begin{array}{c} A_0(W/2) \\ B_0(W/2) \end{array} \right|, \end{aligned} \quad (3.54)$$

where A_1 , B_1 , and A_0 , B_0 are defined by Fig. 3.4. Using Eq. (3.39)-(3.54) we can now solve for an analytic expression for the transverse field of a guided mode, and consider how the waveguide design affects the loss due to leakage through the cladding layer.

Solving Eq. (3.39) in the cladding when $x > 0$ yields a solution[33] of the form

$$\begin{aligned} \left| \begin{array}{c} A(x + x_0) \\ B(x + x_0) \end{array} \right| &= \\ \left| \begin{array}{cc} -\frac{(\gamma - i\Delta k)}{S} \sinh(SL) + \cosh(SL) & \frac{\kappa}{S} \sinh(SL) \\ \frac{\kappa^*}{S} \sinh(SL) & \frac{(\gamma - i\Delta k)}{S} \sinh(SL) + \cosh(SL) \end{array} \right| & \left| \begin{array}{c} A(x_0) \\ B(x_0) \end{array} \right|. \end{aligned} \quad (3.55)$$

where $S = (|\kappa|^2 + (\gamma - i\Delta k)^2)^{1/2}$. For the cladding region when $x > 0$, $x_0 = W/2$. Applying the boundary conditions at the center of the core ($A_0(0)$, $B_0(0)$), and the outer edge of the cladding ($A_2(W/2 + L)$, $B_2(W/2 + L)$), and requiring continuity at the core-cladding interface, Eq. 3.54, we solve numerically for the modal solutions. For the greatest confinement, and consequently the least loss, the transverse wave vector, k , should be near the center of the Bragg resonance, so $k_W \sim k_b$ or $\Delta k \sim 0$. Also, as L increases, the leakage field $B_2(L + W/2)$ becomes smaller, thus reducing the loss.

Using Eq. 2.34 and Eq. 3.45, we get the reflection coefficient as

$$r = \frac{i\kappa}{(\gamma - i\Delta k) + s \coth(sL)} . \quad (3.56)$$

Since the field must be continuous, we can equate the outgoing field in the core to the outgoing field in the cladding, and do likewise for the incoming field at the core-cladding boundary. At the boundary, the field at the cladding is given by

$$E(x = W/2) = A_0 e^{-ikW/2} + B_0 e^{ikW/2} , \quad (3.57)$$

where A_0 , B_0 are the initial outgoing and incoming field amplitudes at the core center and in the cladding,

$$E(x = W/2) = A_1 e^{-ik_b \cdot 0} + r A_1 e^{ik_b \cdot 0} . \quad (3.58)$$

From this, we get

$$r = \frac{B_0}{A_0} e^{ikW} . \quad (3.59)$$

We can then use symmetry to classify the modes as even, $B_0/A_0 = 1$, or odd, $B_0/A_0 = -1$. This expression will give us insight into the core width. We must take a closer look at the phase of Eq. 3.56. First, we recast it into the form

$$r = \frac{-\kappa\Delta k + i\kappa(\gamma + s \coth(sL))}{(\gamma + s \coth(sx))^2 + \Delta k^2} = |r| e^{i\phi_r} \quad (3.60)$$

and then the phase can be easily seen to be

$$\phi_r = \tan^{-1} \left(-\frac{\gamma + s \coth(sL)}{\Delta k} \right) . \quad (3.61)$$

Since any guided mode of the TBR waveguide should be within the bandgap, we know that $\Delta k < |\kappa|$ (Eq. 3.50), and in the limit of a very long cladding ($\kappa L \gg 1$) and low loss ($\gamma \ll 1$) the numerator goes to κ . Thus, we can Taylor

expand about the point $\Delta k = 0$. (We acknowledge that s is a function of Δk , but if $\Delta k < \kappa$, then $\Delta k^2 \ll \kappa^2$.) Making use of the fact that $d/du \tan^{-1} u = du/(1+u^2)$ [30]

$$\phi_r \approx \frac{\pi}{2} + \frac{\Delta k}{\gamma + s \coth(sL)} \quad (3.62)$$

to first order. The phase relation is then

$$kW - \phi_r = m\pi \quad , \quad (3.63)$$

with $m = 0, 2, 4, \dots$ for even modes and $m = 1, 3, 5, \dots$ for odd modes. We now recognize that $k \approx \pi/\Lambda$ near Bragg resonance so that

$$W = \Lambda \left(m + \frac{1}{2} + \frac{\Delta k/\pi}{\gamma + s \coth(sL)} \right) \quad . \quad (3.64)$$

At the Bragg resonance, $\Delta k = 0$, and we get $W = \Lambda/2$ for the lowest order even mode, corresponding to the familiar $\lambda/4$ phase slip in a DFB grating, and $W = 3\Lambda/2$ for the lowest order odd mode.

Let us restrict ourselves to the lowest order even mode. In the limit of $\kappa L \gg 1$ (many Bragg layers) and $\gamma \ll \kappa$ (low loss), we get

$$W = \Lambda \left(\frac{1}{2} + \frac{\Delta k}{\pi|\kappa|} \right) \quad , \quad (3.65)$$

which indicates that the greater the grating strength (κ), the less sensitive the core width is to detuning from Bragg resonance. ($\lim_{x \rightarrow \infty} \coth(x) = 1$)

This shows that the phase matching condition within the waveguide core restricts the width to discrete values. In the next section, we examine how deviation from the phase matched condition affects the propagation loss using a FDTD numerical simulation.

3.2.3 Simulation Results

Since a single transverse even mode is desirable for telecom applications, we study a case with a core width of $W = b/4$. For our 2D FDTD simulations, the domain is composed of an even mirror boundary condition at $x = 0$, Bloch boundary conditions at $z = 0$ and $z = a$, i.e. $E(z = a) = E(z = 0) \exp(i\beta a)$, and an absorbing perfectly matched layer [11] at the outer edge of the simulation domain as shown in Fig. 3.5.

The cladding structure simulated was composed of approximately ten unit cell layers. The hole radius was $r = 0.15a$, which is smaller than photonic bandgap crystals ($r \approx 0.3a - 0.4a$)[31]. When the core width, W , is $b/4$, the field envelope decays as $E(x) \sim \exp(-|\kappa|x)E_0$. Fig. 3.6 shows the transverse field profile decay calculated using the 2D FDTD simulation along with the exponentially decaying envelope predicted by Coupled Mode theory with κ calculated from Eq. (3.35). Also shown is the theoretical curve with a κ chosen to fit the FDTD results. The theoretical κ calculated from Eq. (3.35) is $\kappa = -i0.1475/a$ while the empirical κ found from the fit shown in Fig. 3.6 was $\kappa = -i0.1100/a$. As we shall see, this single empirical constant, and no other free parameters, will allow us to obtain nearly perfect quantitative agreement between the theory and simulations. Fig. 3.7 shows the dispersion calculated by the coupled mode theory using the empirical κ and the FDTD simulations for varying widths. Although there is very good agreement, we note that the dispersion calculated by the coupled mode theory is not very sensitive to small changes in κ . However, the propagation loss is exponentially dependent on κ and is a good measure of how well the coupled mode theory agrees with the FDTD simulations.

In order to compare the propagation loss, we start with a Q calculated

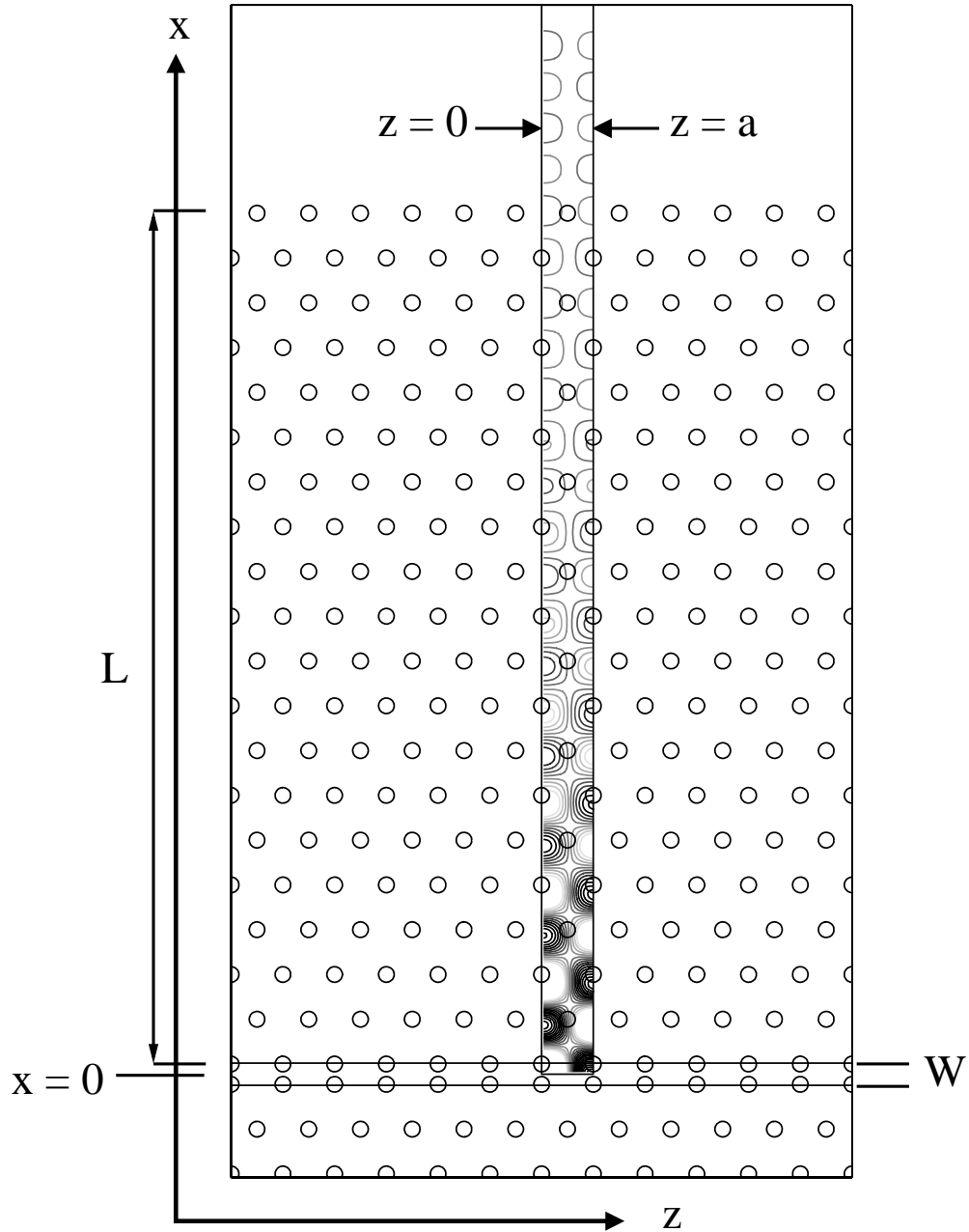


Figure 3.5: The 2D FDTD simulation domain showing a sample field calculation

by the FDTD simulation defined as

$$Q \equiv \omega \frac{\epsilon_0}{-\Delta P} , \quad (3.66)$$

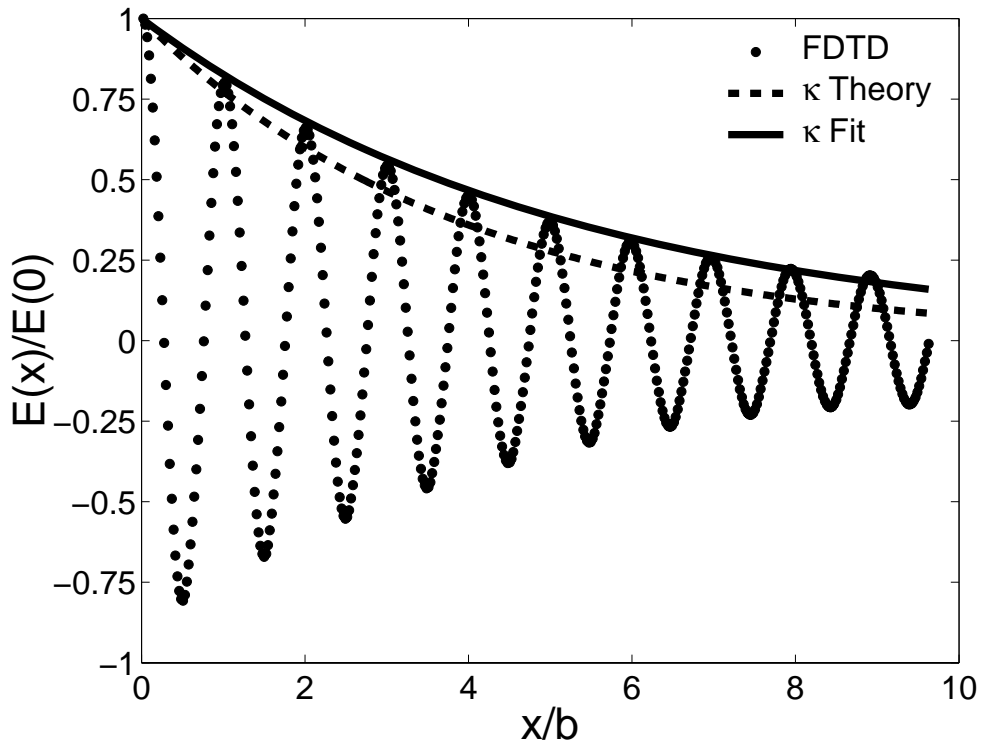


Figure 3.6: Normalized transverse field decay calculated by the 2D FDTD simulation for a structure with approximately 10 layers of Bragg periods

where \mathcal{E}_0 represents the stored energy and $\Delta P = \Delta\mathcal{E}/\Delta t$ is the power dissipation. If we assume low loss and intensity decay to have the form $|E(z)|^2 \sim \exp(-\alpha z)|E(0)|^2$,

$$\alpha = -2\beta_I = \frac{-\Delta\mathcal{E}}{\mathcal{E}_0} \frac{1}{L} = \frac{\omega}{Q} \frac{\Delta t}{L} = \frac{\omega}{Qv_g}, \quad (3.67)$$

where we choose $L/\Delta t \equiv v_g = (d\beta/d\omega)^{-1}$. From Fig. 3.7, we see that the dispersion curves are qualitatively the same, meaning that the slope of the curve does not change appreciably as the width of the core varies. Thus, we estimate the group velocity for all waveguides using an analytic expression

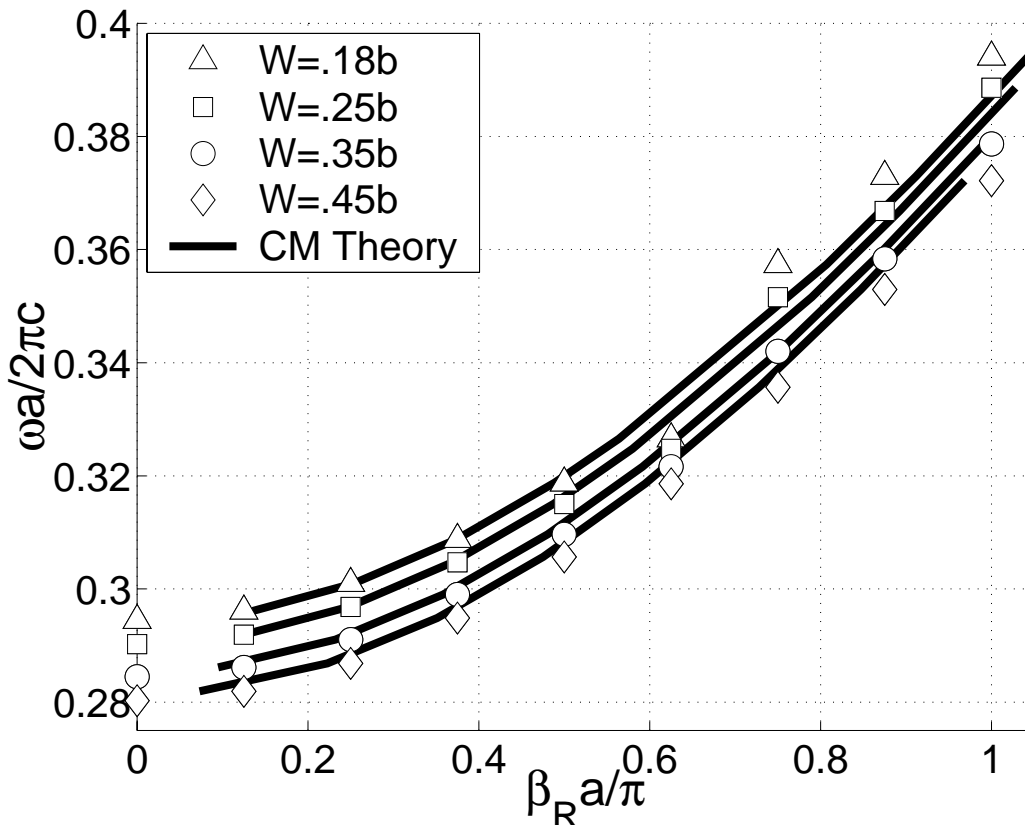


Figure 3.7: Dispersion curves for varying widths of the core

for the dispersion when the core width is $b/4$ [33],

$$v_g \approx \left(\frac{d}{d\omega} \sqrt{\bar{n}^2 \omega^2 - k_b^2} \right)^{-1} = \frac{\beta}{\epsilon \omega} = \frac{\beta}{\bar{n}} (\beta^2 + k_b^2)^{-1/2} \quad (3.68)$$

In Fig. 3.8, we plot the normalized loss constant, αa , from the 2D FDTD simulations using Eq. (3.67) for varying core widths with the normalized propagation constant, $\beta_R a$, as a parameter. As predicted[33], the case $W = b/4$ has the least propagation loss for the lowest order even guided mode studied, and we see that the reduction in loss compared to a larger width can be more than an order of magnitude. In Fig. 3.9, the comparison of the FDTD simulations to the coupled mode theory shows that the single

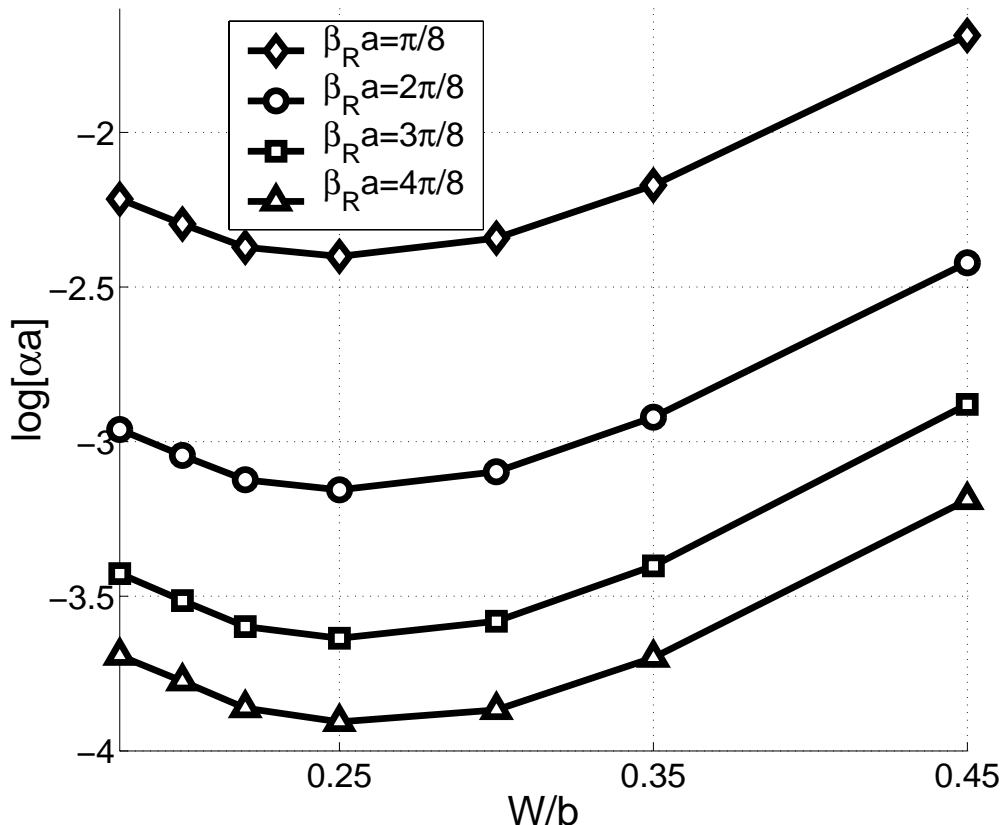


Figure 3.8: Plot of normalized loss constant, αa , from 2D FDTD simulations for varying core widths with the propagation constant, β_R , as a parameter

empirical constant chosen from Fig. 3.6 is capable of fitting the data for all width parameters when $\beta_R a / \pi < 0.6$. The large deviation from the theory near the points when $5/8 \leq \beta_R a / \pi \leq 6/8$ is a result of the one-dimensional nature of the coupled mode analysis. By constructing the reciprocal lattice[2] for the two dimensional triangular lattice used for the cladding, as shown in Fig. 3.10, we see that there is a point when the forward propagating mode, k_1 , can be coupled to the backward propagating mode, k_3 , by the lattice vector a_2 in addition to the transverse reflection, k_2 , via a_1 . This point results when $\beta_R a / \pi = 2/3$ which corresponds to the points that show deviation from the loss expected. Since the coupled mode treatment was 1-dimensional in nature

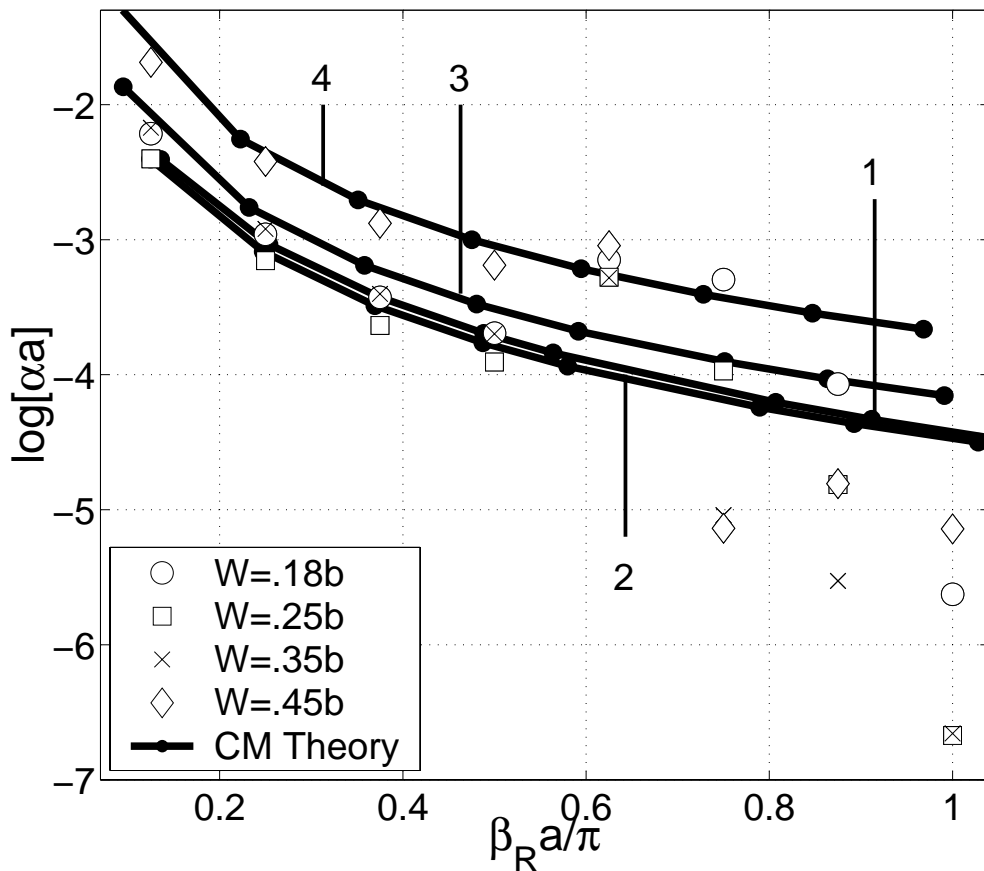


Figure 3.9: Plot of normalized loss constant from 2D FDTD simulations as well as coupled mode (CM) theory for selected core width values

and we only consider the lowest order Bragg reflection, it is not surprising that a k -vector smaller than k_1 shown in Fig. 3.10 is required in order to neglect the 2-dimensional periodicity of the triangular lattice cladding and obtain agreement between the analytical coupled mode theory and the numerical FDTD simulations.

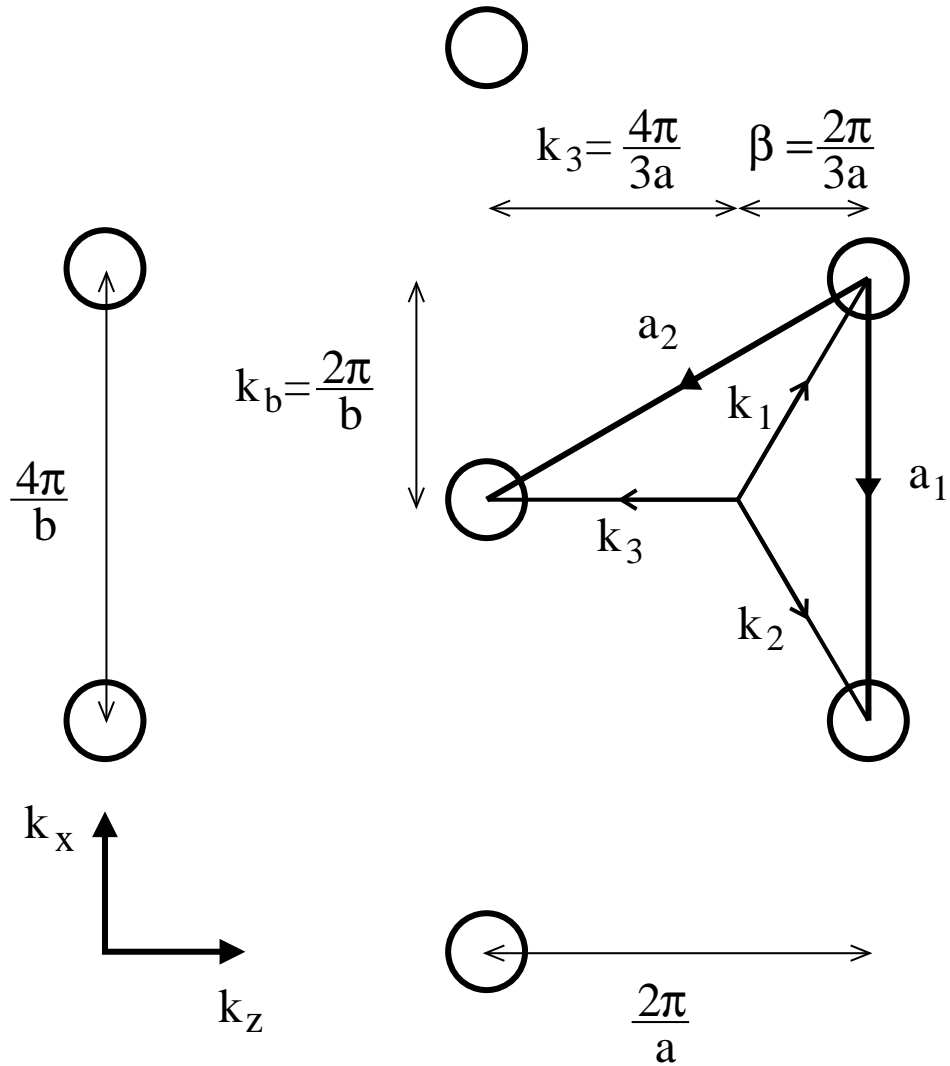


Figure 3.10: The reciprocal lattice vectors for the triangular lattice, $a_1 = -4\pi/b \hat{x}$ and $a_2 = -2\pi/b \hat{x} - 2\pi/a \hat{z}$

Chapter 4

Device Design, Fabrication, and Measurement

4.1 Design

4.1.1 Grating Pitch

The main design consideration for the device design is the grating pitch. Since the longitudinal feedback is provided by the facet reflection, there are many resonant Fabry-Perot modes allowed within the gain spectrum for any grating choice. In the plane-wave perspective, the TBR modes are propagating at much more glancing angles of incidence upon the facets. Thus, it is a reasonable criteria to consider the output of the refracted light.

The Bragg condition occurs when the transverse wavevector, k , equals the lattice wavevector, K , where $k = k_0 \sin \theta$, $k_0 = 2\pi n/\lambda$, $K = \pi/\Lambda$, Λ is the grating pitch, λ is the wavelength of light, n is the index of the material (or more generally the effective index of a mode), and θ is the angle of incidence shown in Fig. 4.1. This leads to the familiar equation for Bragg resonance,

$$\Lambda = \frac{\lambda}{2n \sin \theta} . \tag{4.1}$$

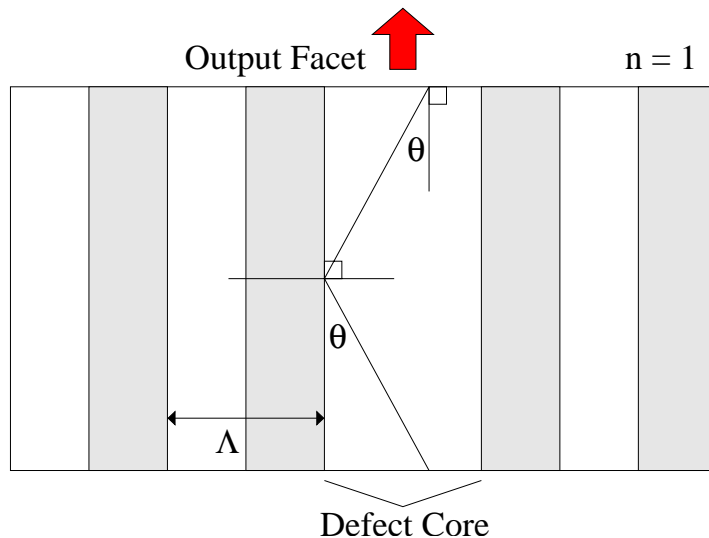


Figure 4.1: Schematic showing equivalent ray optics path within TBR waveguide

Since the angle of incidence can be far from normal, $\theta \neq 0$, the TBR grating can be designed with a pitch that is much larger than a typical DFB grating, resulting in much easier fabrication requirements. Although the transverse confinement is provided by Bragg reflection from the grating, the longitudinal feedback is still provided by the facet reflections, and in order to obtain output, the angle of incidence must not exceed the critical angle, $\theta < \theta_{cr}$, given by $\sin \theta_{cr} = 1/n$. Combining this with Eq. 4.1, the design rule we get is

$$\Lambda > \frac{\lambda}{2}, \quad (4.2)$$

which is independent of the material or effective index. In our design, we choose $\Lambda \approx \lambda$, $1.5 \mu\text{m}$, which includes a factor of 2 margin. This assures that all the wavelengths within the gain spectrum of the quantum well luminescence have the potential to produce laser output.

We may also state Eq. 4.2 in terms of β . For a simple plane-wave ap-

proximation, the dispersion is given by

$$n^2 \frac{\omega^2}{c^2} = k_x^2 + \beta^2 . \quad (4.3)$$

At the facet interface, the boundary conditions imposed require the transverse wavevectors to be continuous. Therefore, at the critical angle when total internal reflection occurs, $k_x = \omega/c$, and if the Bragg condition is satisfied, we also know

$$k_x = \frac{\pi}{\Lambda} . \quad (4.4)$$

Thus,

$$\beta_{cr} = \sqrt{n^2 - 1} \frac{\omega}{c} = \sqrt{n^2 - 1} \frac{\pi}{\Lambda} \quad (4.5)$$

at the critical angle. Also, from Eq. 4.3, it is clear $\beta \leq n\omega/c$, so

$$\sqrt{n^2 - 1} \frac{\omega}{c} \leq \beta \leq n \frac{\omega}{c} . \quad (4.6)$$

From Eq. 4.1, we can rewrite Eq. 4.6 in terms of the grating pitch as

$$\left(\sqrt{n^2 - 1} \right) \frac{\pi}{\Lambda} \leq \beta \leq \left(\frac{1}{\sin \theta} \right) \frac{\pi}{\Lambda} . \quad (4.7)$$

This expression is useful when solving numerically for the modes of a structure.

4.1.2 Wafer Epitaxy/Surface Grating

Using the knowledge gained from these analytical and numerical models, an epitaxial wafer structure was designed. The main design considerations were electrically pumped lasing and surface grating interaction with the TBR confined optical mode. The surface grating approach was chosen to avoid the regrowth process, resulting in a simpler, and hence less costly, design. This

Layer	Description	Material	PL (nm)	Thickness (Å)	Index	Doping
0	Substrate	InP	900		3.1720	n
1	Buffer	InP	900	10000	3.1720	n+ 1E18
2	Waveguide	InGaAsP	1100	700	3.2911	n 1E17
3	Waveguide	InGaAsP	1100	300	3.3203	undoped
4	Waveguide	InGaAsP	1250	500	3.3755	undoped
5	QW	InGaAsP	1600	85	3.5300	undoped
6	Barrier	InGaAsP	1250	100	3.3755	undoped
7	QW	InGaAsP	1600	85	3.5300	undoped
8	Barrier	InGaAsP	1250	100	3.3755	undoped
9	QW	InGaAsP	1600	85	3.5300	undoped
10	Barrier	InGaAsP	1250	100	3.3755	undoped
11	QW	InGaAsP	1600	85	3.5300	undoped
12	Waveguide	InGaAsP	1250	500	3.3755	undoped
13	Waveguide	InGaAsP	1200	400	3.3484	undoped
14	Etch Stop	InGaAsP	1200	1300	3.3484	p 1E17
15	Cladding	InP	900	4000	3.1720	p 1E17 to 2E18
16	Etch Mask	InGaAs	1650	50	3.5500	p+ 1E19

Table 4.1: Epitaxial wafer structure

criteria for electrical pumping and surface grating interaction with the mode led to some challenges compared to conventional laser structures. The interaction between the surface TBR grating and the optical mode required the top, p-type contacts to be much closer than in most semiconductor laser designs. However, due to the metal contacts, this can result in higher loss, preventing lasing at practical pumping currents. With these competing considerations in mind, the wafer was designed as shown in Table 4.1[1, 18]. A

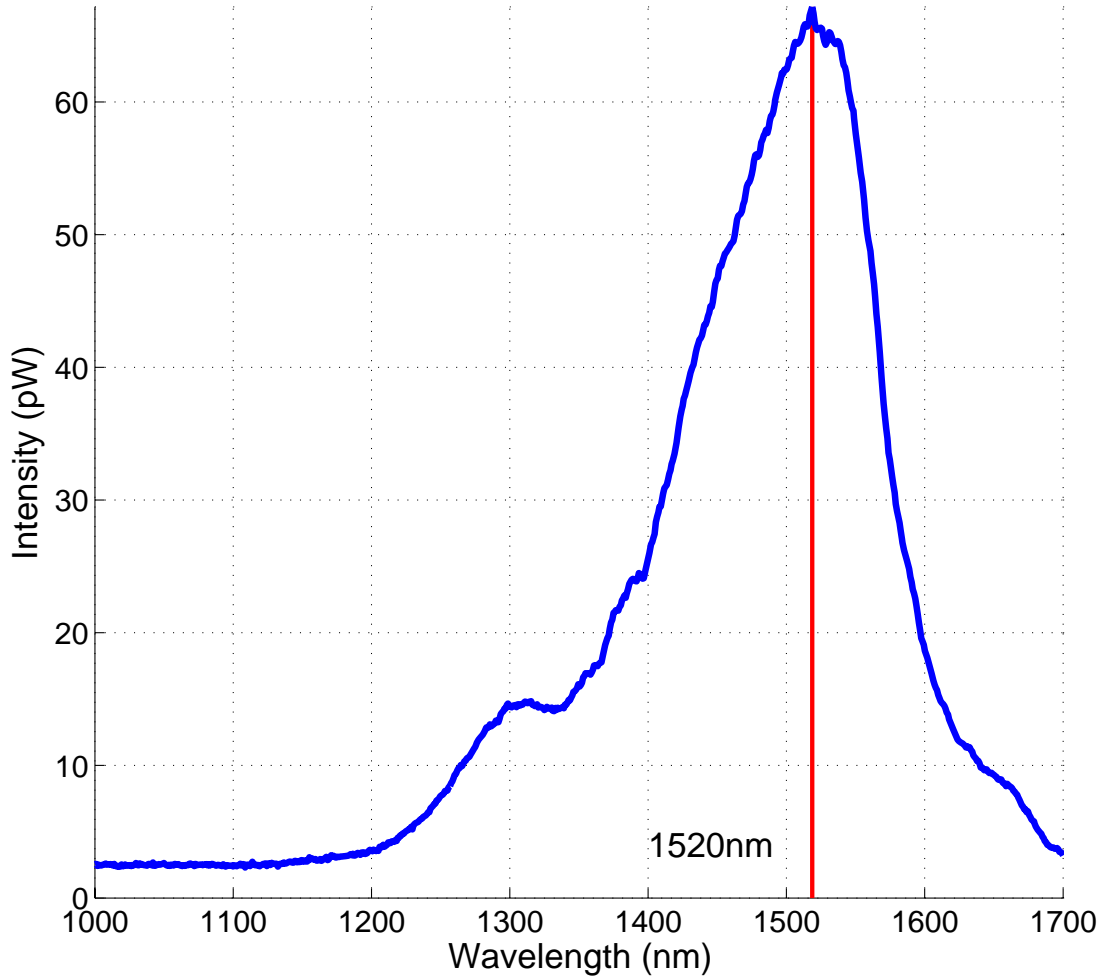


Figure 4.2: Photoluminescence of unprocessed wafer of Table 4.1 excited by a Ti:sapphire pulsed source

sample photoluminescence spectrum of the unprocessed wafer is shown in Fig. 4.2.

To design the surface grating, we need to estimate the coupling constant, κ , for a given etch depth. First, let's calculate the Fourier components of a square grating.

$$\epsilon(x) = \sum_{n=-\infty}^{+\infty} \epsilon_n e^{in2kx} , \quad (4.8)$$

where $k = \pi/\Lambda$, the fundamental lattice vector, and the factor of 2 is due to the round-trip phase condition, and

$$\epsilon_n = \frac{1}{\Lambda} \int_{-\Lambda/2}^{\Lambda/2} \epsilon(x) e^{-in2kx} dx = \frac{\Delta\epsilon}{\Lambda} \int_{-\Lambda/4}^{\Lambda/4} e^{-in2kx} dx = \frac{\Delta\epsilon}{n\pi} (-1)^{\frac{1}{2}(n-1)}, \quad (4.9)$$

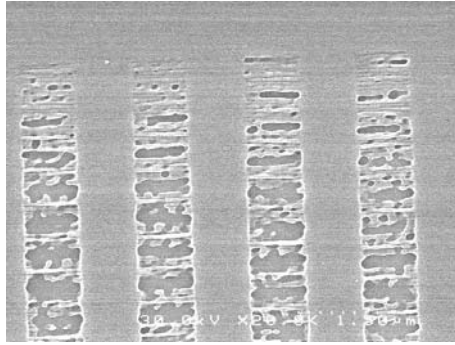
where $n = 1, 3, 5 \dots$ is odd.

$$\kappa \approx \frac{k_0^2}{2k_b} \frac{\int_{-\infty}^{+\infty} \int_{-\Lambda/2}^{+\Lambda/2} \Delta\epsilon(x, y) |E(y)|^2 dx dy}{\int_{-\infty}^{+\infty} |E(y)|^2 dy} \approx \frac{k_0^2}{2k_b\pi} \frac{\int_{-\infty}^{+\infty} \Delta\epsilon(y) |E(y)|^2 dy}{\int_{-\infty}^{+\infty} |E(y)|^2 dy}, \quad (4.10)$$

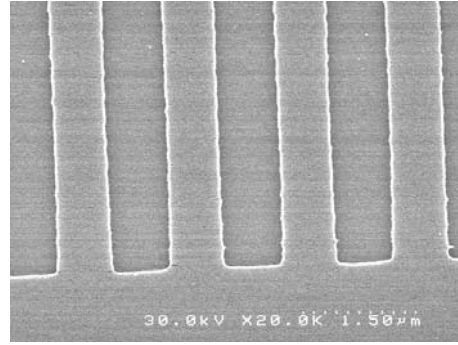
where we have approximated $E(y)$ as the eigenmode of a structure with the average index, $\bar{\epsilon}(x, y)$ and $\Delta\epsilon(x, y) = n_{hi}^2 - n_{lo}^2$ in the etched region and zero elsewhere. Using this method, $\kappa \approx 0.0612/\text{period}$.

4.2 Fabrication

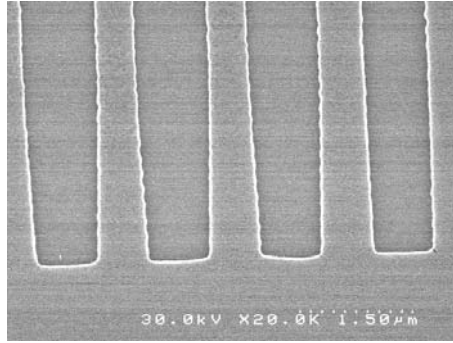
After procuring the commercially grown InP/InGaAsP/InGaAs multiple quantum well wafer material described in the previous section, the fabrication can be roughly divided into lithography, etching, metallization, and packaging. For a Bragg grating, we must define a set of periodic lines with a pitch as guided by Eq. 4.2. By choosing a period of $1.5\mu m$, and a first order grating, our lithography must be capable of defining lines that are half the period, 750nm. Lithography was provided by an electron beam system due to its flexibility for design changes and higher resolution capability under $1\mu m$, as compared to conventional contact, UV photolithography[24]. Lithography and etching were done at the Stanford Nanofabrication Facility (SNF). The resist used was 2% 495K MW PMMA (polymethyl methacrylate) in anisole, spun on a Headway manual coater at 2000 RPM for 45s resulting in an approximately 300nm film. After this, the sample was baked on a hot plate at



(a) Under-exposed.



(b) Optimally exposed.



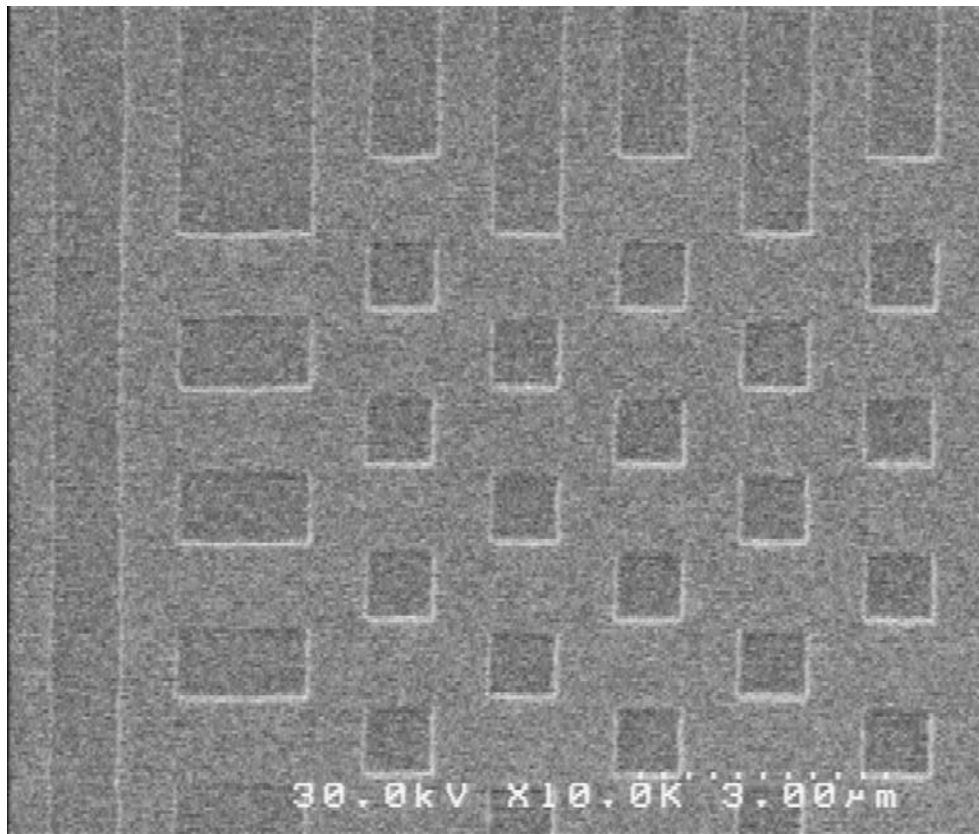
(c) Over-exposed.

Figure 4.3: Electron microscope images of developed PMMA that is (a) underexposed, (b) optimally exposed, and (c) overexposed

200°C for 2 minutes. The system used was a Hitachi HL-700F direct write patterning tool, with a 30keV beam, 4nA current, and a 40 μm minor field size for deflection based stitching, and a 2mm major field size for mechanical stitching. The correct dosage was found to be around 275 $\mu\text{C}/\text{cm}^2$. This dosage was found by writing the same pattern multiple times at different dosages and examination under a scanning electron microscope after development. Fig. 4.3 shows some sample patterns that are under-exposed (Fig. 4.3(a)), optimally exposed (Fig. 4.3(b)), and over-exposed (Fig. 4.3(c)). Fig.

Step	Description
1	Cleave wafer into pieces.
2	Ultrasonic clean in acetone 3 minutes.
3	Ultrasonic clean in propanol 3 minutes.
4	Ultrasonic clean in methanol 3 minutes.
5	Bake on hotplate 200°C 5 minutes.
6	Spin 2% 495K MW PMMA in anisole 2000 RPM 45 seconds.
7	Bake on hotplate 200°C 2 minutes.

Table 4.2: Electron beam resist coat procedures

Figure 4.4: 500nm squares etched into InP using a HBr:HNO₃ mixture

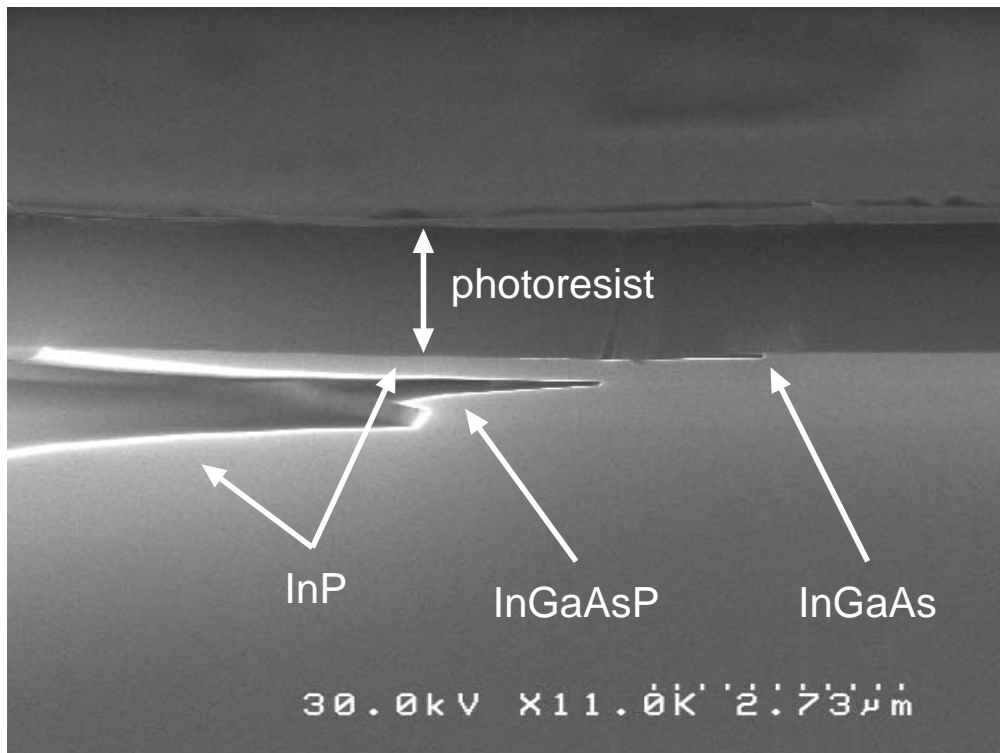


Figure 4.5: Electron microscope image of etched profile using a $\text{HBr}:\text{HNO}_3$ mixture showing the etch rates for different InGaAsP alloys

Step	Solution (Volume Ratios)	Time	Description
1	MIBK:IPA (1:3)	60 seconds	PMMA Develop
2	IPA	30 seconds	Rinse

Table 4.3: PMMA develop procedure

4.3(a) shows incomplete development and residual resist inside the patterned areas. Fig. 4.3(c) shows a bowing of the edges compared to Fig. 4.3(b), resulting in a wider exposed area near the top of the image as compared to the edges of the area at the bottom of the image. (This is due to the proximity effect.) After exposure, the samples were developed in a mixture of MIBK:IPA (methyl isobutyl ketone:isopropanol) 1:3 for 60 seconds followed by a rinse in

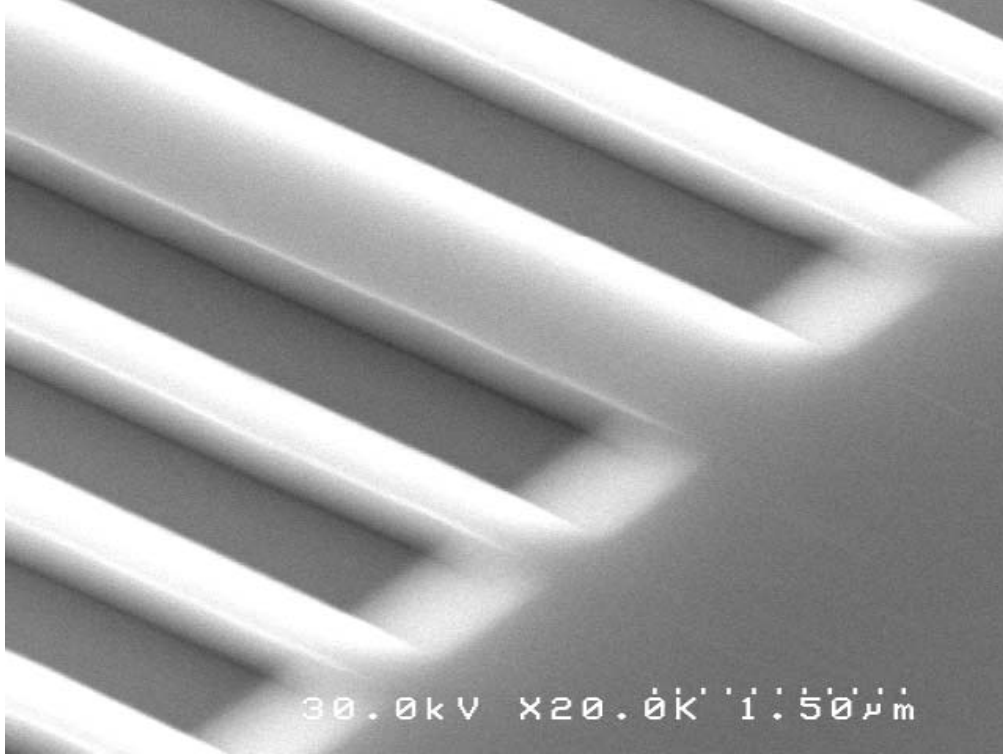


Figure 4.6: Surface gratings after HCl:H₂O etch into InP mixture

IPA for 30 seconds. Following the lithography and development (Fig. 4.7(a)-

Step	Etch Solution (Volume Ratios)	Time	Description
1	HBr:HNO ₃ :H ₂ O (1:1:30)	5 seconds	InGaAs Etch
2	H ₂ O	15 seconds	Rinse
3	H ₂ O	15 seconds	Rinse
4	HCl:H ₂ O (4:1)	30 seconds	InP Etch
5	H ₂ O	15 seconds	Rinse
6	H ₂ O	15 seconds	Rinse

Table 4.4: Etch procedure

4.7(c), the PMMA mask was used to directly transfer the grating pattern into

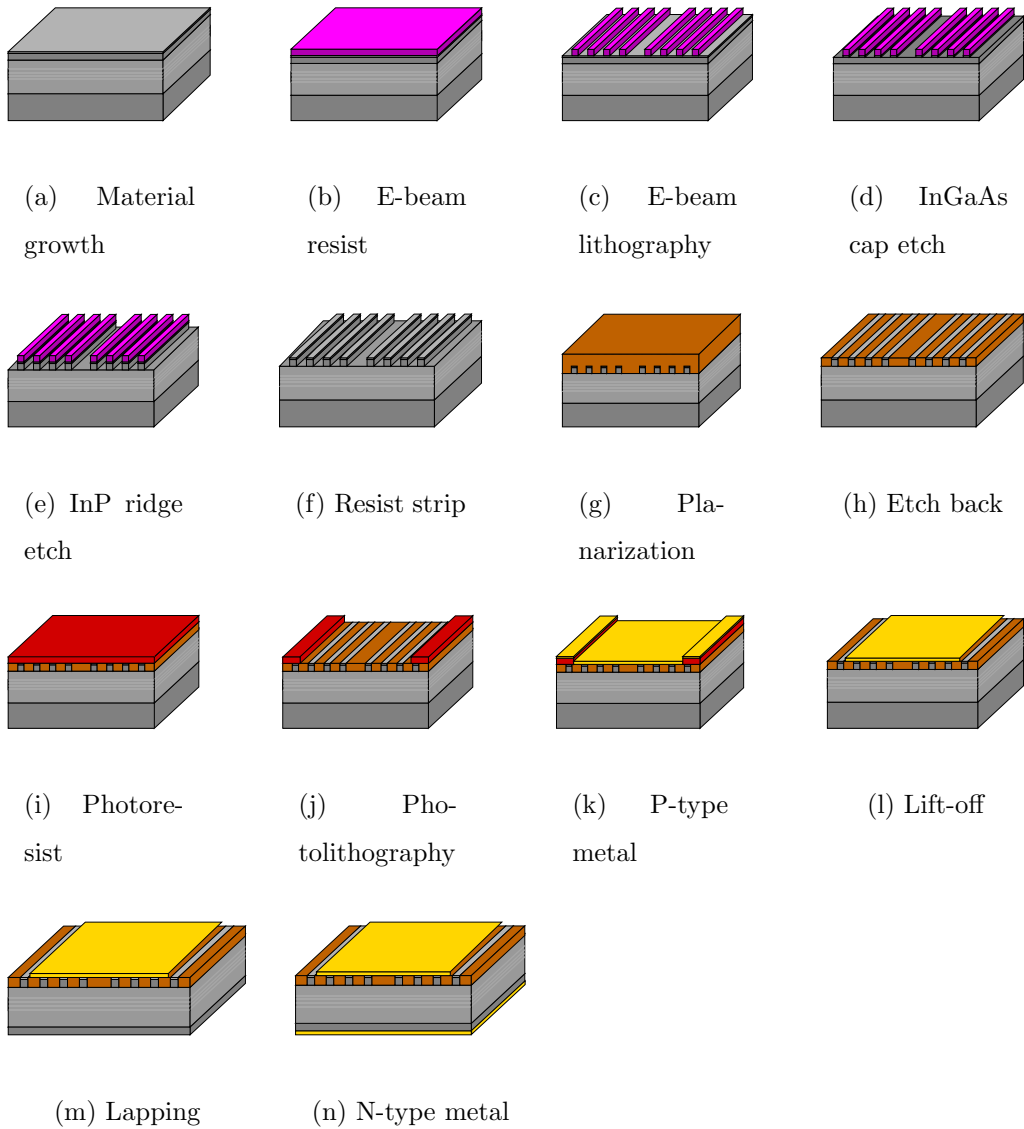


Figure 4.7: Process flow

the semiconductor. The technique used involves a two-step wet etch and an epitaxial mask [14]. In the first step (Fig. 4.7(d)), a 50nm InGaAs epitaxial mask layer was etched with a 1 HBr:1 HNO₃:30 H₂O mixture. (Actual percentage: Hydrobromic Acid 1.5%:Nitric Acid 2.2%:Water 96.3%) This etch is capable of transferring very high resolution features (for a wet etch), and features as small as 500nm have been successfully etched at SNF (Fig. 4.4). Although it etches both InP and InGaAs(P), the etch rate of InP is much slower, as can be seen in Fig. 4.5. The grating was then transferred into the InP device using a chemically selective etch of 4 HCl:1 H₂O (Fig. 4.7(e)) and the PMMA mask was then stripped (Fig. 4.7(f)) by soaking in acetone. The etch procedures used are shown in Table 4.4. A planarization layer of

Step	Description
1	Clean pieces in solvents.
2	Bake on hotplate 180°C 5 minutes.
3	Spin AP3000 adhesion promoter 5000 RPM 45 seconds.
4	Spin BCB3022-63:T1100 2:1 5000 RPM 45 seconds.
5	Bake on hotplate 80°C 90 seconds.
6	Place in oven with nitrogen atmosphere.
7	Ramp up to 25°C (15 minutes).
8	Ramp up to 150°C (30 minutes) and hold for 15 minutes.
9	Ramp up to 250°C (15 minutes) and hold for 1 hour.
10	Ramp down to 25°C (1 hour) and cool.

Table 4.5: BCB planarization coat procedure

BCB (cyclotene-3022-63:t1100 benzocyclobutene:trimethylbenzene 2:1) was then spun on at 6000 RPM and baked at 250°C for 2 hours (Fig. 4.7(g)). This resulted in an approximately 2.2 μ m thick film. This layer was then

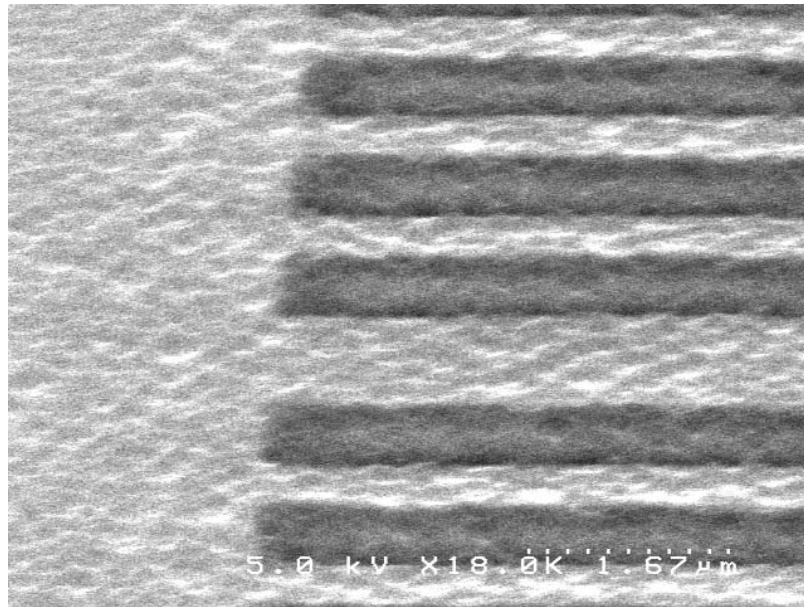
Step	Description
1	Clean pieces in solvents.
2	Bake on hotplate 195°C 5 minutes.
3	Spin LOR10B 5000 RPM 45 seconds. (1 μ m film)
4	Bake on hotplate 195°C 6 minutes.
5	Spin SPR-3612 5000 RPM 45 seconds. (1.6 μ m film)
6	Bake on hotplate 90°C 90 seconds.
7	Expose on Karl Suss MA-6 2.5 seconds. (365nm, 15mW/cm ²)
8	Develop in LDD-26W 60 seconds.
9	Rinse in H ₂ O 15 seconds.

Table 4.6: Photolithography procedure

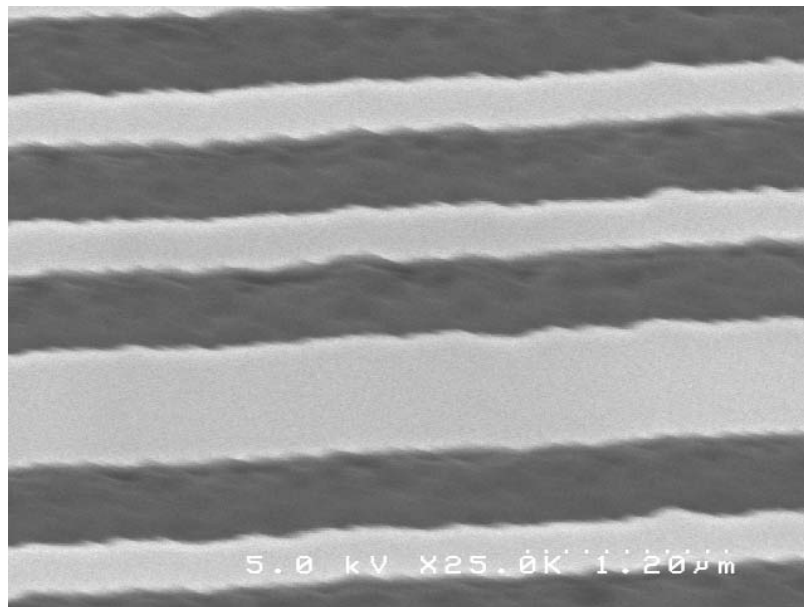
etched back in an O₂:CF₄ plasma (Fig. 4.7(h)). The etcher was a Plasma Quest electron-cyclotron resonance (ECR) plasma etcher. The chamber was first cleaned with an O₂ plasma at 5mT pressures, 100sccm flow, 700W microwave power, and 100W RF power for 10 minutes. After a 2 minute argon purge, the chamber was pre-conditioned using the actual etch recipe for 15 minutes. The samples were then mounted on the center of a 4-inch silicon carrier wafer with double-sided copper tape (3M 1182), such that no tape was exposed, and loaded into the chamber. The etch conditions were 80sccm O₂, 20sccm CF₄, 400W microwave power, 20W RF power (typical bias 40V) at a chamber pressure of 10mT. The sample chuck was set to 20°C and the carrier wafer was cooled with a helium backflow pressure of 10T. The resulting etch rate was approximately 200Å/min.

After planarization, photolithography (Fig. 4.7(i), 4.7(j)) was used to isolate neighboring devices, and p-side metal contacts were deposited with an electron-beam evaporator, Ti:Pt:Au 20nm:50nm:500nm (Fig. 4.7(k)).

A final lift-off completed the p-side processing (Fig. 4.7(l)). Finished devices are shown in Fig. 4.11. These devices were then lapped to $100\mu\text{m}$ thin (Fig. 4.7(m)), and the n-side contact metallization was deposited with a thermal evaporator, Cr: AuGe: Au 5nm:25nm:100nm (Fig. 4.7(n)). No anneal step was performed. The devices were then cleaved into individual die and bonded to gold-plated copper c-mounts using a eutectic PbSn (37/63 183°C) solder paste (90.25% metal) (Indium Corporation SMQ92J). The samples were then wirebonded with 6-8 0.001" inch diameter 1% silicon/aluminum wire leads.

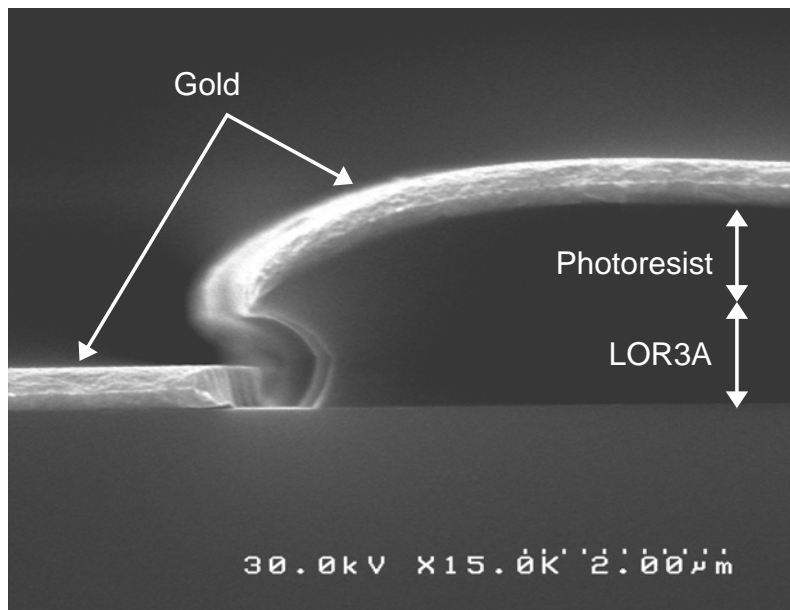


(a) Under-planarized.

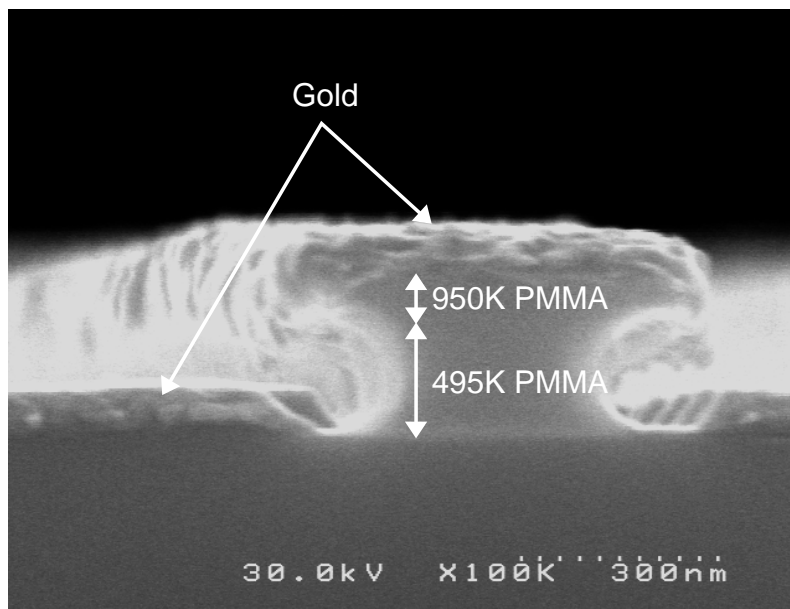


(b) Optimally planarized.

Figure 4.8: Electron microscope images of surface after etching of planarization polymer showing (a) incomplete planarization and (b) complete planarization



(a) Photolithography



(b) Electron beam lithography

Figure 4.9: Scanning electron microscope images of lift-off resist profiles for (a) photolithography and (b) electron beam lithography

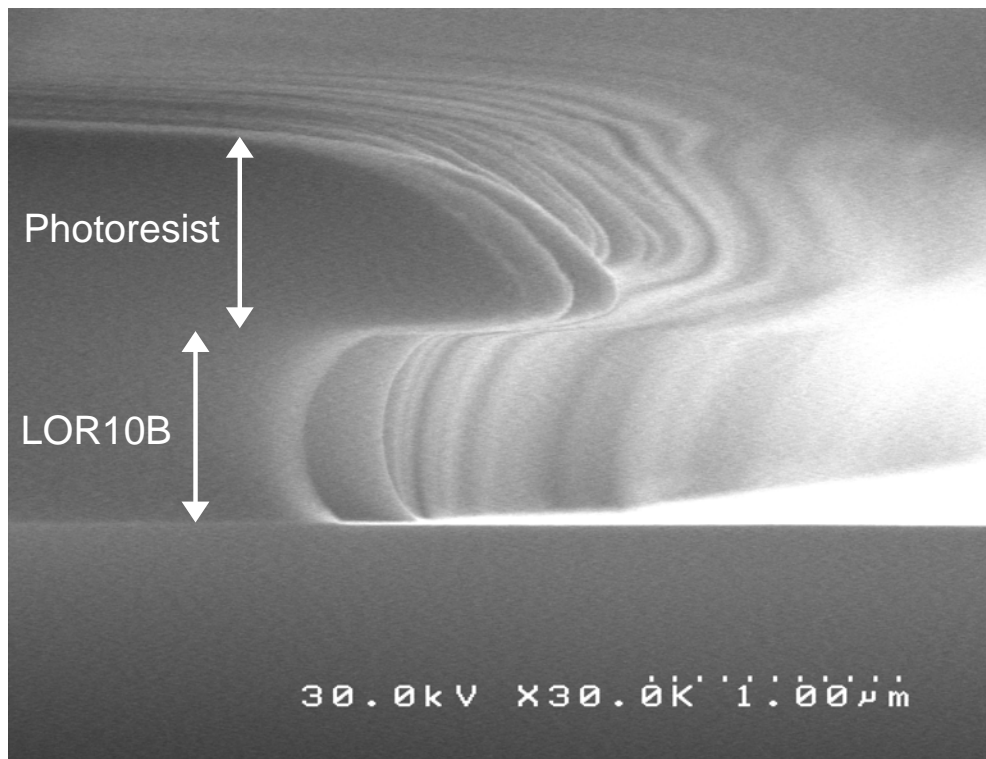
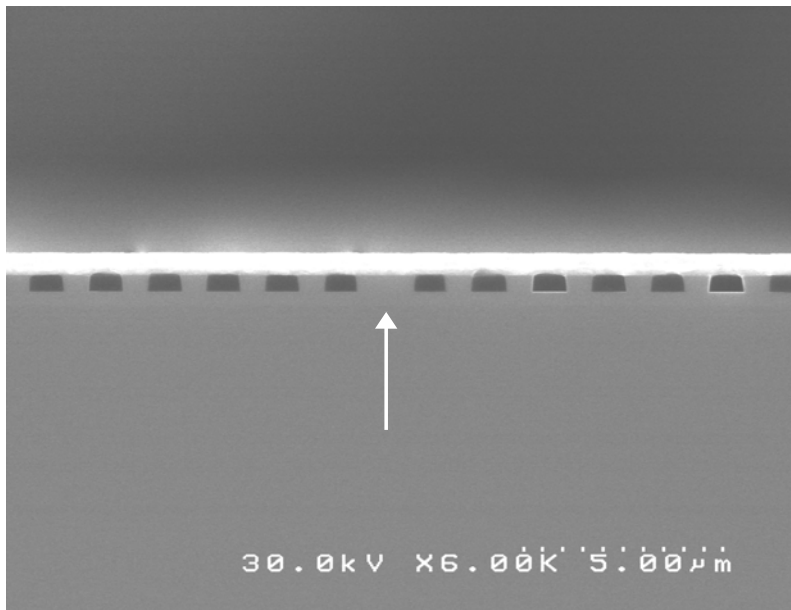
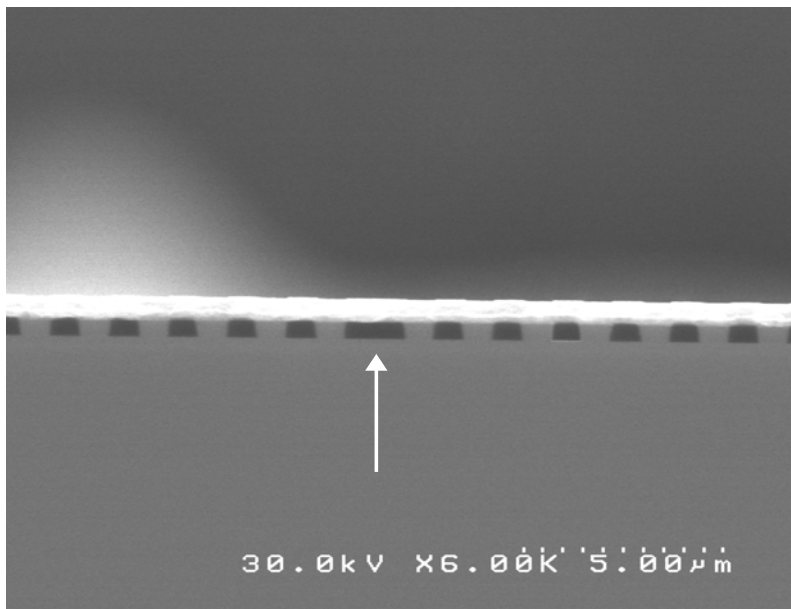


Figure 4.10: Scanning electron microscope image of developed LOR10B and photoresist showing undercut profile



(a) Under-planarized.



(b) Optimally planarized.

Figure 4.11: Scanning electron microscope images of TBR lasers showing the defect region. (a) A high index defect composed of semiconductor and (b) a low index defect composed of polymer

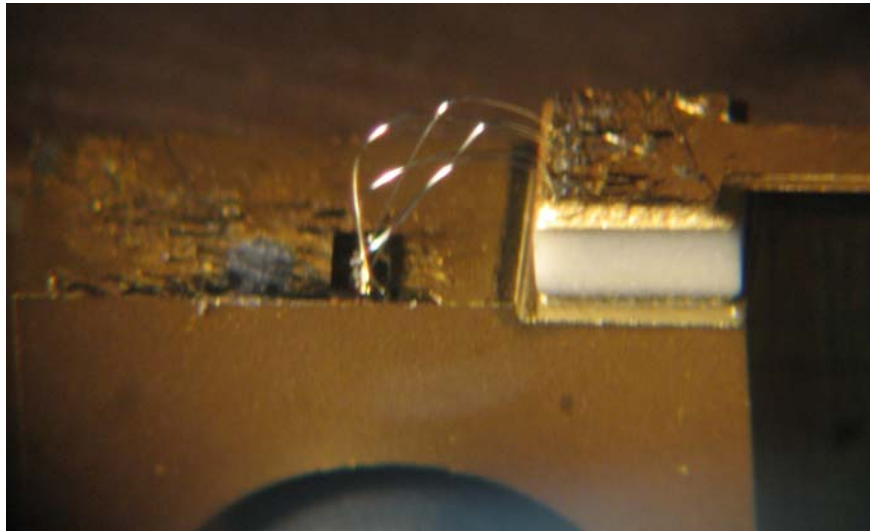


Figure 4.12: A fully fabricated device die-bonded onto a c-mount heatsink and wirebonded

4.3 Measurement

4.3.1 Experimental Setup

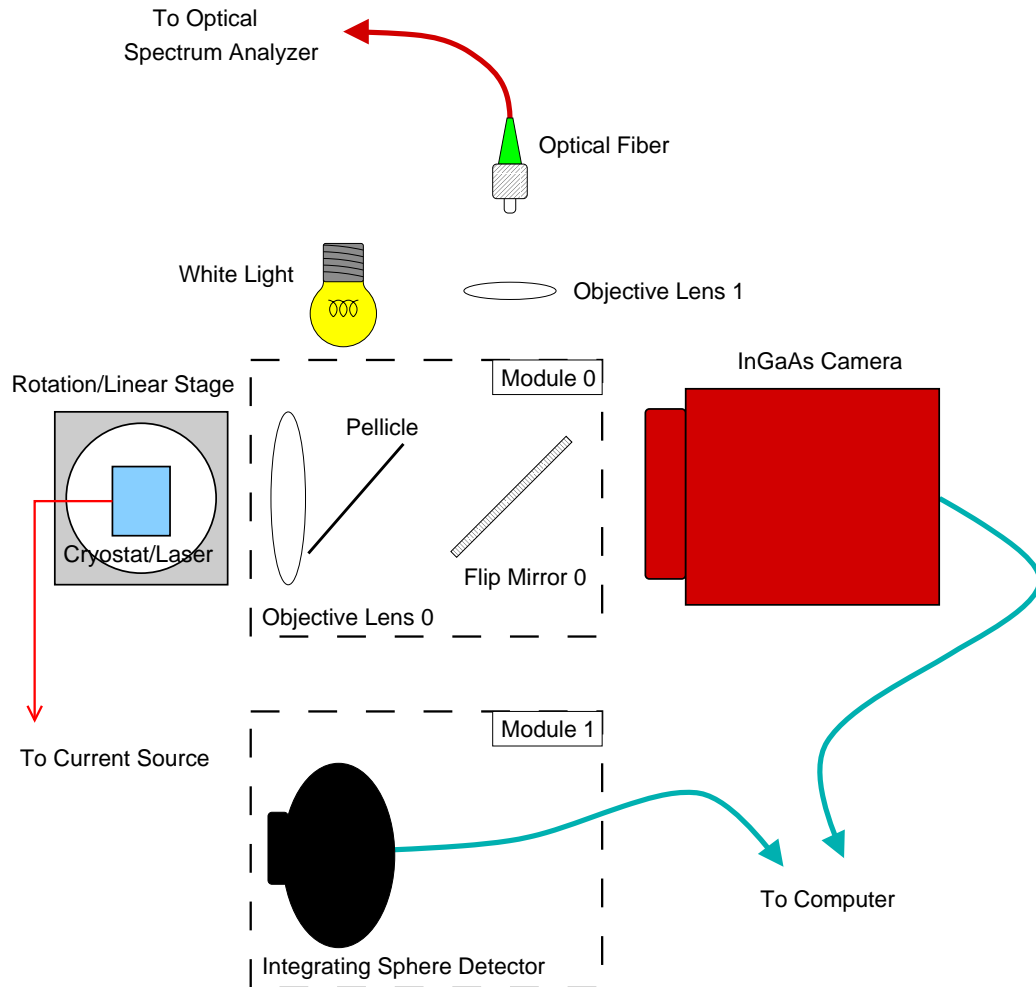


Figure 4.13: Experimental setup used for measurement of devices

The experimental setup used for measuring fabricated devices is shown in Fig. 4.13. The laser was placed in a cryostat (MMR Technologies Micro Miniature Refrigerator, Optical Transmission/Fused Silica Window, K-77 Controller) mounted to linear and rotation motion stages and connected to a constant current source (ILX Lightwave LDC-3742B). For measuring the

optical spectrum of the emission, Objective Lens 0 (Mitutoyo M Plan Apo NIR 50X) and Objective Lens 1 (20X 0.4 NA) were used to focus the light into a multimode optical fiber that was connected to an optical spectrum analyzer (HP 70950A). The path was folded by Flip Mirror 0. For nearfield imaging of the intensity as well as the facet, Flip Mirror 0 was removed from the path by folding down, resulting in an unobstructed path to the InGaAs area camera (Sensors Unlimited SU640SDV). The White Light and Pellicle were used for imaging the facet for alignment purposes. By replacing all elements demarcated as Module 0 with the Integrating Sphere Detector (ILX Lightwave OMM-6810B with OMH-6727B) designated as Module 1, the total integrated power was measured for a light vs. current density (L-I) curve. By removing all elements between the device under test and the camera, farfield data was taken by rotating the laser on the rotation stage (Newport URS150CC). The camera pixels were used in place of a slit, to effectively create a variable aperture in increments of the pixel spacing, $25\mu\text{m}$.

4.3.2 Pulsed and Continuous Lasing

The packaged samples were then tested under pulsed and continuous operation at cooled and cryogenic temperatures as shown in Fig. 4.14.

By cleaving individual lasers separately and bonding them to heat sinks (industry standard c-mounts), the thermal effects were mitigated. Previous results required 0.125% duty cycle to prevent heat induced failure (50ns pulse width, $40\mu\text{s}$ periods, HP 8114A Pulse Generator). However, using active cooling techniques (thermoelectric cooling) at a temperature of 10°C , lasing was observed at $1.5\mu\text{s}$ pulse widths (Fig. 4.15). This was an improvement of more than 100 times. As seen in Fig. 4.15, thermal roll-off occurred above a duty cycle of 15%, and continuous lasing could not be achieved.

For continuous wave operation, cryogenic temperatures were required.

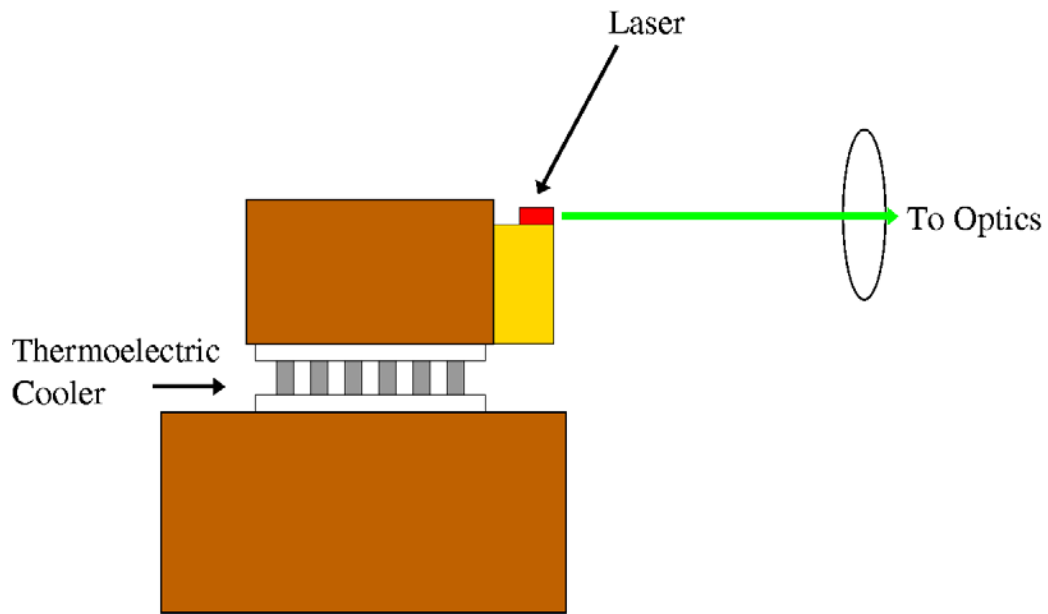
As the setpoint temperature of the cryostat was lowered, the optical gain increased due to the reduced rate of non-radiative, thermal transitions, as well as a blue-shift of the emission peak as shown in Fig. 4.16. Fig. 4.17 shows the L-I and I-V curves of continuous wave operation of lasers at a cryostat temperature of 82K and Fig. 4.18 shows the optical spectrum of the same devices. From the I-V curves of Fig. 4.17(b), it is clear that the TBR lasers have a higher turn-on voltage, on the order of twice, indicating larger contact resistance. This is also apparent from the spectral red-shift shown in Fig. 4.18(a), experienced by both TBR lasers while the broad-area laser shows negligible shift. This may be due to the surface of the TBR laser being half the area due to the 50% duty-cycle grating, increasing the resistance by a corresponding factor of 2.

4.3.3 Nearfield

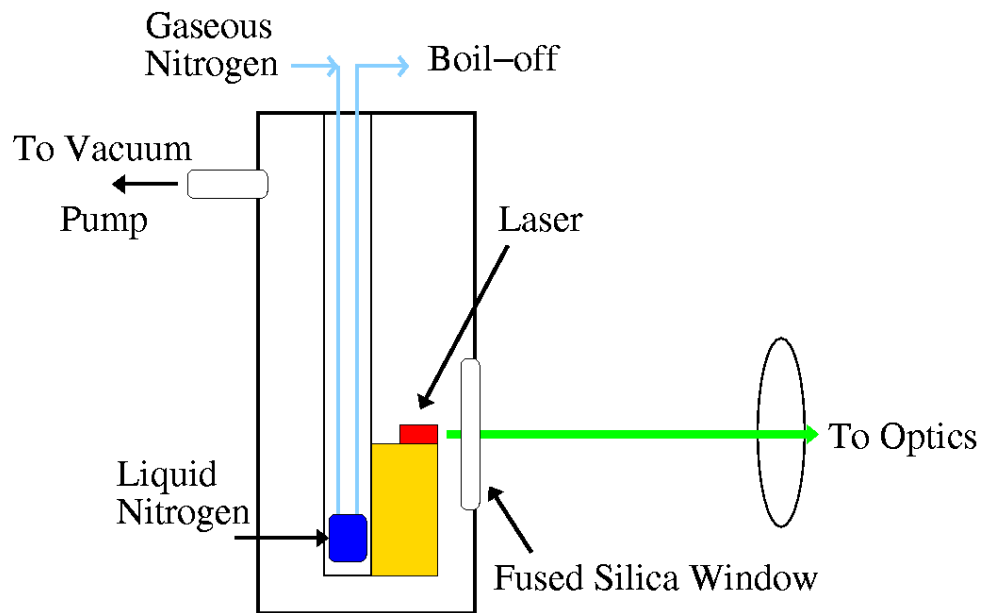
Figs. 4.19-4.21 show the nearfield intensity distribution of the measured devices below threshold (Fig. 4.19), near threshold (Fig. 4.20), and above threshold (Fig. 4.21) at the values shown in Fig. 4.18(a).

4.3.4 Farfield

Fig. 4.22 shows the farfield pattern for the lasers at a pump current of 90mA for each device. The aperture used was equivalent to a slit size of 8.9mm X 0.5mm which corresponds to an integration over approximately 0.6° for each data point. Data was measured at 1° intervals. Comparing the farfield patterns of the TBR lasers to the broad area laser, the TBR lasers seem to have a full width at half maximum (FWHM) almost twice as wide.



(a) Thermoelectric cooling



(b) Cryogenic cooling

Figure 4.14: Schematic diagram of apparatus for (a) thermoelectric cooling and (b) cryogenic cooling

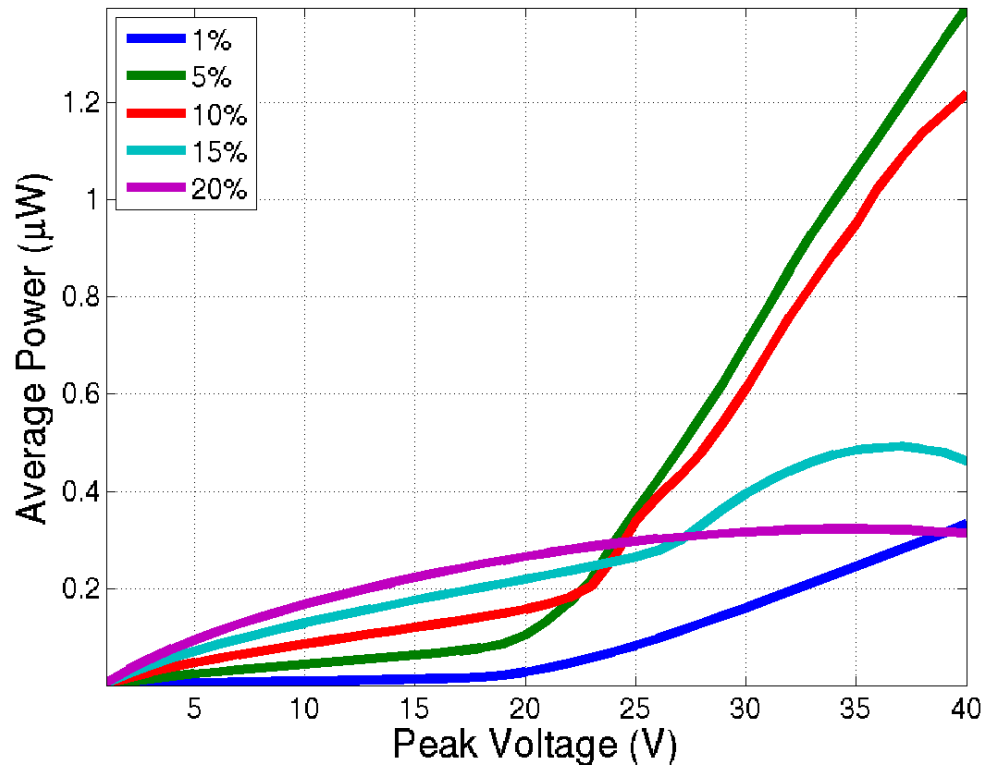


Figure 4.15: Average optical power vs. peak voltage of a TBR laser as a function of duty cycle for a $10\mu\text{s}$ period. Data is shown for 100ns to $2\mu\text{s}$ pulse widths at a heat sink temperature of 10°C .

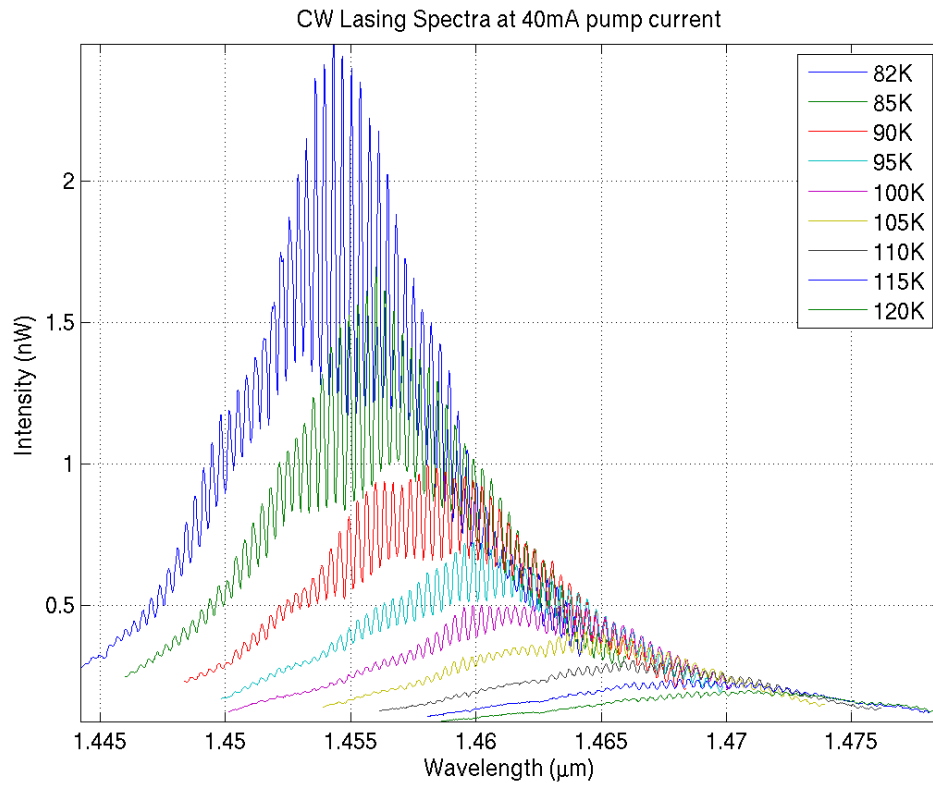
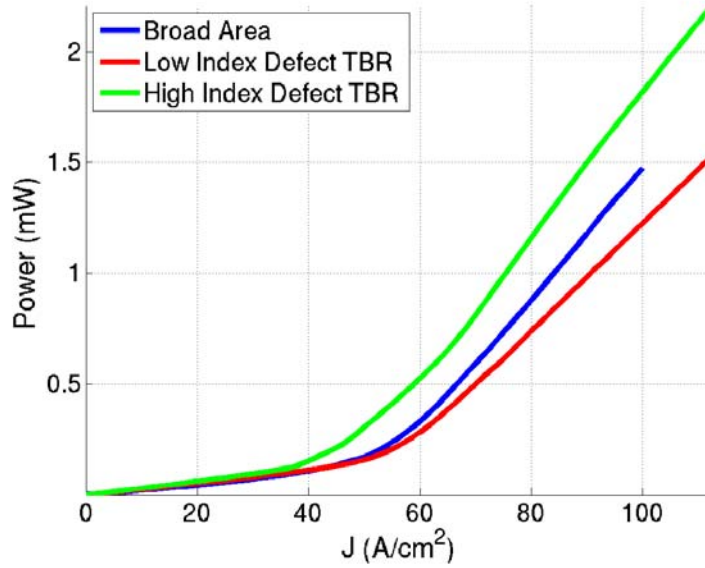
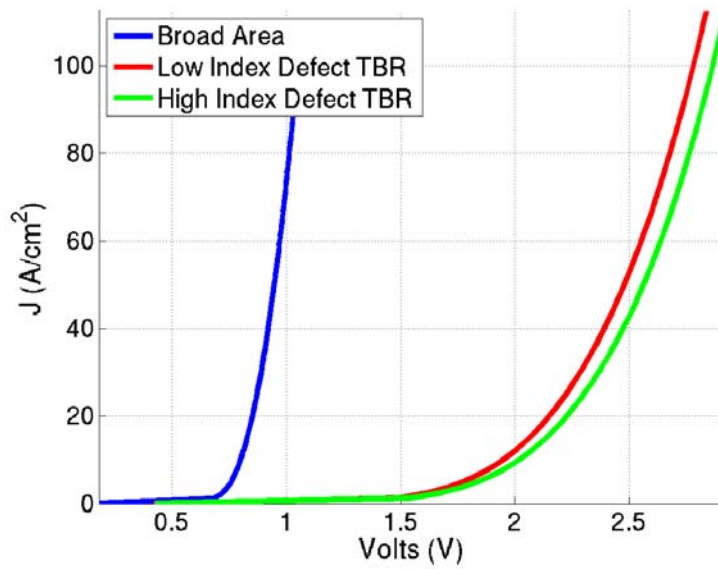


Figure 4.16: Lasing spectrum shift as a function of cryostat temperature

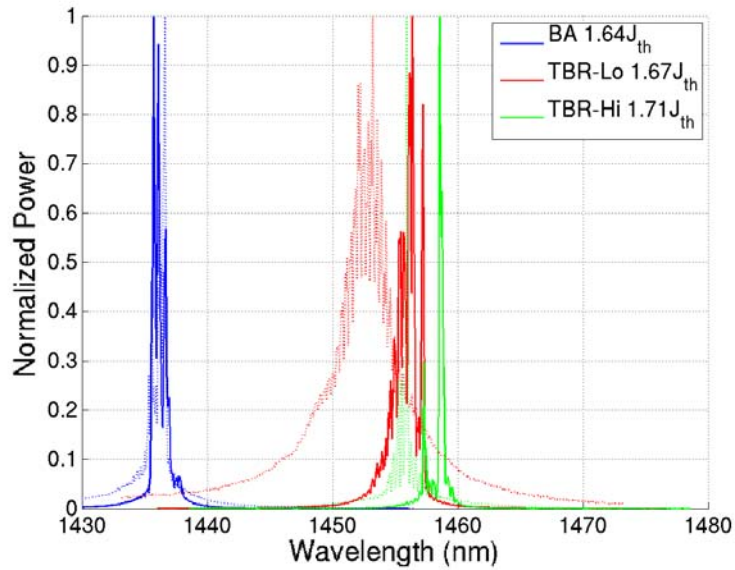


(a) L-I plot

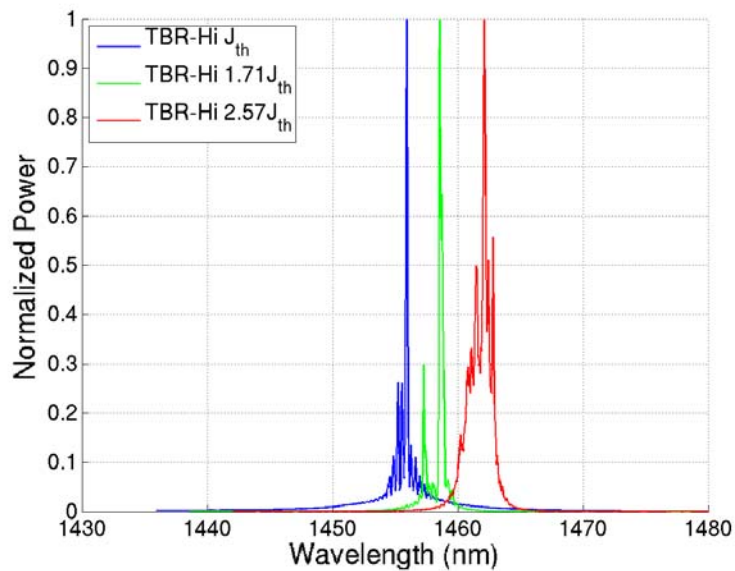


(b) I-V plot

Figure 4.17: (a) Continuous wave light vs. current density curves at cryostat temperature of 82K. (b) Current vs. voltage curves of corresponding lasers

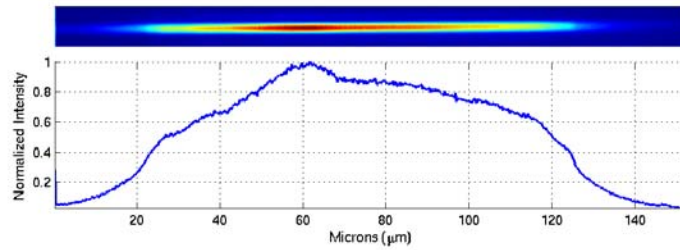


(a) Laser spectra

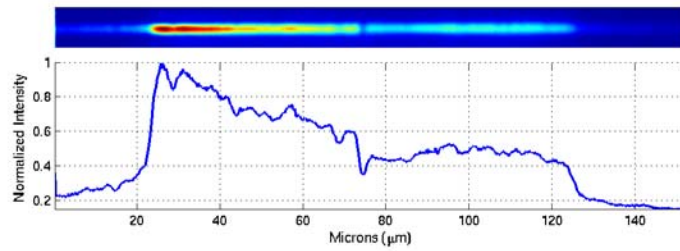


(b) TBR hi defect spectra

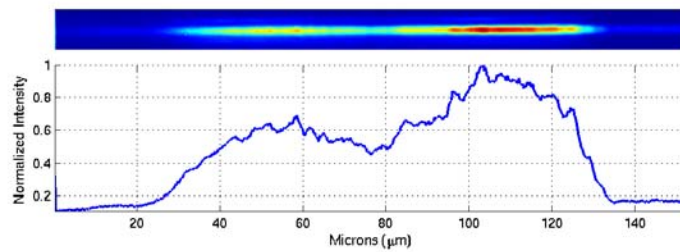
Figure 4.18: (a) Lasing spectra of a broad-area laser, a low index defect TBR, and a high index defect TBR. The dashed curves show the lasing spectra at threshold. (b) Lasing threshold of the high index defect TBR laser at various operating points



(a) Broad-area

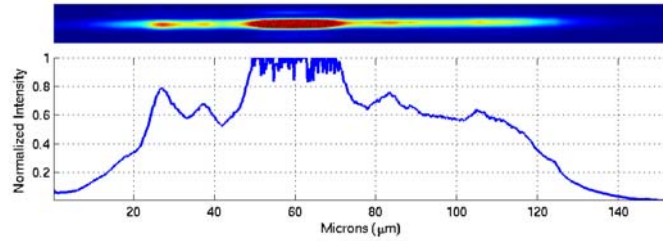


(b) TBR high index defect

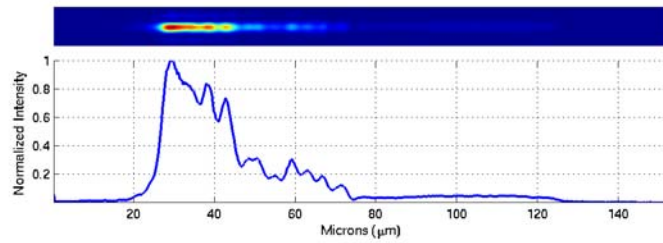


(c) TBR low index defect

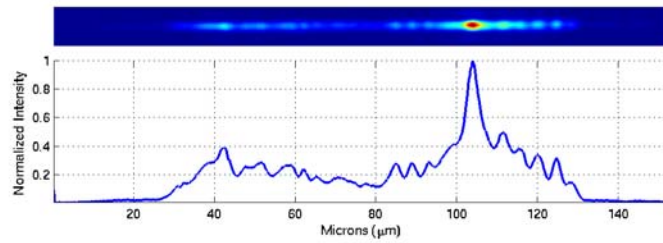
Figure 4.19: Nearfield image below threshold for (a) broad-area, (b) high index defect TBR, and (c) low index defect TBR



(a) Broad-area

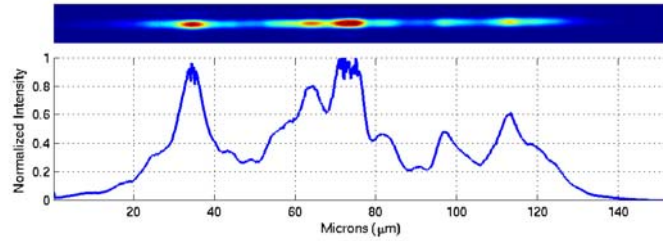


(b) TBR high index defect

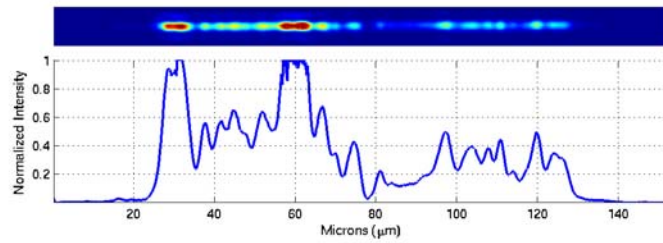


(c) TBR low index defect

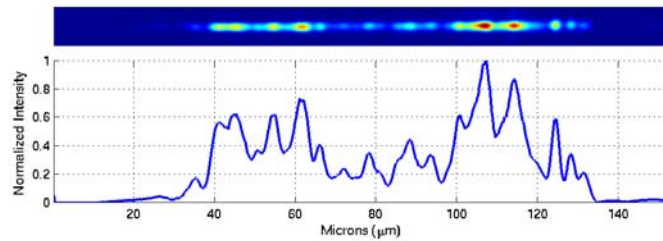
Figure 4.20: Nearfield image at threshold for (a) broad-area, (b) high index defect TBR, and (c) low index defect TBR



(a) Broad-area

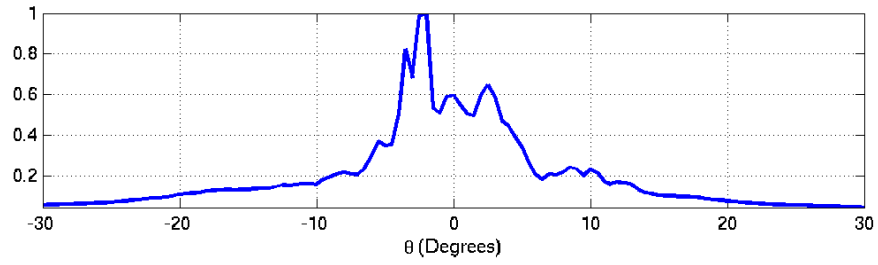


(b) TBR high index defect

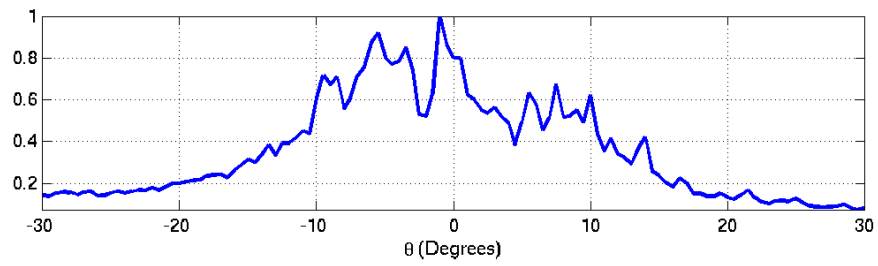


(c) TBR low index defect

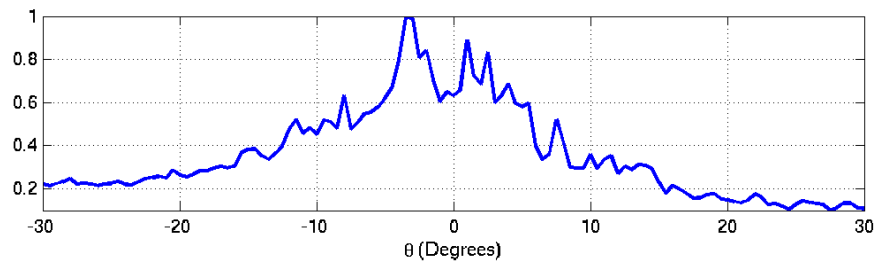
Figure 4.21: Nearfield image above threshold for (a) broad-area, (b) high index defect TBR, and (c) low index defect TBR



(a) Broad-area



(b) TBR high index defect



(c) TBR low index defect

Figure 4.22: Farfield image above threshold for (a) broad-area, (b) high index defect TBR, and (c) low index defect TBR

Chapter 5

Analysis of Results

5.1 Coupled Waveguides

The experimental results of the previous chapter clearly show behavior that deviates from the expected behavior of a TBR waveguide mode. To understand the modal structure of the device, we start with the basic model of a single slab waveguide, and consider the effect of additional identical waveguides brought into close proximity. From this pedagogical method, we will attempt to gain some insight into the more complex behavior of the actual device.

To analyze this system, we use a perturbation method adapted from reference [32]. The wave equation is:

$$\nabla^2 \mathbf{E}(\mathbf{r}, t) - \mu \partial_t^2 [\epsilon_0 \mathbf{E}(\mathbf{r}, t) + \mathbf{P}_{unpert}(\mathbf{r}, t)] = \mu \partial_t^2 \mathbf{P}_{pert}(\mathbf{r}, t) . \quad (5.1)$$

Here, \mathbf{E} is the electric field, and \mathbf{P} is the polarization as defined by the constitutive relation

$$\mathbf{D} = \epsilon_0 \mathbf{E} + \mathbf{P} = \epsilon_0 n^2 \mathbf{E} \quad (5.2)$$

where n is the index of refraction. For each individual, isolated (unperturbed)

waveguide labeled by the subscript m , let the mode be described by the unperturbed wave equation

$$\nabla^2 \mathbf{E}_m - \mu \epsilon_0 n_m^2(x) \partial_t^2 \mathbf{E}_m = 0 \quad (5.3)$$

where Eq. 5.2 was used to introduce $n_m(x)$, the index profile for the individual waveguide m apart from other waveguides. $\mathbf{E}_m = E_m(x) \exp(i\omega t - i\beta_m z)$ ($\partial_y \mathbf{E} = 0$) We will now assume that the solutions can be closely described by a superposition of the individual waveguide modes

$$\mathbf{E}(\mathbf{r}, t) = \sum_m \mathbf{A}_m \mathbf{E}_m(\mathbf{r}, t) \quad (5.4)$$

where $\mathbf{A}_m = A_m(z) \exp(-i\Delta\beta_m z)$, where $\Delta\beta_m$ accounts for a correction to the propagation constant due to the other waveguides. We now substitute Eq. 5.4 into the left hand side of Eq. 5.1.

$$\sum_m \mathbf{A}_m (\nabla^2 - \mu \epsilon_0 n_m^2(x) \partial_t^2) \mathbf{E}_m + \partial_z^2 \mathbf{A}_m - i2\beta_m \mathbf{E}_m \partial_z \mathbf{A}_m = \mu \partial_t^2 \mathbf{P}_{pert} . \quad (5.5)$$

Now by making use of Eq. 5.3 and by making the slowly varying approximation,

$$|\partial_z^2 \mathbf{A}_m| \ll \beta_m |\partial_z \mathbf{A}_m| , \quad (5.6)$$

Eq. 5.7 becomes

$$\sum_m -i2\beta_m \mathbf{E}_m \partial_z \mathbf{A}_m = \mu \partial_t^2 \mathbf{P}_{pert} . \quad (5.7)$$

Next, we multiply by E_n^* and integrate over x to obtain

$$e^{i\omega t - i\beta_m z} \partial_z \mathbf{A}_m = \frac{i}{4\omega} \int E_n^* \partial_t^2 \mathbf{P}_{pert} dx . \quad (5.8)$$

To find the perturbative polarization, we use

$$\mathbf{P}_{pert} = \sum_m \mathbf{P} - \mathbf{P}_m = \sum_m \epsilon_0(n^2(x) - n_m^2(x))\mathbf{A}_m\mathbf{E}_m \quad (5.9)$$

where \mathbf{P} is the actual polarization and \mathbf{P}_m are the unperturbed polarizations for each waveguide m and $n(x)$ is the actual, perturbed index profile. We must also use the normalization condition for planewave-like eigenmodes:

$$\nabla \times \mathbf{E} = -\mu\partial_t\mathbf{H} \rightarrow \partial_k E_i = -i\omega\mu H_j \rightarrow H_y = \frac{\beta}{\omega\mu} E_x \quad (5.10)$$

for a planewave propagating in the z -direction with transverse field components E_x and H_y . Thus, if the harmonic modes are power normalized, we can write

$$\frac{1}{2} \int \mathbf{E} \times \mathbf{H}^* dx = \frac{\beta}{2\mu\omega} \int |\mathbf{E}|^2 dx = 1 \quad (5.11)$$

Substituting Eq. 5.9 into Eq. 5.8 we obtain

$$\partial_z \mathbf{A}_m = -i\frac{\omega\epsilon_0}{4} \sum_r \mathbf{A}_r e^{-i(\beta_r - \beta_m)z} \int (n^2(x) - n_r^2(x)) E_m^* E_r dx \quad (5.12)$$

Noting that

$$\partial_z \mathbf{A}_m = e^{-i\Delta\beta_m z} \partial_z A_m - i\Delta\beta_m A_m e^{-i\Delta\beta_m z} \quad (5.13)$$

if

$$\Delta\beta_m = \frac{\omega\epsilon_0}{4} \int (n^2(x) - n_m^2(x)) |E_m|^2 dx \quad (5.14)$$

and

$$\kappa_{mn} = i\frac{\omega\epsilon_0}{4} \int (n^2(x) - n_m^2(x)) E_m E_n^* dx \quad (5.15)$$

then

$$\partial_z A_m = \sum_{n \neq m} -\kappa_{nm} A_n e^{-i(\beta_n - \beta_m + \Delta\beta_n - \Delta\beta_m)z} \quad (5.16)$$

Now let $B_m = A_m \exp(-i\beta'_m z)$. This means we are now going to describe the modes using just the coefficients, and assume they are propagating. We can then write

$$\partial_z B_m = e^{-i\beta'_m z} \partial_z A_m - i\beta'_m e^{-i\beta'_m z} A_m \quad (5.17)$$

and by substituting Eq. 5.16 into 5.17,

$$\partial_z B_m = -i\beta'_m B_m + \sum_{n \neq m} -\kappa_{nm} B_n \quad (5.18)$$

if we let $\beta'_m \equiv \beta_m + \Delta\beta_m$. If we assume that only nearest neighbor coupling is significant, then Eq. 5.18 becomes

$$\partial_z B_m = -i\beta'_m B_m - \kappa_{m+1,m} B_{m+1} - \kappa_{m-1,m} B_{m-1} \quad (5.19)$$

or in matrix notation,

$$\partial_z \mathbf{B} = \hat{\mathbf{C}} \mathbf{B} \quad (5.20)$$

$$\hat{\mathbf{C}} = \begin{bmatrix} -i\beta'_1 & -\kappa_{2,1} & 0 & 0 & \dots & 0 & 0 \\ -\kappa_{1,2} & -i\beta'_2 & -\kappa_{3,2} & 0 & \dots & 0 & 0 \\ 0 & -\kappa_{2,3} & -i\beta'_3 & -\kappa_{4,3} & \dots & 0 & 0 \\ \vdots & \vdots & \vdots & \vdots & \dots & \vdots & \vdots \\ 0 & 0 & 0 & 0 & \dots & -\kappa_{N-1,N} & -i\beta'_N \end{bmatrix} \quad (5.21)$$

$$\mathbf{B} = \begin{bmatrix} B_1 \\ B_2 \\ \vdots \\ B_N \end{bmatrix}. \quad (5.22)$$

Here, \mathbf{B} describes the z -dependence of a mode of the entire waveguide array

system. We can now assume propagating solutions of the form

$$\mathbf{B}(z) = \mathbf{B}(0)e^{-i\lambda z} \quad (5.23)$$

meaning Eq. 5.20 becomes

$$-i\lambda\mathbf{B} = \hat{\mathbf{C}}\mathbf{B} \quad (5.24)$$

and solve the related eigenvalue problem which means we are looking for values of λ such that

$$\det(\hat{\mathbf{C}} + i\lambda\hat{\mathbf{I}}) = 0 \quad (5.25)$$

where $\hat{\mathbf{I}}$ is the identity matrix. Since $\hat{\mathbf{C}}$ is an $N \times N$ square matrix, in general, there are N eigenvalues, λ , that satisfy Eq. 5.25. Thus, for a coupled waveguide array with N identical waveguides, there will be approximately N modes for each original confined mode of the original waveguide. Thus, if the isolated waveguide has M modes, then the coupled system will have on the order of $M \times N$ modes.

Fig. 5.1 shows the dispersion for several coupled waveguide systems computed numerically using the matrix method of Chapter 2. For each solid line representing the modes of the original slab waveguide predicted by the analytic theory, we find discrete modes in the coupled system equal in number to the number of waveguides coupled.

The simplest nontrivial example is the coupling of two identical slab waveguides. In this case, Eq. 5.25 reduces to

$$\det \begin{bmatrix} -i\beta'_1 + i\lambda & -\kappa \\ \kappa^* & -i\beta'_2 + i\lambda \end{bmatrix} = 0 \quad (5.26)$$

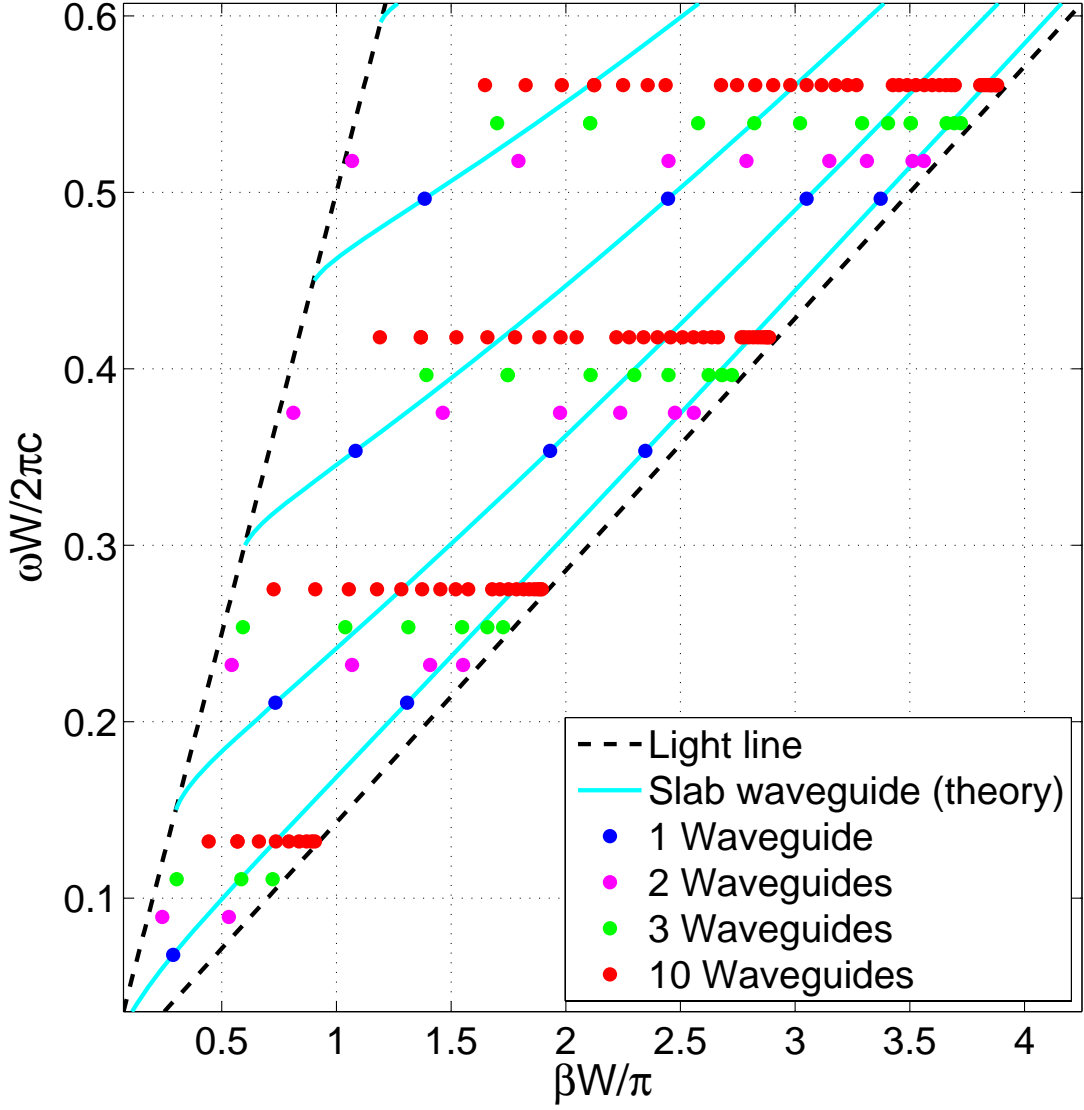


Figure 5.1: Dispersion curves calculated for various coupled waveguide systems composed of 2, 3, and 10 identical waveguides. The light lines for the high index and low index materials as well as the analytic slab waveguide theory are shown.

since from Eq. 5.15, $\kappa_{2,1} = -\kappa_{1,2}^*$. Finally, we have

$$\lambda = \frac{1}{2}(\beta'_1 + \beta'_2) \pm \frac{1}{2}\sqrt{(\beta'_1 - \beta'_2)^2 + 4|\kappa|^2} . \quad (5.27)$$

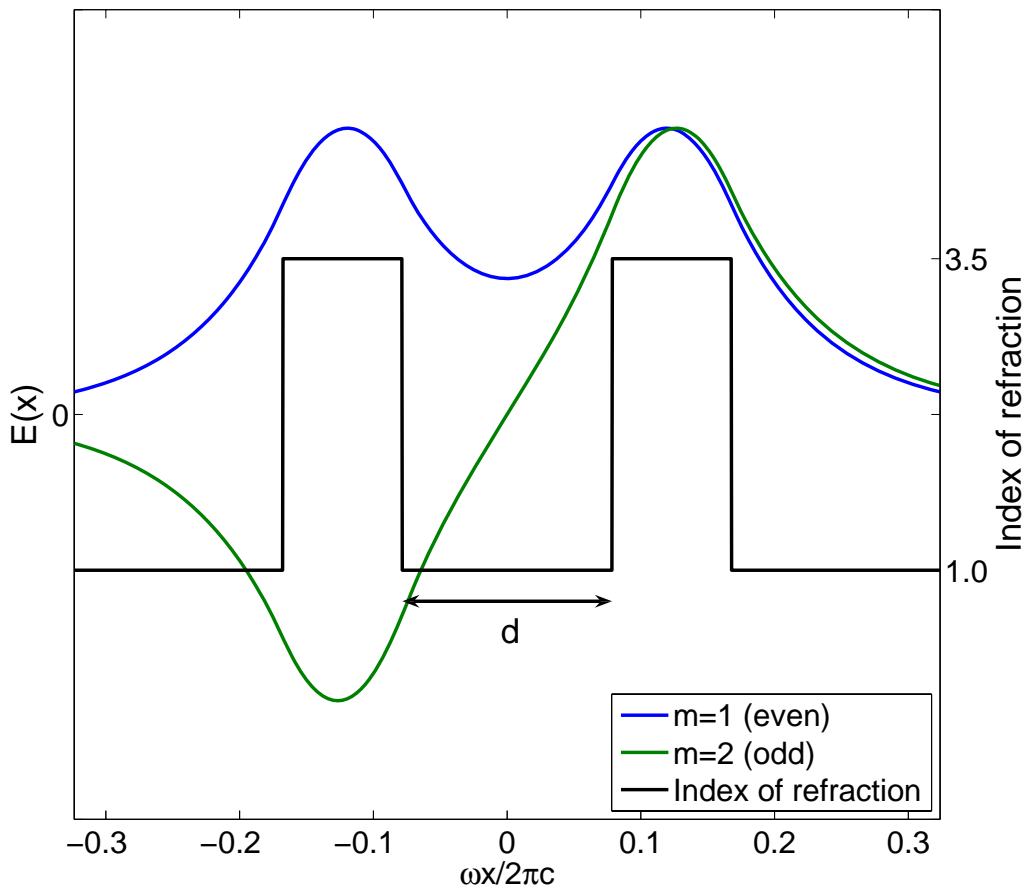


Figure 5.2: Two coupled waveguides and the mode solutions, showing the even and odd mode splitting. The separation between the two waveguides is given by d .

When the two waveguides are identical and single-mode, $\beta'_1 = \beta'_2$, so

$$\lambda_{\pm} = \beta' \pm |\kappa| . \quad (5.28)$$

This result shows that the splitting of each mode, $\Delta\lambda$, due to the coupling is proportional to the coupling strength, κ . While the exact result may not hold for all systems, the general principle still holds. From Eq. 5.15, it is clear that the larger separation decreases the overlap of the each mode field profile with

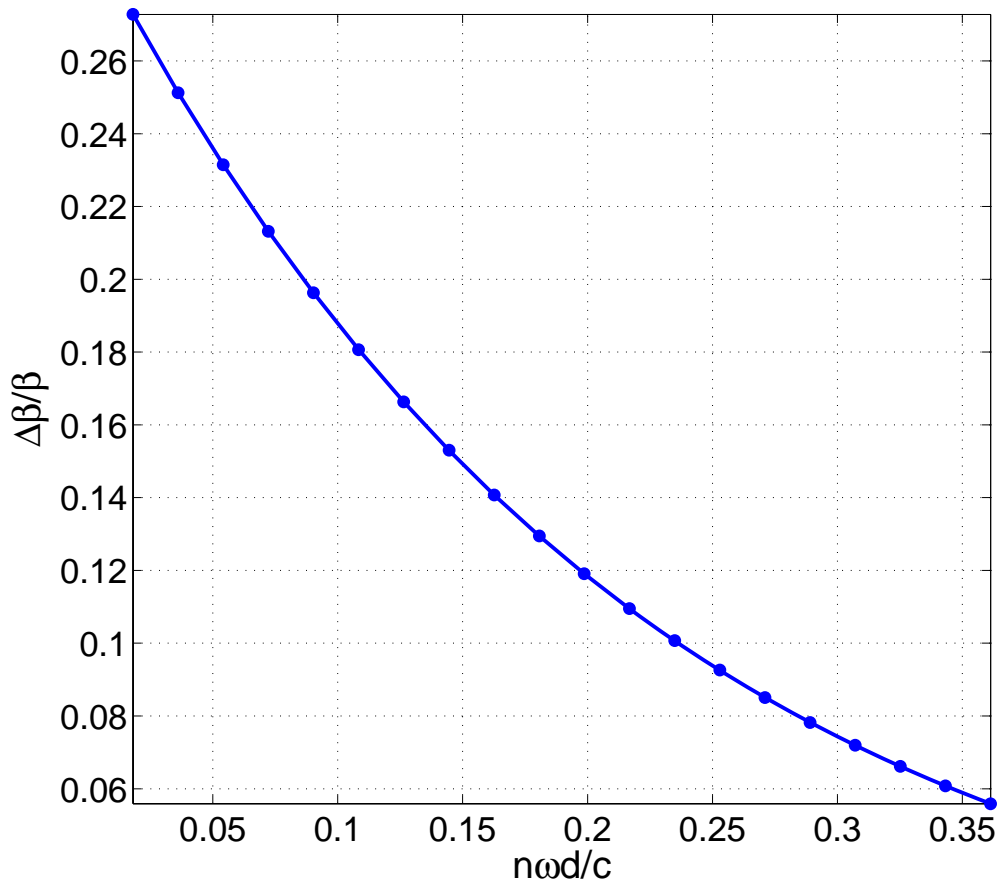


Figure 5.3: The propagation constant difference between the odd/even mode splitting as a function of the separation distance, d in Fig. 5.2. As d increases, κ decreases, reducing the separation as described by Eq. 5.28.

the index perturbation, resulting in smaller coupling. This trend is shown in Fig. 5.3 which shows the difference in the propagation constants for a two waveguide system as the distance between the waveguides is increased. Substituting Eq. 5.28 into Eq. 5.24, the eigenmodes are found to be

$$\mathbf{B}_{\pm} = \begin{vmatrix} \mp i \frac{\kappa}{|\kappa|} \\ 1 \end{vmatrix} e^{-i(\beta' \pm |\kappa|)z} . \quad (5.29)$$

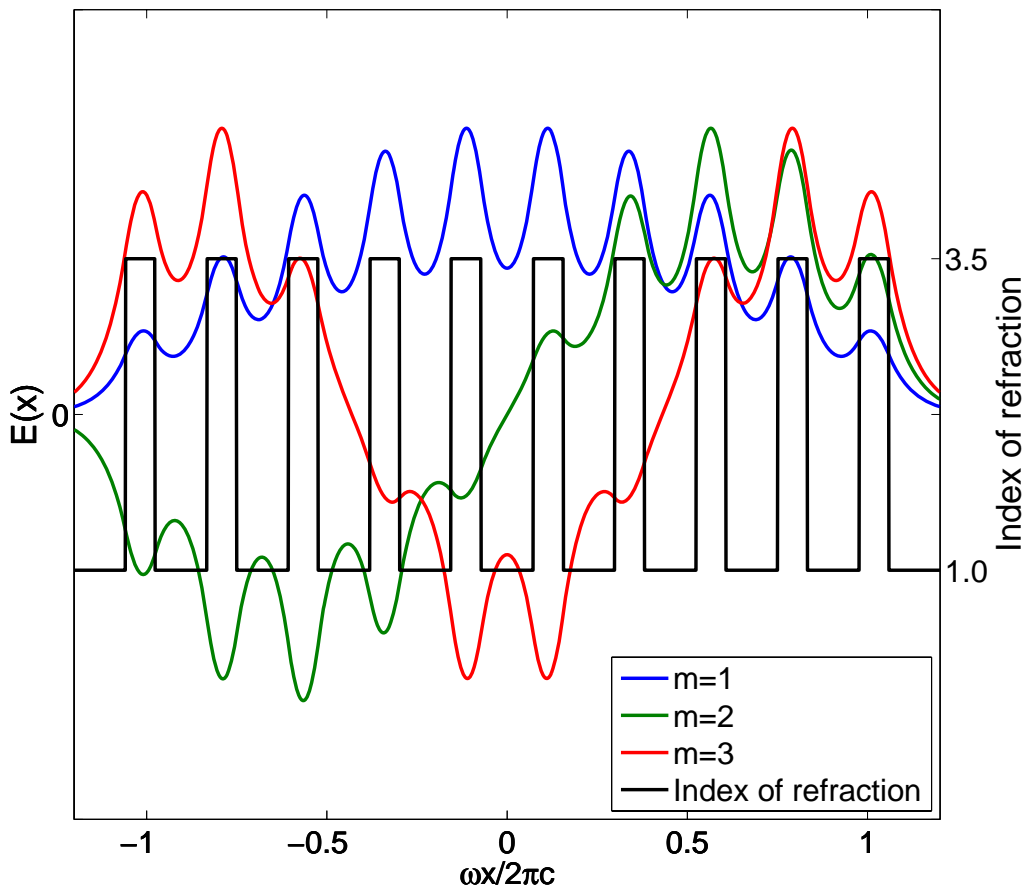


Figure 5.4: Ten coupled waveguides and the first 3 mode solutions

From Eq. 5.15, κ is a purely imaginary, positive number, so in this case, we get

$$\mathbf{B}_{\text{even}} = \begin{vmatrix} 1 \\ 1 \end{vmatrix} e^{-i(\beta' + |\kappa|)z} \quad (5.30)$$

$$\mathbf{B}_{\text{odd}} = \begin{vmatrix} -1 \\ 1 \end{vmatrix} e^{-i(\beta' - |\kappa|)z} . \quad (5.31)$$

Fig. 5.2 shows such a two waveguide coupled array along with the even and odd modes. Fig. 5.4 shows the first three modes of a 10 waveguide coupled array system.

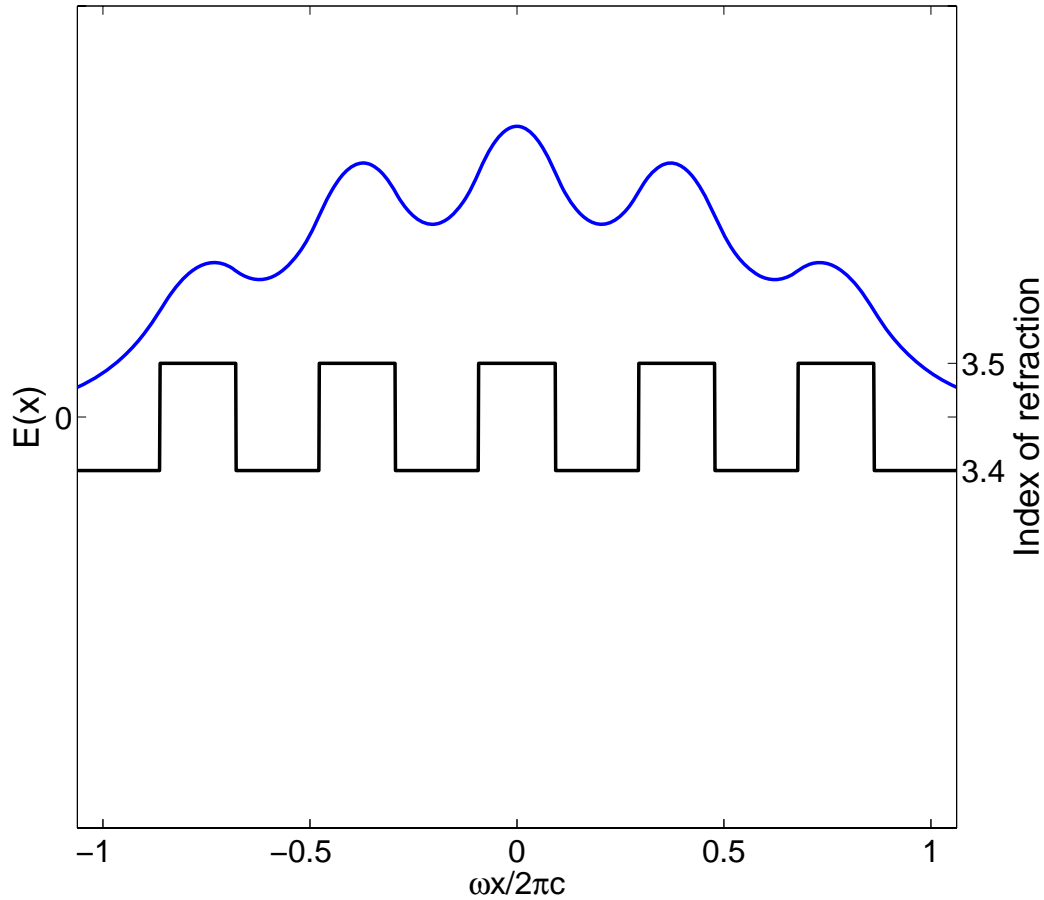


Figure 5.5: A coupled array waveguide consisting of 5 periods of Bragg reflectors that will be one half of a TBR waveguide. The lowest order mode electric field profile is shown.

5.2 Transverse Bragg Resonance Waveguides, Revisited

Using the results of the previous section, let us now reconsider the TBR waveguide structure by starting with the periodic Bragg layers of one side, as shown in Fig. 5.5. This structure can be viewed as a 5 element coupled array waveguide, or as a 5 period Bragg reflector. In Fig. 5.5, the lowest order

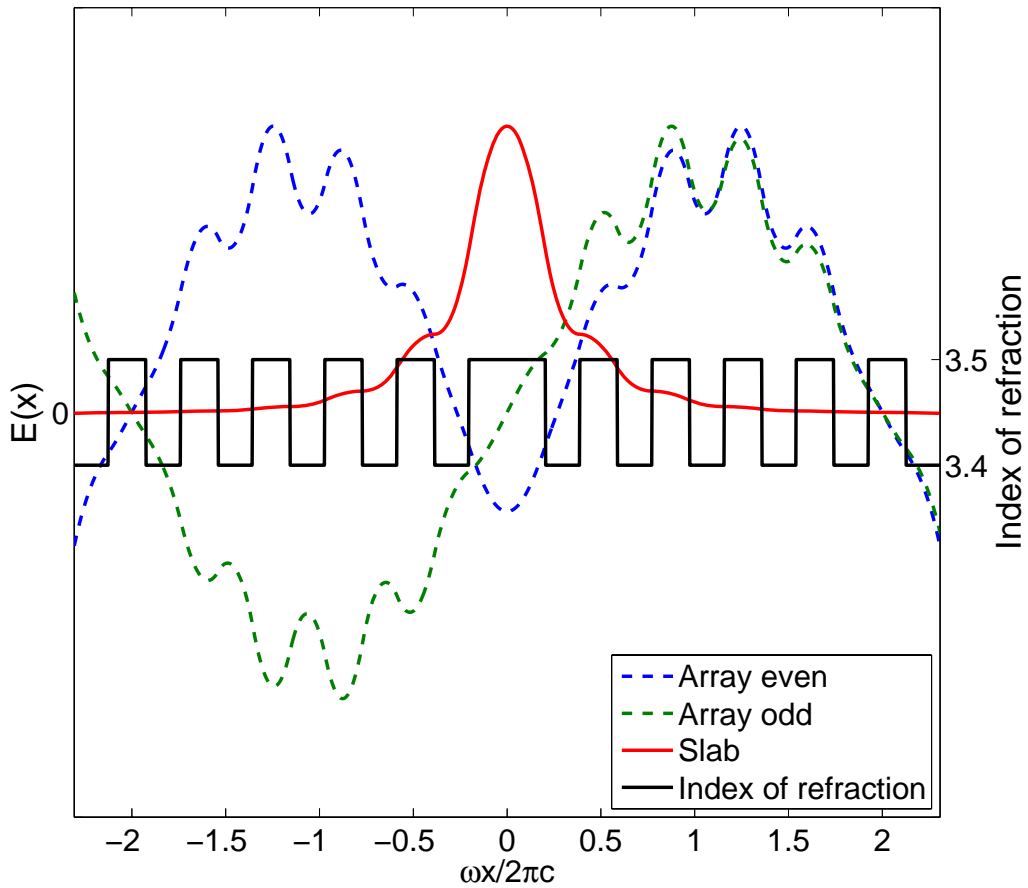


Figure 5.6: A coupled array waveguide composed of the two waveguides shown in Fig. 5.5. The even/odd splitting of the lowest order mode is shown as well as a slab mode confined to the central high index (defect) region.

mode electric field profile is also shown. Beginning with this perspective, a TBR waveguide structure is then simply two of these arrayed waveguides coupled together by some distance that happens to contain a high index region, as shown in Fig. 5.6.

If the array waveguide of Fig. 5.5 is considered as a single waveguide supporting eigenmodes (also referred to as “supermodes”), then the structure shown in Fig. 5.6 is just an arrayed waveguide created by the coupling of

two such waveguides. As we saw in the analysis of the previous section, and shown in Fig. 5.2, an array of two waveguides splits the original mode into an even and odd mode. By calculating the modes of the coupled array system of Fig. 5.6 using the matrix method of Chapter 2, we see that there are indeed two modes corresponding to the same mode splitting seen in the simple two waveguide, coupled system. These mode profiles are shown by the dashed lines in Fig. 5.6. In addition, due to the high index region in the central region (the TBR defect), there is also a mode that corresponds to a simple slab waveguide mode due to the effective index confinement.

The alternate viewpoint of a TBR waveguide and coupled mode analysis yields the Bragg confined modes shown in Fig. 5.7. As expected, there is a mode that is confined by Bragg reflection that lies within the Bragg reflection bandwidth, a defect in the so-called band gap. The field profiles of the modes on either side of the band gap are also shown. They are the equivalent radiation modes of slab waveguides. These modes are normally ignored because they are the propagating eigenmodes of the periodic Bragg material and are not confined, but rather freely radiate at the boundaries. However, as we will see later, in the presence of gain neglecting these modes is not a valid assumption.

In the coupled mode treatment of Chapter 3, the lowest order mode was found to be even. However, this is a result of assuming that the index variation was a small perturbation over an average, background index. For the devices analyzed in this chapter, and fabricated as shown in the previous chapter, the defect region is equal to the maximum or minimum index variation rather than the average index. While this has little effect on the physical properties, it can modify the symmetry of the mode due to a phase reversal at the defect boundary as shown in Fig. 5.8.

Fig. 5.9 shows the dispersion of the TBR defect mode as calculated by

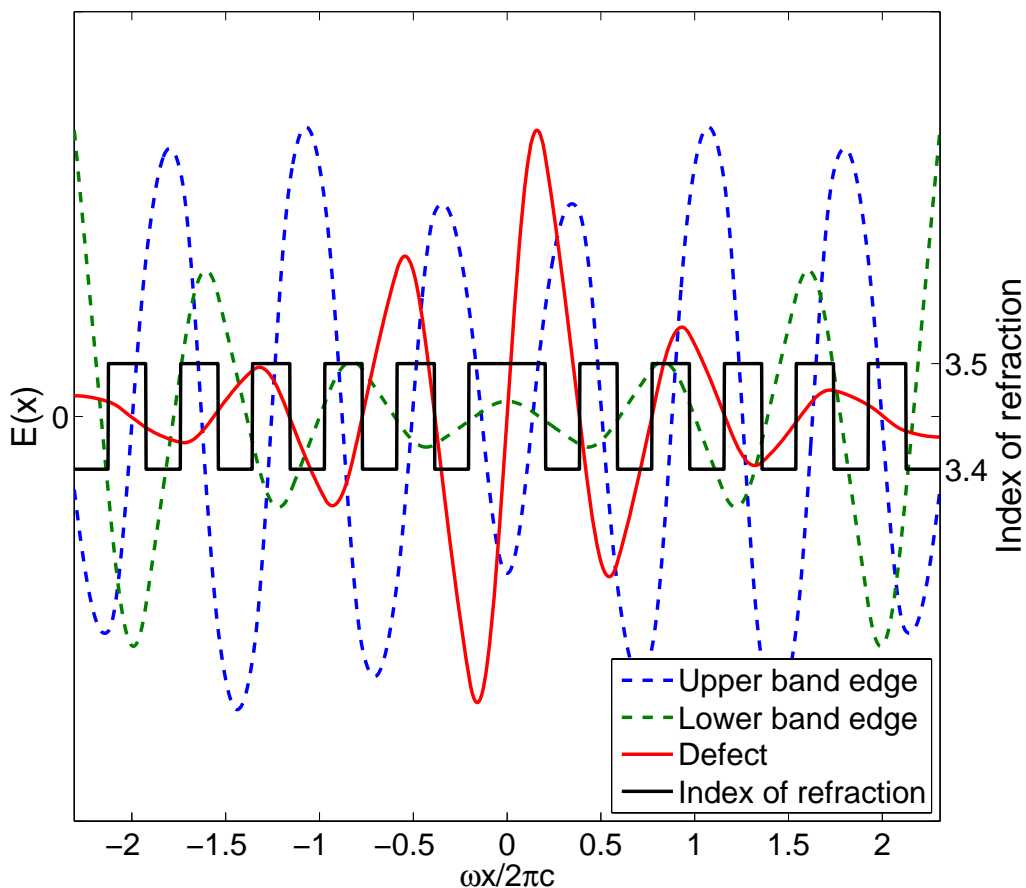
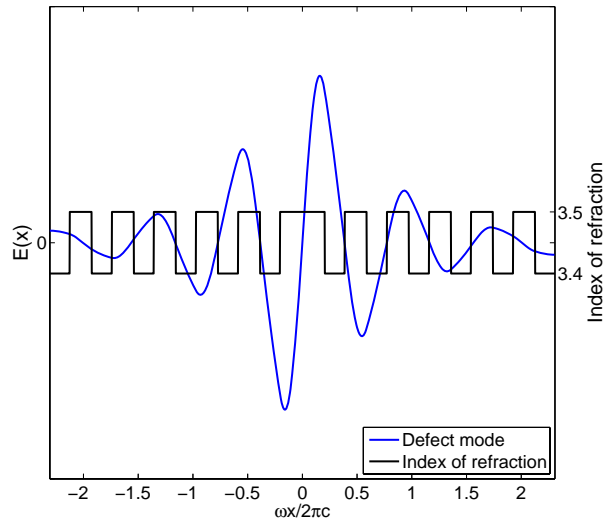


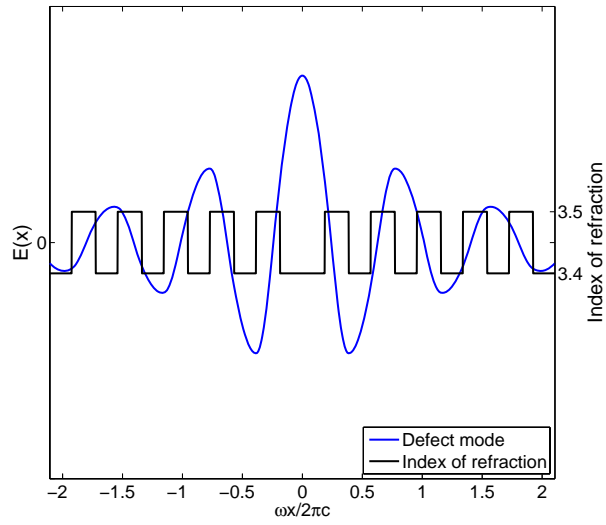
Figure 5.7: The Bragg confined defect mode as well as the two band edge modes of a TBR waveguide

the matrix method. The light lines, $\omega = (c/n)\beta$, corresponding to the high index and low index materials are also shown. Since the array modes are guided by total internal reflection, they are restricted to the region bounded by the light lines. From the figure, we see that the defect mode dispersion eventually crosses into the region demarcating index-guided modes. From the coupled mode theory, the dispersion can be described as

$$\omega = \frac{c}{\bar{n}} \sqrt{\beta^2 + \left(\frac{\pi}{\Lambda}\right)^2} \quad (5.32)$$



(a) High index defect region



(b) Low index defect region

Figure 5.8: Mode profile of the lowest order mode for a (a) high index defect region, and a (b) low index defect region

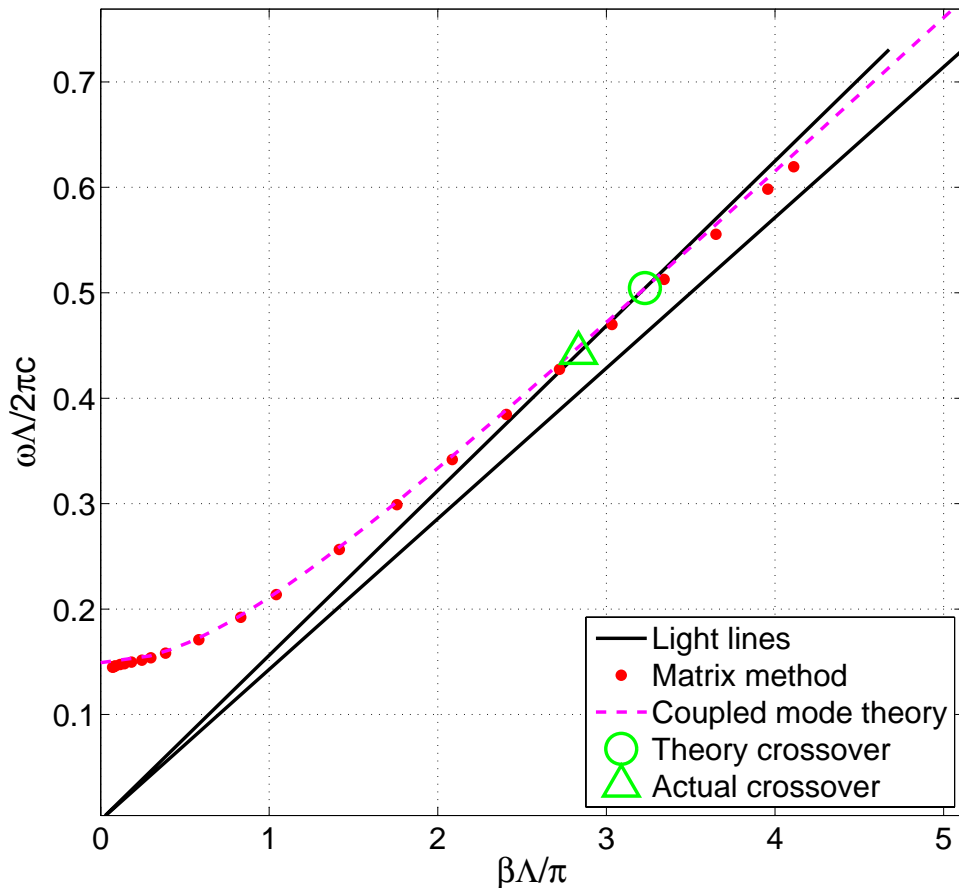


Figure 5.9: Dispersion of the TBR defect mode for the model shown in Fig. 5.7. The crossover points show that for small propagation constants, β , the modes are above the light line, and for very large propagation constants, the modes sink below the light line.

where $\bar{n} = (n_{hi} + n_{lo})/2$ is the average index and Λ is the period. From this equation we see that the dispersion asymptotically approaches the light line for the average index,

$$\lim_{\beta \rightarrow \infty} \omega = \frac{c}{\bar{n}} \beta . \quad (5.33)$$

This indicates that the crossover will always occur when the propagation constant is large enough. To find this crossover point, $\beta = \beta_x$, we can use

Eq. 5.32 and the light line for the low index material,

$$\beta_x = \frac{\pi}{\Lambda} \left(\frac{\bar{n}^2}{n_{lo}^2} - 1 \right)^{-1/2}. \quad (5.34)$$

From Fig. 5.9, we see that there is some offset between the predicted crossover point, $(\beta_x = 3.228, \omega_x = 0.504)$, and the actual point, $(\beta_x = 2.834, \omega_x = 0.443)$, approximately 14% error. However, qualitatively, it is clear that the TBR modes can be separated into two regions of interest. For small propagation constants, $\beta \ll \beta_x$, the TBR modes are above the light line while for large propagation constants, $\beta \gg \beta_x$, the TBR modes are below the light line.

This separation of the modes above and below the light line can be seen in Fig. 5.10. Within the region bounded by the light lines, the modes are confined by total internal reflection. The guided modes of the isolated slab waveguides corresponding to the high index Bragg layers ($W \approx \Lambda/2$) and the high index defect ($W \approx \Lambda$) are also shown. From the calculated modes of the structure, we see that the majority of modes are centered along the mode for the isolated waveguide due to the mode splitting seen in coupled array waveguides. However, as the number of Bragg layers increases (> 30 in the fabricated devices), these modes can be thought to compose a quasi-continuous band centered around the original slab mode. In addition, there is a mode that can be related to the slab mode of an isolated waveguide with a width equal to the defect width. Above the light line, we find the defect mode and the modes corresponding to the band edges.

In Fig. 5.11, the modal loss of the modes calculated in Fig. 5.10, $\omega\Lambda/2\pi c = 0.385$, are shown. The modal loss is calculated from the imaginary component of the propagation constant,

$$\alpha = -2\text{Im}[\beta], \quad (5.35)$$

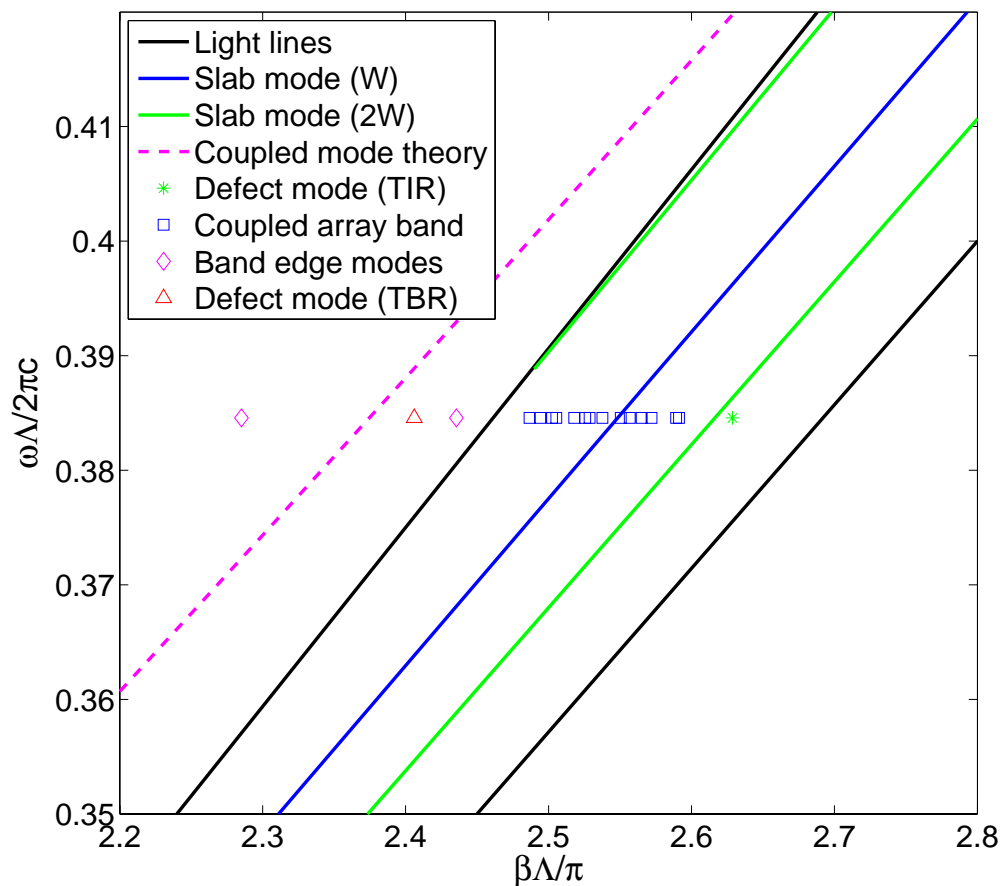


Figure 5.10: The modes of the TBR structure shown for a single frequency. The theoretical curves for TIR and TBR modes are also shown.

when the intensity is assumed to propagate with the form $|E(z)|^2 \approx |E(0)|^2 \exp(-\alpha z)$. The large relative propagation loss of the TBR modes relative to the total-internal-reflection (TIR) modes can thus be understood by the position on the dispersion curve relative to the light line. Since the TBR modes are above the light line, they couple to the slab radiation modes and are inherently lossy compared to the TIR modes, which are inherently lossless. Although the TBR modes are much lossier, we see that the density of modes is much lower than the TIR modes. Since the number of TIR modes due to

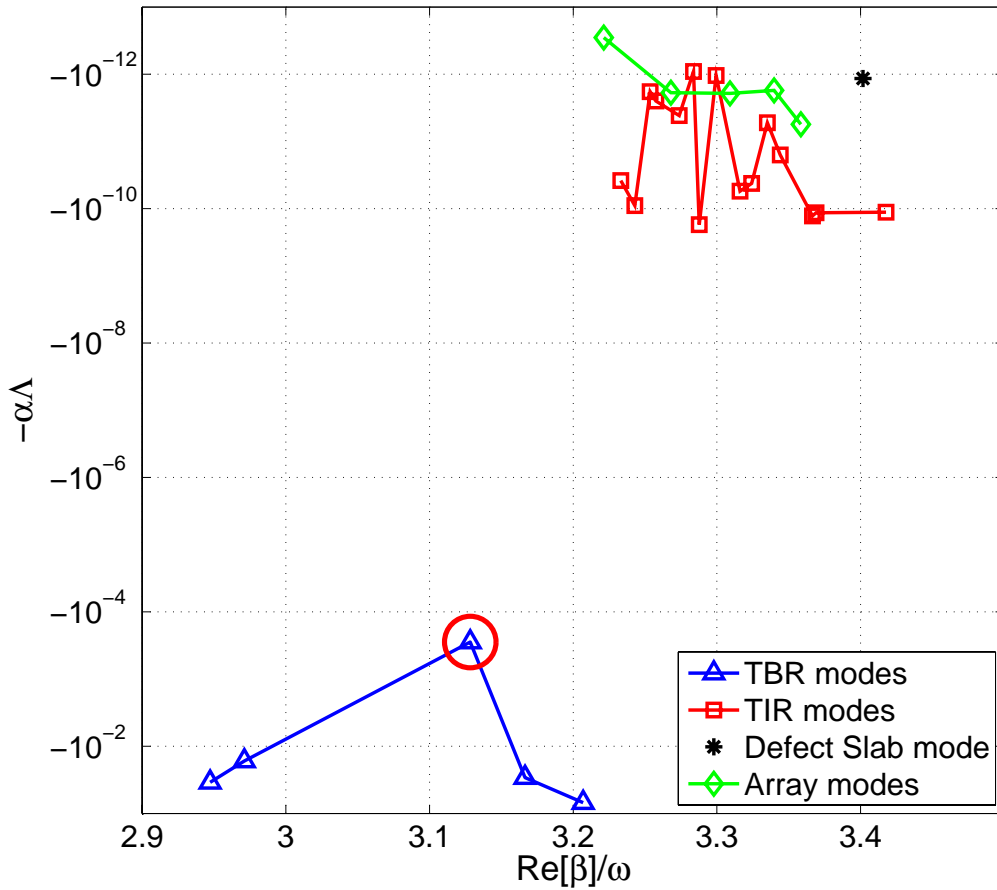


Figure 5.11: Modal loss of the modes shown in Fig. 5.10, $\omega\Lambda/2\pi c = 0.385$. The TBR defect mode is circled.

the coupled waveguide array scales with the number of waveguides, a TBR waveguide with many Bragg layers will have at least as many modes as the number of Bragg layers. Thus, to design a single mode waveguide, the TBR's lower mode density is advantageous.

Fig. 5.12 shows the loss computed at $\omega\Lambda/2\pi c = 0.598$, past the crossover point when the TBR modes are under the light line. As expected, the mode that corresponds to the TBR defect mode has low loss that is similar to the TIR modes. However, The propagation constant is no longer very different

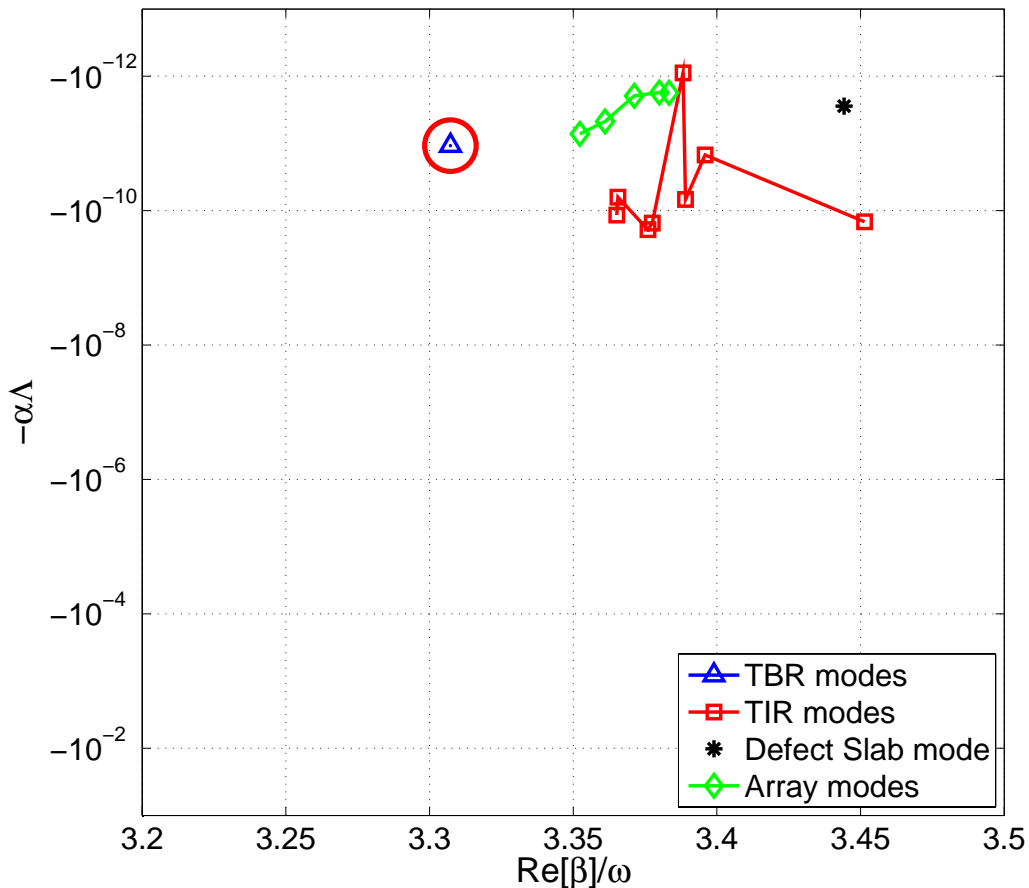


Figure 5.12: Modal loss at $\omega\Lambda/2\pi c = 0.598$. The TBR defect mode is circled.

than these TIR modes. Consequently, it is more difficult to separate the modes to achieve single-mode operation of the waveguide.

The results of Figs. 5.11 and 5.12 leads to the conclusion that the advantages of a TBR mode's single-mode operation can only be achieved by operating above the light line, when the waveguide is designed to operate with a propagation constant less than the crossover point defined in Eq. 5.34. Thus, the coupling to the radiation modes is the fundamental physical property of the TBR modes that results in the large loss discrimination of the TBR modes and is utilized to achieve single-mode operation. While

Eq. 5.34 gives the largest allowed propagation constant to isolate a TBR mode, it must be combined with Eq. 4.7 which gives the smallest allowed propagation constant for coupling light out at a facet oriented normal to the grating momentum vector ($\mathbf{k} = \pi/\Lambda$). Another consequence is that the index guided modes below the light line will always have low loss compared to the TBR modes due to the very property that creates the advantage of loss dependence. This means that these index guided modes must be suppressed through control of the longitudinal propagation constant, necessitating the use of longitudinal mode control in addition to the transverse mode control provided by the Bragg cladding.

If longitudinal mode control can be used to isolate the TBR modes from the TIR modes, we can then concern ourselves with the TBR waveguide modes. In addition to the desired defect mode, there exist band edge modes that are composed of the propagating eigenmodes of the periodic Bragg medium. Fig. 5.13 shows the modal loss ($\exp(\alpha\Lambda) < 1$) and gain ($\exp(\alpha\Lambda) > 1$) of the defect mode and the two nearest neighbor band edge modes. They have been labeled by the effective index of each mode, $n_{\text{effective}}/c \equiv \text{Re}[\beta]/\omega$. As the material gain is increased, all the modes experience a proportionate increase in their modal gains. This means that with enough pump power, the band edge modes are equally valid lasing modes. If the modal loss separation is large enough, by increasing the band gap size, the threshold difference may be sufficient to guarantee single-mode operation at the desired operating point. However, in order to expand the defect modal volume for high power operation, the index contrast is reduced. This, in turn, reduces the band gap size, reducing the modal gain discrimination. Ideally, we would like a method for independently increasing the modal loss of the band edge modes.

Fig. 5.14 shows the mode profiles of the defect mode and a band edge mode. Outside the grating region, the radiation loss into the substrate ma-

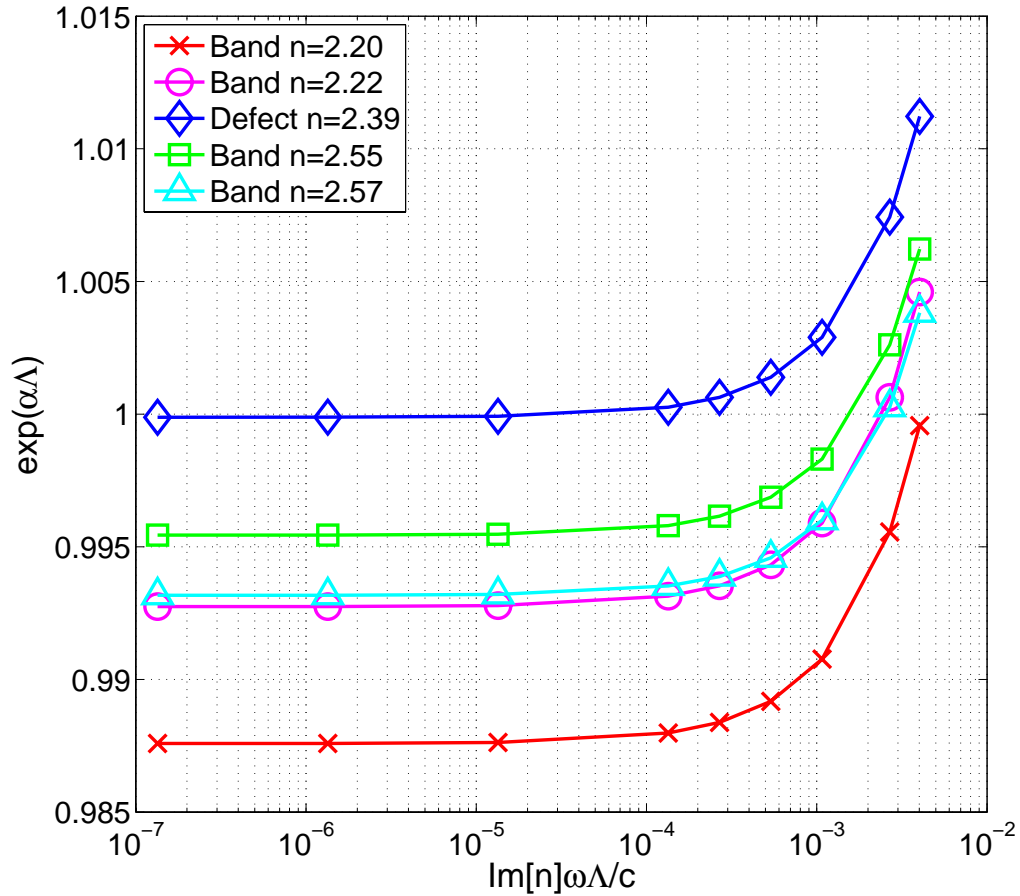


Figure 5.13: The modal loss/gain of the defect mode, effective index 2.39, and the 2 nearest band edge modes on either side as the material gain of the laser is increased

material is clearly observed. However, it appears that the band edge mode has a much larger radiation pattern in the substrate than the defect mode. This observation suggests that the band edge mode has a greater dependence on the material outside the grating than the defect mode.

Fig. 5.15 shows the modal loss dependence of the defect mode and the two neighboring band edge modes with the largest effective index for the the structure shown in Fig. 5.14 as the material loss in the region outside the

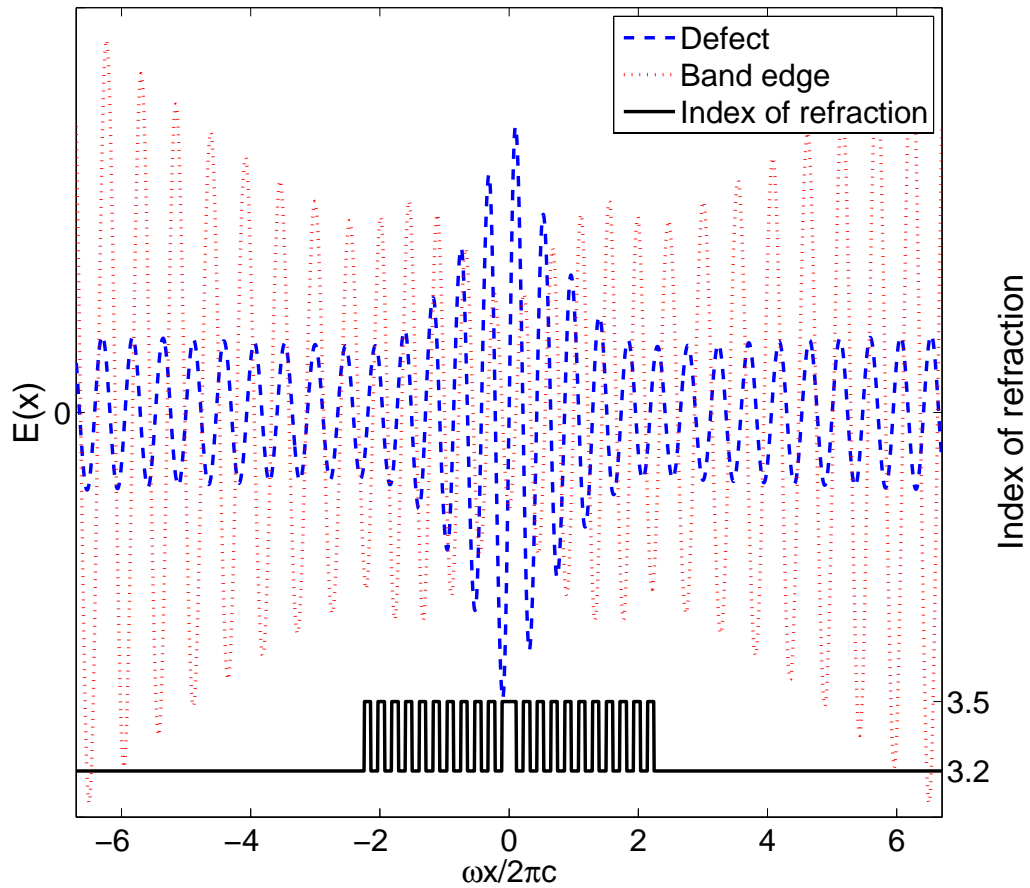


Figure 5.14: Mode profiles of the defect mode and a band edge mode showing the radiation into the substrate outside the grating region for a passive, lossless waveguide structure

grating is increased while the grating region remains lossless. As suspected, the defect mode is affected very little. However, the band edge modes experience a significantly larger loss as the material loss outside the grating region is increased. This result suggests that increasing the loss outside the grating region can increase the modal loss difference between the defect mode and the band edge modes. Fig. 5.16 shows the same structure and modes of Fig. 5.14 when the material loss outside the grating region is increased.

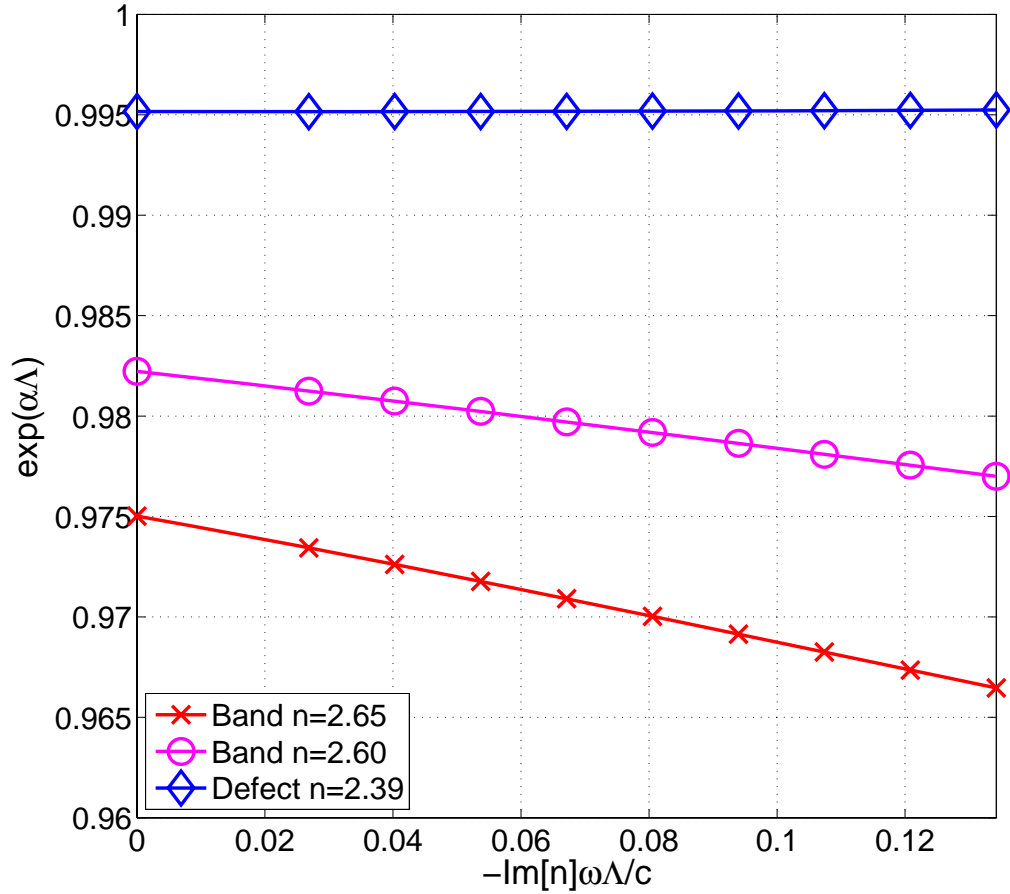


Figure 5.15: Modal loss dependence of the defect mode and two neighboring band edge modes of the structure shown in Fig. 5.14 as the material loss outside the grating region is increased

The final piece to the TBR waveguide is to check the mode profile in the presence of gain. Fig. 5.17 shows the mode profile of the defect mode and band edge mode for a lossless grating region. This structure has twice as many Bragg layers as in the structure for Fig. 5.15, showing the reduced radiation loss of the defect mode, while not affecting the band edge mode radiation loss. Fig. 5.18 shows the same structure, and the same modes in the presence of material gain within the grating region. The qualitative

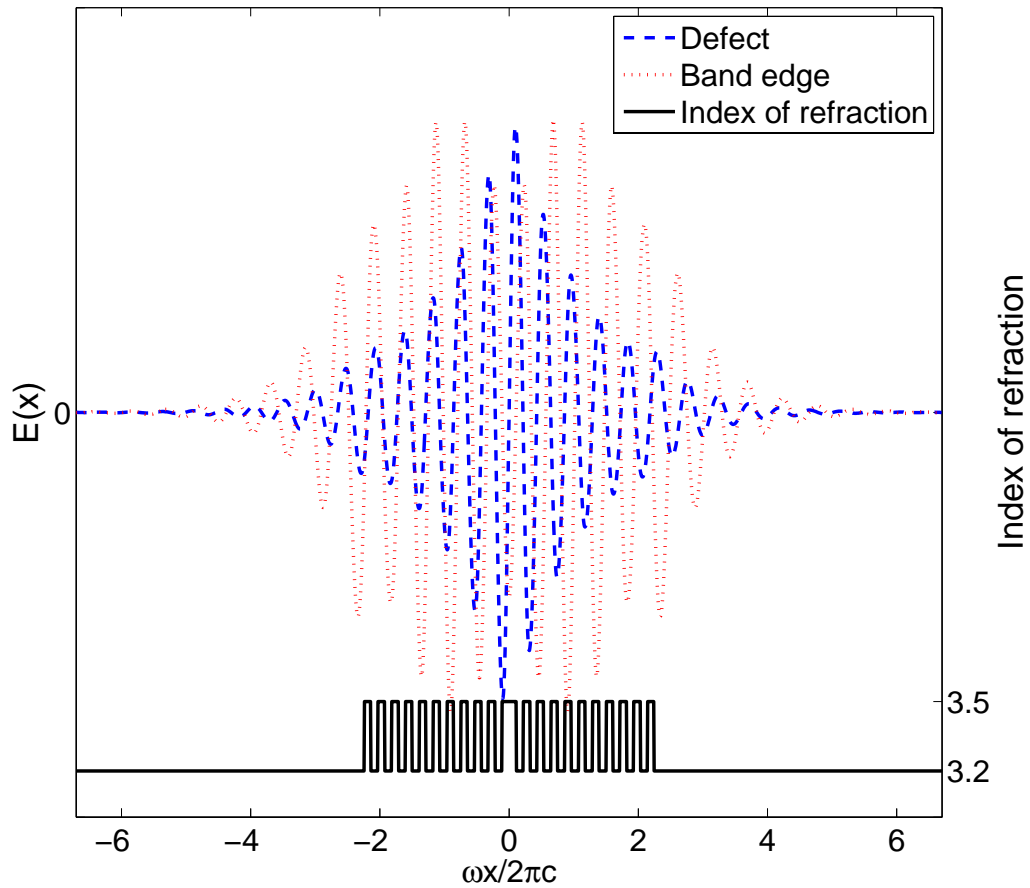


Figure 5.16: Mode profiles of the defect mode and a band edge mode showing the absorption of the substrate radiation leakage shown in Fig. 5.14 when the material loss outside the grating region is increased sufficiently

behavior, or the mode shape, is the same in both cases. However, in Fig. 5.18, the amplitude of the radiation leakage is reduced in relation to the field within the grating region. This reduced ratio is most apparent for the band edge mode. While the gain in the grating region amplifies the field within the grating section, there is no corresponding gain in the substrate, and the field appears to decay.

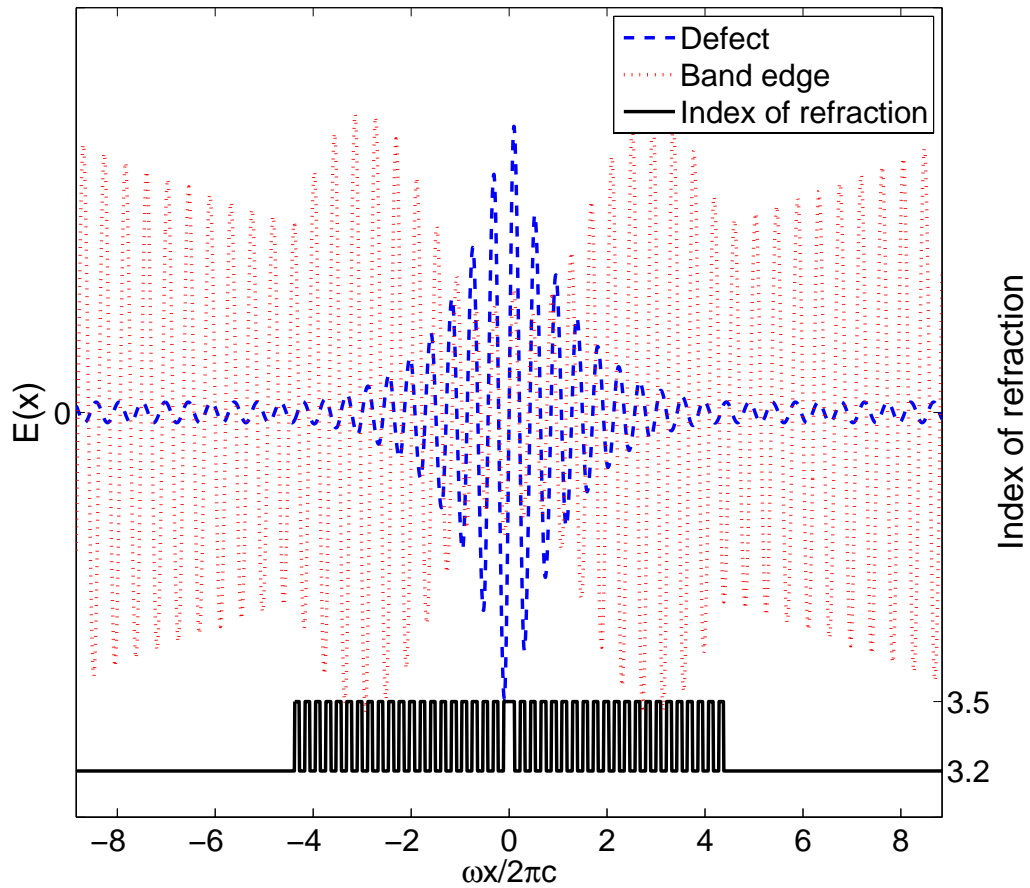


Figure 5.17: Mode profile of the defect mode and band edge mode for a lossless grating region. Note that there are twice as many Bragg layers as in the structure for Fig. 5.15, reducing the radiation loss of the defect mode. The radiation of the band edge mode is not effected.

5.3 Device Simulations

To analyze the actual TBR laser structure fabricated, the 3-dimensional vector FDTD method was used. Although this method is capable of simulating the entire laser structure, the computational requirements are extremely steep. However, as we have seen previously, the large modal loss discrimination of the TBR modes means that we can limit our attention to the defect

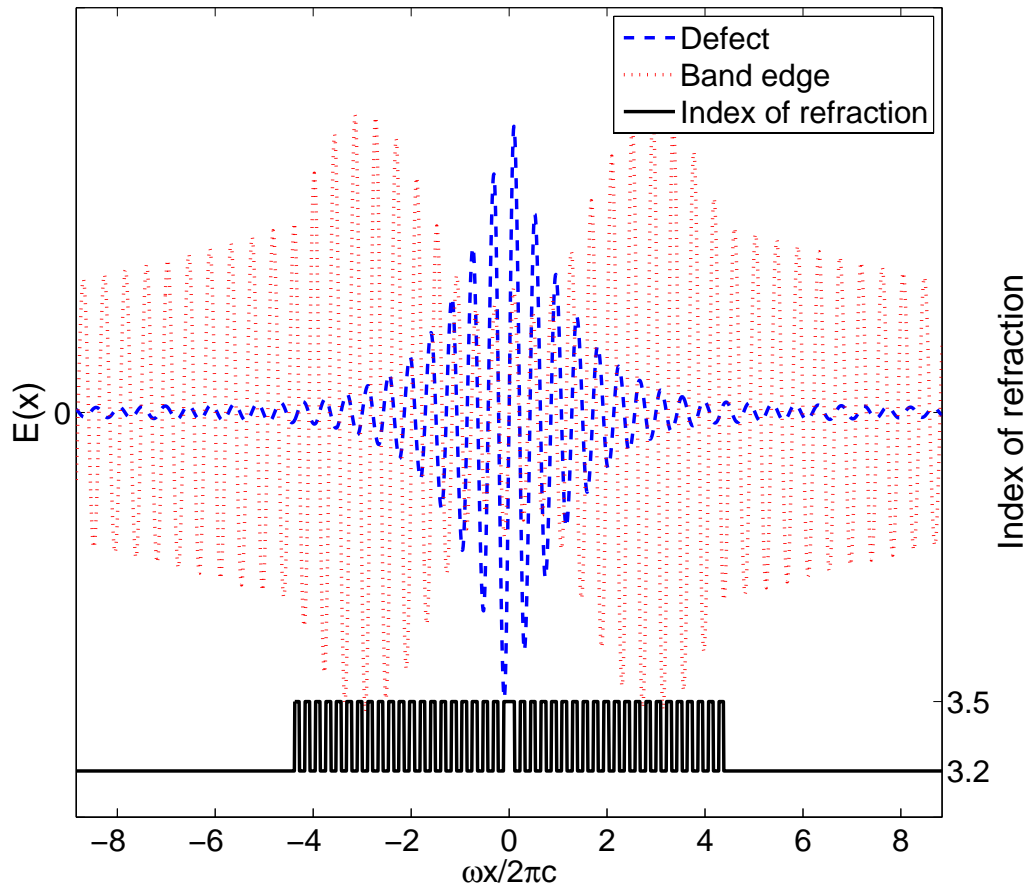


Figure 5.18: Mode profile of the defect mode and band edge mode shown in Fig. 5.17 in the presence of material gain in the grating region displaying the same qualitative behavior

and two nearest band edge modes. Further, we know that the defect mode must lie within the band gap. Therefore, if the band gap is sufficiently narrow compared to the other spectral features, knowing the band edges can fully describe our TBR waveguide modal structure. The band edges are particularly cost effective to compute because they are the modes of the periodic Bragg structure. This means that periodic boundary conditions can be employed to limit the computational domain to a single unit cell rather than the full

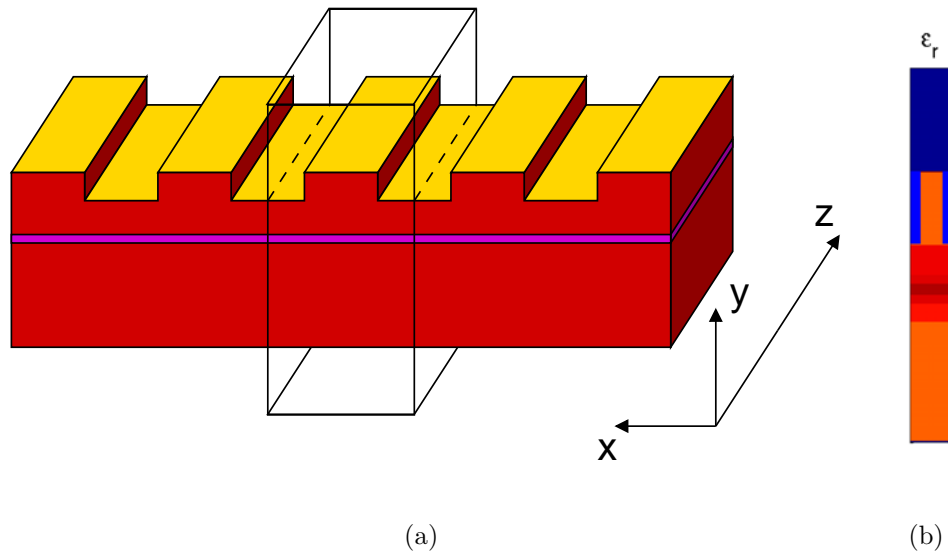


Figure 5.19: (a) The surface grating semiconductor structures. The box shows the unit cell used for calculating the band structure. (b) The index contours of the actual simulation domain

device, which can contain nearly 100 unit cells.

Fig. 5.19(a) shows an example of the periodic Bragg structure fabricated by a surface grating in semiconductor. The box outline shows the unit cell that is simulated with periodic boundary conditions. Fig. 5.19(b) shows the index contours of the actual simulation domain. By setting the propagation constant in the z direction to zero (no propagation in the z direction) and scanning the wave vector in the x direction, we obtain the band diagram in Fig. 5.20. When $k_x\Lambda = \pi$, at the Brillouin zone edge, we reach the transverse phase condition for Bragg reflection. The inset shows in detail the TE and TM polarization band gaps at the zone edge. Fig. 5.21 shows the field intensity distributions for the four modes at the zone edge, the upper and lower band edges for each polarization.

Fig. 5.22 shows the dispersion of the propagating band edge modes for the

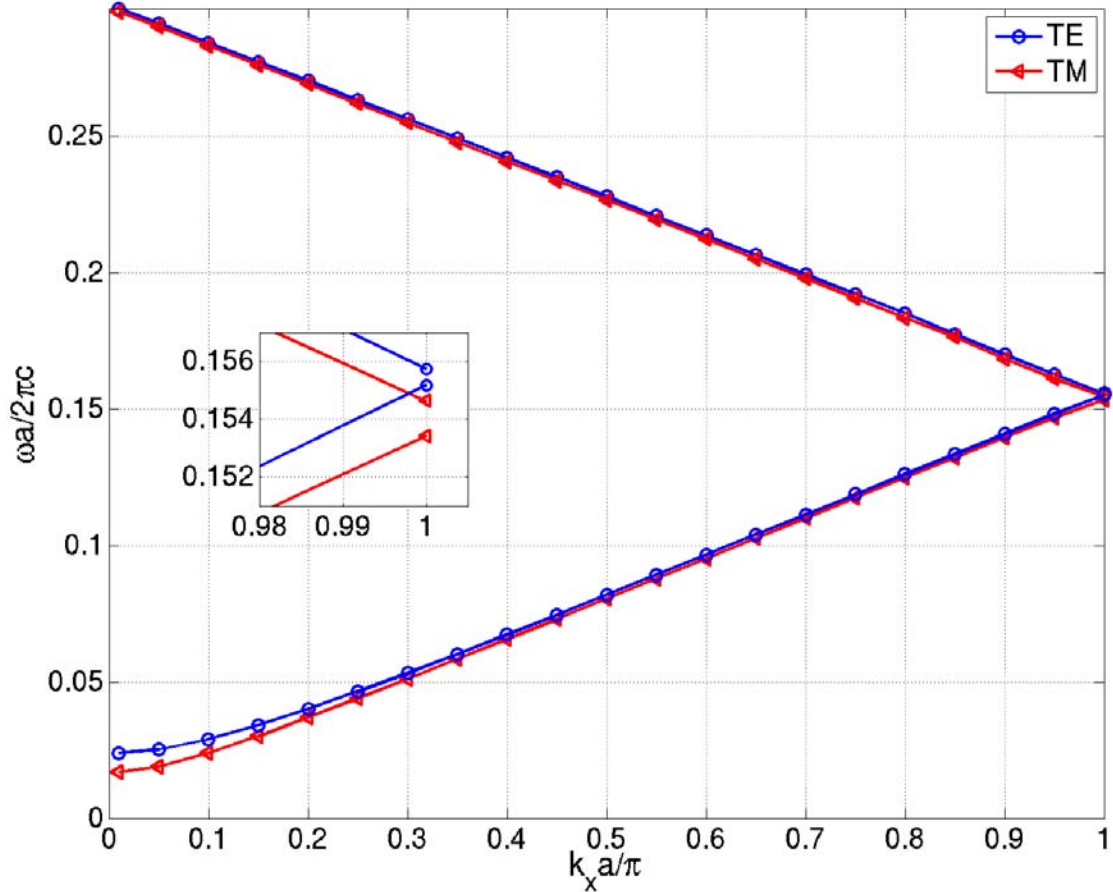
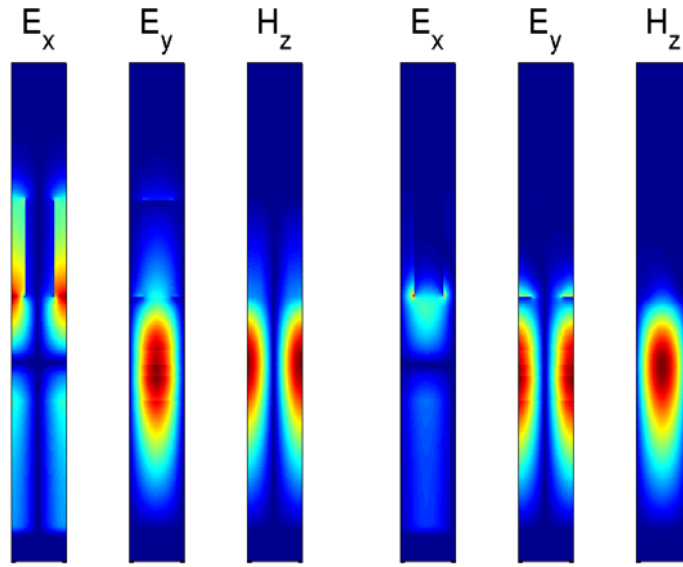


Figure 5.20: Band diagram of the surface grating structure. The inset shows the Brillouin zone edge.

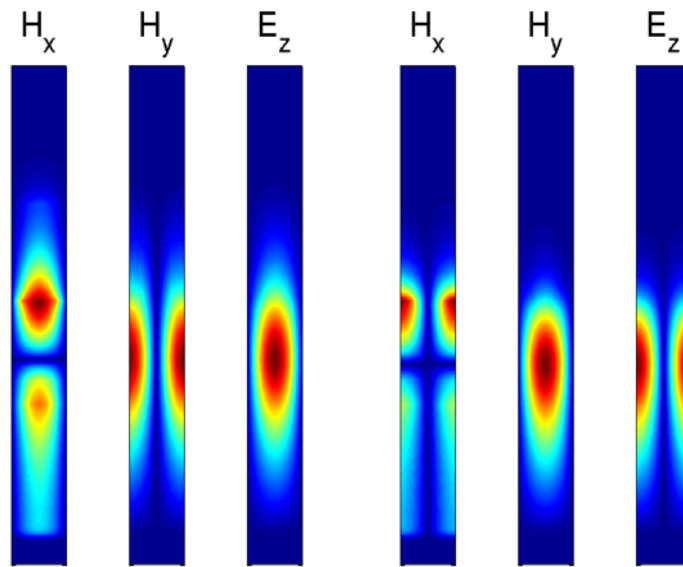
actual fabricated device. The light lines for InP ($n = 3.17$) and InGaAs ($n = 3.55$) are shown as the approximate, relevant substrate and core indices. The crossover point appears to be approximately $\beta_x \Lambda \approx 3.2\pi$, $\omega \Lambda/2\pi c \approx 0.48$. The lasing wavelength measured for the devices was approximately $1.455\mu\text{m}$. This means that for the fabricated structure with a grating period of $1.5\mu\text{m}$, the normalized frequency, $\omega \Lambda/2\pi c$, is approximately 1.03. This puts the operating point well past the crossover point, and any TBR mode would

most likely be below the light line making it difficult to distinguish any TBR mode from nearby TIR modes similar to the example in Fig. 5.12. It is concluded that this is the reason a clear defect mode was not observed.



(a) TE lower band edge

(b) TE upper band edge



(c) TM lower band edge

(d) TM upper band edge

Figure 5.21: Intensity distribution of fields at the Brillouin zone edge

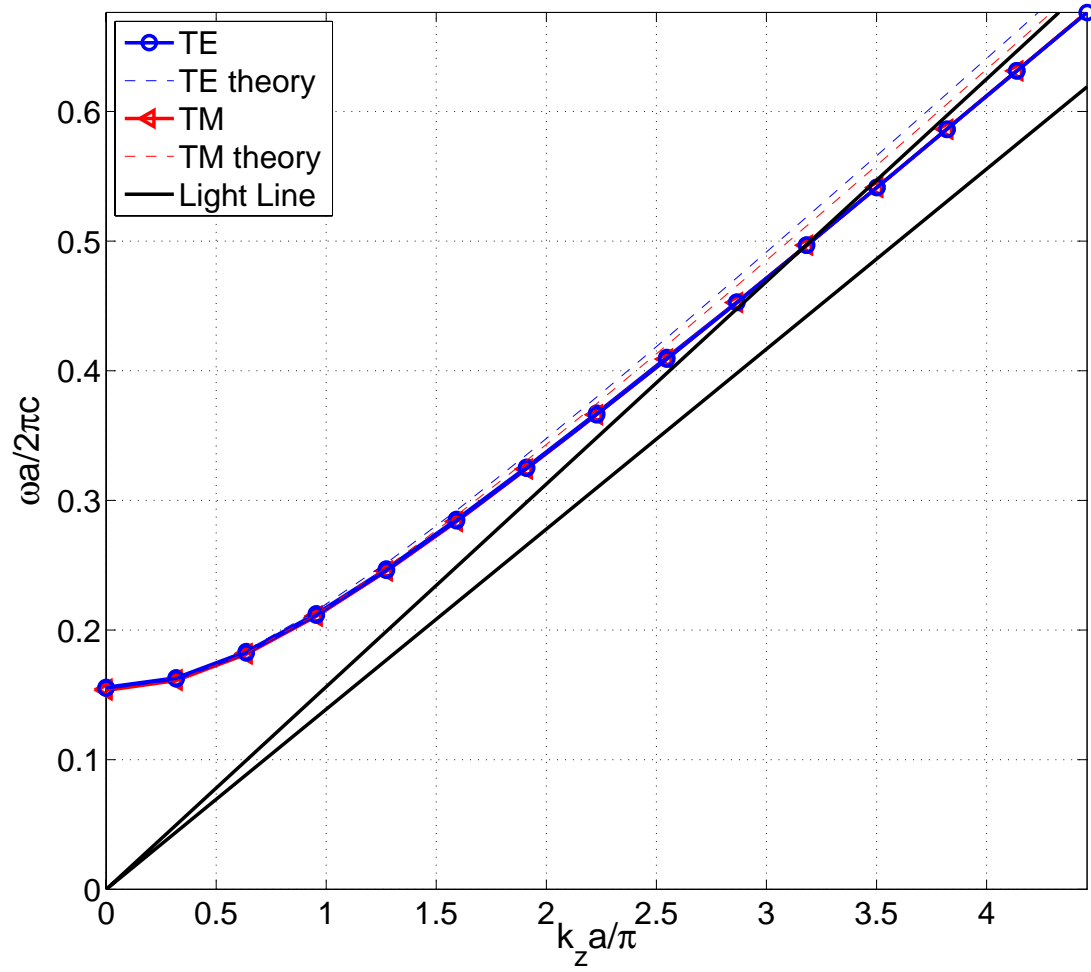


Figure 5.22: Dispersion of the propagating band edge modes for the actual fabricated device

Chapter 6

Conclusion

Controlling the electromagnetic modes in a laser cavity is the key to designing high power lasers. Rather than just the total output power from the facet, the more important metric is the total useful power coupled into an optical system. While a large modal volume is necessary for reducing the energy density at the facet, this is contrary to the requirement for single spatial mode operation in a waveguide utilizing total-internal-reflection for confinement. We have seen that grating confinement via Brag reflection allows for modes above the light line, and if these lossy modes can be isolated, the inherent loss mechanism by radiation into the substrate creates a large modal loss discrimination that can favor the defect mode for single spatial mode operation.

While the transverse grating is necessary to restrict the transverse wavevector and support Bragg confined modes above the light line, the longitudinal wavevector must also be controlled to disallow the modes below the light line. If the waveguide is designed to allow only propagation constants less than the crossover propagation constant, β_x , the modal separation can be large enough to isolate the TBR defect mode. Thus, periodicity in a single direction is insufficient to prevent multimoded waveguiding in a transverse grating waveguide. By including a second periodicity in the longitudinal direction,

the longitudinal mode can also be controlled to achieve a truly single-mode, large modal volume, high power laser.

Due to the lack of longitudinal mode control, as well as an operating point beyond the crossover point, $\beta > \beta_x$, the fabricated devices did not demonstrate single-mode behavior of the TBR defect mode. However, the advantages of designing a waveguide that operates above the light line have been demonstrated theoretically, and is a method of modal control that has much potential to be exploited. By removing the traditional restriction of guiding below the light line by total internal reflection a new degree of freedom is made possible and the spatial modes of a large modal volume laser may finally be tamed.

Bibliography

- [1] S. Adachi. Material properties of $\text{In}_{1-x}\text{Ga}_x\text{As}_y\text{P}_{(1-y)}$ and related binaries. *J. Appl. Phys.*, 53:8775–8792, 1982.
- [2] N. W. Ashcroft and N. D. Mermin. *Solid State Physics*. Harcourt, 1976.
- [3] J.-P. Bérenger. A perfectly matched layer for the absorption of electromagnetic waves. *J. Comput. Phys.*, 127:363–379, 1994.
- [4] D. Botez and L. J. Mawst. Phase-locked laser arrays revisited. *IEEE Circuits Devices Mag.*, 12:25–32, 1996.
- [5] A.Y. Cho, A. Yariv, and P. Yeh. Observation of confined propagation in bragg waveguides. *Appl. Phys. Lett.*, 30:471–472, 1977.
- [6] J. M. Choi, W. Liang, Y. Xu, and A. Yariv. Loss optimization of transverse bragg resonance waveguides. *J. Opt. Soc. Am. A*, 21:426–429, 2004.
- [7] E. Chow, S. Y. Lin, J. R. Wendt, S. G. Johnson, and J. D. Joannopoulos. Quantitative analysis of bending efficiency in photonic-crystal waveguide bends at $\lambda = 1.55\mu\text{m}$. *Opt. Lett.*, 26:286–288, 2001.
- [8] B. R. D’Urso. *Coupled Semiconductor Cavities with 2-D Photonic Bandgap Crystal Mirrors*. Undergraduate thesis, California Institute of Technology, 1998.

- [9] K. M. Dzurko, D. R. Scifres, A. Hardy, D. F. Welch, and R. G. Waarts. Single mode broad area distributed bragg reflector ring oscillators. *Appl. Phys. Lett.* , 61:2389–2391, 1992.
- [10] S. Fan, J. N. Winn, A. Devenyi, J. C. Chen, R. D. Meade, and J. D. Joannopoulos. Guided and defect modes in periodic dielectric waveguides. *J. Opt. Soc. Am. B* , 17:1267–1272, 1995.
- [11] S. D. Gedney. An anisotropic perfectly matched layer-absorbing medium for the truncation of fdtd lattices. *IEEE Trans. Antennas Propag.* , 44:1630–1639, 1996.
- [12] W. Gropp, E. Lusk, and A. Skjellum. *Using Mpi: Portable Parallel Programming With the Message-Passing Interface*. MIT Press, 2nd edition, 1999.
- [13] C. Gulffaut and K. Mahdjoubi. A parallel fdtd algorithm using the mpi library. *IEEE Trans. Antennas Propag.* , 43:94–103, 2001.
- [14] R. L. Koch, P. J. Corvini, and W. T. Tsang. Anisotropically etched deep gratings for inp/ingaasp optical devices. *J. Appl. Phys.* , 62:3461–3463, 1987.
- [15] W. Liang, Y. Xu, J. M. Choi, and A. Yariv. Engineering transverse bragg resonance waveguides for large modal volume lasers. *Opt. Lett.* , 28:2079–2081, 2003.
- [16] M. Lončar, D. Nedeljkovič, T. P. Pearsall, J. Vučković, A. Scherer, S. Kuchinsky, and D. C. Allan. Experimental and theoretical confirmation of bloch-mode light propagation in planar photonic crystal waveguides. *Appl. Phys. Lett.* , 80:1689–1691, 2002.

- [17] D. Marcuse. *Theory of Dielectric Optical Waveguides*. Academic Press, Inc., 2nd edition, 1991.
- [18] R. W. Martin, S. L. Wong, R. J. Warburton, R.J. Nicholas, A. D. Smith, M. A. Gibbon, and E. J. Thrush. Variations of the hole effective masses induced by tensile strain in $\text{In}_{1-x}\text{Ga}_x\text{As}(\text{p})/\text{InGaAsP}$ heterostructures. *Phys. Rev. B* , 50:7660–7667, 1994.
- [19] M. Nakamura and A. Yariv. Optically pumped GaAs surface laser with corrugation feedback. *Appl. Phys. Lett.* , 22:515–516, 1973.
- [20] M. Notomi, A. Shinya, K. Yamada, J. Takahashi, C. Takahashi, and I. Yokohama. Structural tuning of guiding modes of line-defect waveguides of silicon-on-insulator photonic crystal slabs. *IEEE J. Quantum Electron.* , 38:736–742, 2002.
- [21] O. Painter, R. K. Lee, A. Scherer, A. Yariv, J. D. O’Brien, P. D. Dapkus, and I. Kim. Two-dimensional photonic band-gap defect mode laser. *Science*, 284:1819–1821, 1999.
- [22] B. Pezeshki, M. Hagberg, M. Zelinski, S. D. DeMars, E. Koley, and R. J. Lang. 400-mw single-frequency 660-nm semiconductor laser. *IEEE Photon. Technol. Lett.* , 11:791–793, 1999.
- [23] K. Sakoda. Optical transmittance of a two-dimensional triangular photonic lattice. *Phys. Rev. B*, 51:4672–4675, 1995.
- [24] J. R. Sheats and B. W. Smith, editors. *Microlithography: Science and Technology*. Marcel Dekker, Inc., 1998.
- [25] M. Snir and W. Gropp. *MPI: The Complete Reference*. MIT Press, 2nd edition, 1998.

- [26] S. J. Sweeney, L. J. Lyons, A. R. Adams, and D. A. Lock. Direct measurement of facet temperature up to melting point and cod in high-power 980-nm semiconductor diode lasers. *IEEE J. Sel. Topics Quantum Electron.*, 9:1325–1332, 2003.
- [27] A. Taflove and S. C. Hagness. *Computational Electrodynamics: The Finite-Difference Time-Domain Method*. Artech House, Inc., 3rd edition, 2005.
- [28] T. Tsukada. Gaas-ga(1-x)al(x)as buried-heterostructure injection lasers. *J. Appl. Phys.* , 45:4899–4906, 1974.
- [29] J. N. Walpole, J. P. Donnelly, P. J. Taylor, L. J. Missaggia, C. T. Harris, R. J. Bailey, A. Napoleone, S. H. Groves, S. R. Chinn, R. Huang, and J. Plant. Slab-coupled 1.3- μ m semiconductor laser with single-spatial large-diameter mode. *IEEE Photon. Technol. Lett.* , 14:756–758, 2002.
- [30] R. C. Weast, editor. *CRC Handbook of Chemistry and Physics*. CRC Press, 54th edition, 1973.
- [31] J. N. Winn, R. D. Meade, and J. D. Joannopoulos. Two-dimensional photonic band-gap materials. *J. Mod. Opt.* , 41:257–273, 1994.
- [32] A. Yariv. *Optical Electronics in Modern Communications*. Oxford University Press, Inc., 5th edition, 1997.
- [33] A. Yariv. Coupled-wave formalism for optical waveguiding by transverse bragg reflection. *Opt. Lett.* , 27:936–938, 2002.
- [34] A. Yariv, Y. Xu, and S. Mookherjea. Transverse bragg resonance (tbr) laser amplifier. *Opt. Lett.* , 28:176–178, 2003.

- [35] K. S. Yee. Numerical solution of initial boundary value problems involving maxwell's equations in isotropic media. *IEEE Trans. Antennas Propag.* , AP-14:302–307, 1966.
- [36] P. Yeh. *Optical Waves in Layered Media*. John Wiley & Sons, Inc., 2nd edition, 2005.
- [37] P. Yeh and A. Yariv. Bragg reflection waveguides. *Opt. Commun.* , 19:427–430, 1976.
- [38] P. Yeh, A. Yariv, and E. Marom. Theory of bragg fiber. *J. Opt. Soc. Am.* , 68:1196–1201, 1978.